MISSIONE 4
ISTRUZIONE
RICERCA

SCUOLA DI DOTTORATO
UNIVERSITÀ DEGLI STUDI DI MILANO-BICOCCA

UNIVERSITÀ DEGLI STUDI DI MILANO BICOCCA

Department of Earth and Environmental Sciences (DISAT)
PhD program Chemical, Geological and Environmental Sciences Cycle XXXVIII
Curriculum in Environmental Sciences

Urban Soils as Multifunctional Systems: Carbon Persistence, Vegetation Interactions, and Contaminant Dynamics

Surname: Abu El Khair
Name: Davide
Registration number: 708750

Tutor: Prof.ssa Sandra Citterio
Supervisor: Dott.ssa Chiara Ferré
Coordinator: Prof. Giovanni Malusà

ACADEMIC YEAR 2024/2025

Finanziato dall'Unione europea NextGenerationEU
Ministero dell'Università e della Ricerca
Italiadomani PIANO NAZIONALE DI RIPRESA E RESILIENZA
UNIVERSITÀ DEGLI STUDI DI MILANO BICOCCA

Abstract

Urban and peri-urban soils are increasingly recognized as key components of urban ecosystems, providing essential ecosystem services while simultaneously hosting legacies of anthropogenic disturbance and contamination. Shaped by complex interactions among land-use change, vegetation management, atmospheric deposition, and soil heterogeneity, these soils function as dynamic and stratified systems in which carbon persistence, biological activity, and contaminant behaviour are tightly interconnected. Understanding these processes requires integrated approaches that explicitly consider soil depth, carbon quality, and spatial variability, particularly to capture how carbon storage, biodiversity support, and contaminant risks co-exist and interact in urban and peri-urban ecosystems.

This PhD thesis, developed within the framework of the *PNRR project Biodiversity Future Center - Spoke 5: Urban Biodiversity*, investigates the functioning of urban and peri-urban soils in the Metropolitan City of Milan, with a particular focus on soil organic carbon (SOC) dynamics, soil-vegetation interactions, pyrogenic carbon (PyC) persistence, and heavy metal mobility. By combining field-based soil sampling, laboratory analyses, and process-oriented approaches, the thesis aims to elucidate how carbon pools of different origin and stability interact with vegetation development and contaminant processes in highly heterogeneous urban environments.

The first part of the thesis examines SOC dynamics and soil-vegetation interactions in urban and peri-urban forests established on former agricultural land. Results show that afforestation leads to rapid changes in SOC stocks, humus forms, and understory functional composition, with pronounced depth-dependent patterns and strong links to soil properties and forest development stage. These findings highlight that SOC accumulation in urban forests is governed by multiple, coexisting stabilization pathways rather than by a single dominant process.

The second part focuses on PyC as a chemically distinct and persistent component of urban soil organic matter. At the city scale, PyC is shown to be a ubiquitous fraction of SOC, exhibiting relatively stable PyC:SOC ratios across soil depths and land-use contexts. PyC distribution reflects long-term atmospheric deposition and stabilization mechanisms rather than short-term ecological dynamics, emphasizing its role as a long-term carbon reservoir in urban soils.

The third part addresses methodological uncertainty in PyC quantification by comparing chemo-thermal oxidation (CTO-360) and chemical oxidation (CO) approaches applied to the same soil samples. Methodological differences are most pronounced in surface soils, where CO captures a broader and less refractory aromatic fraction, while PyC estimates obtained by the two methods progressively converge with depth. This depth-dependent convergence indicates the dominance of highly condensed and persistent PyC forms in subsoil horizons and underscores the importance of method-aware interpretation of PyC data.

The final part extends carbon-focused insights to the assessment of heavy metal mobility in unsaturated urban soils. Through laboratory experiments and stochastic modelling, the study demonstrates that contaminant transport is strongly influenced by soil heterogeneity, hydraulic properties, and parameter uncertainty. The

results further show that non-pyrogenic organic carbon represents the primary reactive pool controlling metal retention, while PyC plays a limited direct role in metal binding.

Overall, this thesis demonstrates that urban soils function as stratified, multifunctional systems in which carbon quality, soil depth, and heterogeneity govern both ecosystem services and environmental risks. By integrating pedological, biogeochemical, ecological, and process-based perspectives, the work provides a comprehensive framework for understanding urban soil functioning and supports the development of soil-aware strategies for sustainable management of urban and peri-urban landscapes.

Table of contents

General Introduction

Urbanization represents one of the most pervasive drivers of environmental change, profoundly reshaping soil properties, ecosystem processes, and biogeochemical cycles. In urban and peri-urban landscapes, soils are subjected to overlapping and often interacting pressures, including land-use change, atmospheric deposition, soil sealing, organic amendments, vegetation management, and long-term disturbance. As a result, urban soils exhibit high spatial heterogeneity, reflecting the overlap of multiple anthropogenic and natural drivers. At the same time, similarly to natural soils, they perform a wide range of functions, acting as substrates for vegetation development, reservoirs of legacy contaminants, regulators of water and solute fluxes, and key components of urban green infrastructures.

Within this complex context, urban and peri-urban soils play a dual and sometimes contrasting role. On the one hand, they provide essential ecosystem services, including carbon sequestration, nutrient cycling, water regulation, and support for biodiversity. On the other hand, they often retain the imprint of past and present anthropogenic activities, hosting potentially toxic elements, combustion-derived particles, and other pollutants whose long-term behaviour may pose risks to environmental and human health. Understanding how these functions and risks co-exist and interact requires an integrated, process-based perspective on soil functioning.

Soil organic matter represents a central interface linking physical, chemical, and biological processes in urban soils. Changes in vegetation cover and land use, such as the conversion of agricultural land into urban and peri-urban forests, can strongly influence soil organic carbon (SOC) stocks, vertical distribution, and stabilization mechanisms. However, SOC in urban environments derives from multiple sources, including both biogenic inputs associated with vegetation development and anthropogenic inputs linked to combustion processes and atmospheric deposition. Consequently, total SOC alone may not fully capture the quality, persistence, and functional role of carbon stored in urban soils.

Among the different components of soil organic matter, pyrogenic carbon (PyC) occupies a distinctive position. Formed during incomplete combustion of biomass and fossil fuels, PyC constitutes a chemically heterogeneous but often highly persistent fraction of soil carbon. Urban ecosystems are particularly prone to PyC accumulation due to continuous emissions from traffic, domestic heating, and industrial activities. Once incorporated into soils, PyC can persist for decades to centuries, contributing to long-term carbon storage while potentially interacting with mineral phases and co-occurring contaminants. Yet, PyC remains challenging to quantify, and its environmental significance depends strongly on the analytical approach adopted and on soil depth.

In parallel, urban soils function as active media for the transport and retention of contaminants. In the unsaturated (vadose) zone, water flow, sorption processes, and soil structure jointly control the mobility of trace metals toward groundwater. These processes are strongly influenced by soil heterogeneity and by the same properties that regulate soil carbon dynamics, including texture, organic matter content, and depth-dependent structure. Parameter uncertainty and spatial variability therefore play a critical role in determining contaminant behaviour in urban soils, with important implications for environmental risk assessment.

Despite increasing scientific attention to urban soils, many studies still address soil carbon dynamics, vegetation development, and contaminant behaviour in isolation. Fewer investigations explicitly explore their interconnections across soil depth, land-use history, and spatial scales. This fragmentation limits our ability to interpret urban soil functioning as an integrated system and to design effective soil-based management and mitigation strategies.

From a policy and management perspective, urban soils are increasingly recognized as key components of nature-based solutions, supporting urban afforestation, biodiversity enhancement, and climate mitigation strategies. At the same time, they represent potential sources and pathways of contaminant exposure, requiring careful risk assessment and management. In this context, soil organic matter and pyrogenic carbon play a dual role: they contribute to long-term carbon storage and ecosystem functioning, while also influencing the retention and mobility of contaminants. Integrating carbon dynamics with contaminant processes is therefore essential to fully understand the multifunctionality of urban soils, as contaminant behaviour is intrinsically linked to the same soil properties that regulate carbon persistence and ecosystem functioning, including organic matter composition, soil structure, and depth-dependent heterogeneity.

Objectives and structure of the thesis

The overarching aim of this PhD thesis, developed within the framework of the *PNRR project Biodiversity Future Center - Spoke 5: Urban Biodiversity*, is to investigate urban and peri-urban soils as complex and stratified environmental systems, focusing on the interplay between soil organic carbon dynamics, vegetation development, pyrogenic carbon persistence, and contaminant behaviour. The research is grounded in the soils of the Metropolitan City of Milan, which provide a representative and heterogeneous laboratory for studying urban soil processes under varying land-use histories and degrees of anthropogenic influence.

To achieve this aim, the thesis integrates field-based observations, laboratory analyses, and process-oriented approaches across multiple soil depths and environmental contexts. Rather than treating soils as homogeneous units, particular emphasis is placed on vertical differentiation, carbon quality, and soil heterogeneity as key drivers of ecosystem functioning and contaminant dynamics.

The thesis is structured into four thematic chapters, each addressing a complementary aspect of urban soil functioning.

Chapter 1 examines soil-vegetation interactions and SOC dynamics in urban and peri-urban forests established on former agricultural land. By combining pedological analyses with vegetation functional traits and humus form characterization, this chapter explores how soil properties and vegetation co-evolve following afforestation, and how SOC accumulation varies with soil depth and forest development stage.

Chapter 2 focuses on PyC at the city scale. Through the analysis of PyC distribution across a wide range of urban and peri-urban green areas, this chapter investigates depth patterns, relationships with SOC fractions, and the role of land-use history in shaping PyC persistence within urban soils.

Chapter 3 addresses methodological uncertainty in PyC quantification by comparing chemo-thermal oxidation (CTO-360) and chemical oxidation (CO) approaches applied to soil samples taken from a peri-urban park

inside the Metropolitan City of Milan. This chapter highlights depth-dependent differences and convergence between methods, clarifying how analytical choices influence the interpretation of PyC stocks and stabilization pathways.

Chapter 4 shifts the focus toward contaminant behaviour in unsaturated urban soils. Presented in the form of a published article, this chapter combines laboratory experiments and stochastic modelling to assess the mobility of heavy metals under unsaturated flow conditions, emphasizing the role of soil heterogeneity and parameter uncertainty in contaminant transport toward groundwater.

Together, these chapters provide an integrated framework for understanding urban soils as multifunctional systems in which carbon persistence, vegetation dynamics, and contaminant processes are tightly interconnected. By bridging pedology, biogeochemistry, ecology, and process-based analysis, this thesis contributes to advancing urban soil science and to informing sustainable management of urban and peri-urban landscapes.

Chapter 1.

Soil-vegetation interactions and SOC dynamics in urban and peri-urban forests established on former agricultural land

This chapter investigates how soil properties and understory vegetation co-evolve in urban and peri-urban forests established on former agricultural land. By combining pedological analyses, humus form classification, and plant functional traits, it examines the processes underlying soil organic carbon accumulation and ecosystem development. Particular attention is given to depth-dependent patterns and to the role of pedolandscape context in shaping soil-vegetation interactions across a wide forest age gradient.

1. Introduction

Urban and peri-urban soils play a critical role in sustaining ecosystem functions in densely populated areas, yet their pedogenic trajectories following afforestation remain poorly understood. These soils are characterized by pronounced heterogeneity due to long-term human disturbance, but provide essential services including carbon sequestration, biodiversity support, and water regulation (Morel *et al.*, 2015; Canedoli *et al.*, 2020). Urban forests can store substantial amounts of soil organic carbon (SOC), making them important contributors to climate change mitigation (Pouyat *et al.*, 2006; Churkina *et al.*, 2010).

Peri-urban forests established on former croplands represent key opportunities for restoring ecological processes and enhancing ecosystem services (Salbitano *et al.*, 2016). However, SOC accumulation following afforestation depends on multiple interacting factors, including stand age, vegetation composition, climate, and pre-afforestation soil cultivation and management (Laganière *et al.*, 2010; Mayer *et al.*, 2020). Intensive agricultural practices prior to afforestation tend to reduce SOC stocks and alters nutrient cycling, with legacy effects that may persist for decades (Don *et al.*, 2011). Understanding how urban reforestation can mitigate the long-term effects of past agricultural land use on soils remains a critical research priority (Cambou *et al.*, 2018; Resemini *et al.* 2025).

Plant functional traits and Grime's CSR strategy provide a robust framework for interpreting plant responses to environmental disturbance and stress, finally categorizing species based on their adaptation (in terms of trait characteristics) in competitor (C), stress-tolerator (S) and ruderals (R) (Grime, 1977; Pierce *et al.*, 2017). Mainly, traits associated with the "leaf economics spectrum", such as specific leaf area (SLA) and leaf dry matter content (LDMC), capture trade-offs between resource acquisition (e.g. nutrients, light, etc.) and conservation (Wright *et al.*, 2004; Reich, 2014). Because plant functional traits reflect species' strategies for resource acquisition and conservation, they are strongly influenced by soil properties that control nutrient availability, organic matter dynamics, and rooting conditions, with soil acting as a key environmental filter. Although most studies focus on surface soil properties (0-10 cm), recent evidence suggests that soil-vegetation interactions may extend to deeper horizons, particularly in systems undergoing pedogenic reorganization (Vasenev *et al.*, 2014; Schittko *et al.*, 2020).

While most soil-vegetation studies rely on routine chemical analyses, humus form classification provides an integrative, field-assessable descriptor of organic matter dynamics (Ponge, 2003; Zanella *et al.*, 2011). Humus forms, defined by organic horizon morphology, capture differences in decomposition pathways, nutrient cycling, and soil biota interactions (Jabiol *et al.*, 2013). The European classification distinguishes three main types: Mull, Moder, and Mor, which reflect increasing organic matter accumulation and decreasing biological activity (Zanella *et al.*, 2011).

In natural forests, humus forms are closely linked to soil fertility, pH, and nutrient availability, and are associated with predictable shifts in understory vegetation composition (Wardle *et al.*, 2004; Berg & McClaugherty, 2014). Mull systems typically support fast-growing, competitive species, whereas Mor systems favor stress-tolerant species adapted to oligotrophic conditions. Despite their ecological relevance, humus

forms remain underexplored in urban and peri-urban forests, where soil legacy effects and management practices may alter pedogenic trajectories (Cambou *et al.*, 2018).

Understanding soil-vegetation relationships in urban reforestation remains limited: humus form development, its links to understory vegetation, and the influence of spatial autocorrelation are still poorly studied.

To address these gaps, we investigated soil and understory vegetation relationships across 44 urban and peri-urban forest sites in the metropolitan area of Milan (Italy), spanning a temporal gradient. Specifically, we aimed to: (i) quantify SOC responses to urban forest establishment by comparing forested soils with agricultural reference soils and assessing SOC accumulation with forest age; (ii) test mechanistic pathways linking humus forms to understory vegetation, distinguishing direct effects from those mediated by soil chemistry; (iii) analyze trait-environment relationships shaping herbaceous community composition; and (iv) evaluate the influence of soil depth on trait-environment associations to inform efficient sampling strategies in urban forest research.

2. Materials and Methods

2.1 Study Forest Areas

The Metropolitan City of Milan (northern Italy) is located in the Po Valley alluvial plain (~100 m a.s.l.) and is characterized by a continental climate and high population density. Land use includes a mosaic of built-up areas, agricultural land, and remnant or planted woodlands.

We selected 44 georeferenced forest sites (Table 2.1), all established on former agricultural land and spanning a wide gradient of stand age (10 to >150 years), tree cover (10-90%), and soil conditions. Sites were categorized as: 28 forested peri-urban parks (PPf), 3 spontaneous urban forests (SUF), and 13 mature woodlands (W).

Forest age (mean ± SD: 52 ± 45 years), was determined from historical aerial photographs, municipal planting records, and dendrochronological information where available. Several mature woodlands were already recorded as forest in historical cadastral maps from the 18^{th}-19^{th} centuries, confirming long-term forest continuity.

Table 2.1. Characteristics of the 44 sampled sites.

Plot ID	site	Latitude	Longitude	Altitude (m)	green area	age	type of environment	Pedolandscape Unit (PU)
BB - Bosco della Besozza	BB-01	45.4694	9.3195	111	PPf	20	semi-open mixed broadleaf forest	PU 2
	BB-02	45.4712	9.3208	111			semi-open mixed broadleaf forest	
BC - Bosco di Cusago	BC-01	45.4501	9.006	126	W	89	closed mixed broadleaf natural forest	PU 3
	BC-02	45.4479	9.0069	126			closed mixed broadleaf natural forest	
	BC-04	45.4497	9.0088	126			semi-open mixed broadleaf natural forest	
BF - Bosco del Fontanone	BF-01	45.5339	9.3173	136	PPf	55	open mixed broadleaf natural forest (*Robinia pseudoacacia* dominance)	PU 1
	BF-03	45.5328	9.3197	135		50	open mixed broadleaf forest	
	BF-04	45.5337	9.3191	135		35	linear broadleaf forest	
BM - Bosco di Montorfano	BM-01	45.3661	9.3259	86	PPf	18	linear broadleaf forest	PU 6
	BM-03	45.3638	9.329	86		28	closed mixed broadleaf forest	
	BM-04	45.3637	9.3288	86		27	closed mixed broadleaf forest	
	BM-05	45.3633	9.3279	86		27	closed mixed broadleaf forest	
BR - Bosco di Riazzolo	BR-01	45.4397	8.9555	128	W	71	closed mixed broadleaf natural forest	PU 3
	BR-02	45.4391	8.9587	127		150	closed mixed broadleaf natural forest	
	BR-03	45.4387	8.9573	127		150	closed mixed broadleaf natural forest	
	BR-04	45.4391	8.9609	127		71	semi-open mixed broadleaf natural forest	
	BR-05	45.4407	8.9631	127		150	linear broadleaf forest	
	BR-06	45.4406	8.9620	127		150	semi-closed mixed broadleaf natural forest	
CA - Bosco del Carengione	CA-01	45.4459	9.3081	104	PPf	18	semi-open mixed broadleaf forest	PU 2
CH - Bosco della Chiesa	CH-01	45.4446	8.9536	129	W	150	semi-closed mixed broadleaf forest	PU 3
	CH-02	45.4462	8.9532	129			semi-closed mixed broadleaf forest	
CT- Boscoincittà	CT-04	45.4857	9.0941	131	PPf	51	semi-closed mixed broadleaf forest	PU 3

Table 2.1. (continue).

Plot ID	site	Latitude	Longitude	Altitude (m)	green area	age	type of environment	Pedolandscape Unit
LG - La Goccia	LG-01	45.5042	9.1493	134	SUF	31	linear broadleaf forest	PU 3
	LG-02	45.5079	9.1523	135		37	semi-open mixed broadleaf natural forest (*Robinia pseudoacacia* dominance)	
	LG-04	45.5093	9.1517	135		21	open mixed broadleaf natural forest (*Robinia pseudoacacia* dominance)	
MS - Oasi del Municipio SGM	MS-04	45.4020	9.2836	95	PPf	22	closed mixed broadleaf forest	PU 5
	MS-06	45.4011	9.2857	95		10	linear broadleaf forest	
NA - Parco Natura	NA-02	45.4459	9.0832	121	PPf	17	linear broadleaf forest	PU 3
PC - Parco delle Cave	PC-01	45.4691	9.1041	126	PPf	15	linear broadleaf forest	PU 3
	PC-02	45.4660	9.1066	124		28	open mixed broadleaf forest (*Robinia pseudoacacia* dominance)	
	PC-03	45.4736	9.1016	127		27	linear broadleaf forest	
PNM - Parco Nord Milano	PN-01	45.5271	9.1996	139	PPf	25	closed mixed broadleaf forest	PU 1
	PN-02	45.5290	9.2060	139		33	closed mixed broadleaf forest	
	PN-03	45.5296	9.2117	139		38	open mixed broadleaf forest	
	PN-04	45.5294	9.1988	140		27	open mixed broadleaf forest	
	PN-05	45.5405	9.2098	140		34	semi-open mixed broadleaf forest	
	PN-06	45.5417	9.2122	140		41	semi-open mixed broadleaf forest	
	PN-10	45.5273	9.1987	139		18	semi-open mixed broadleaf forest	
	PN-11	45.5260	9.2013	137		18	semi-open mixed broadleaf forest	
	PN-12	45.5244	9.1998	137		18	linear broadleaf forest	
TF - Testa del Fontanile	TF-02	45.4056	9.2811	95	PPf	35	open mixed broadleaf natural forest (*Robinia pseudoacacia* dominance)	PU 5
VA - Oasi di Vanzago	VA-01	45.5225	8.9772	160	W	89	semi-open mixed broadleaf forest	PU 4
	VA-02	45.5255	8.9765	160		18	open mixed broadleaf forest (*Robinia pseudoacacia* dominance)	
VB - Viale Berbera	VB-01	45.5212	9.2047	136	PPf	16	linear broadleaf forest	PU 1

2.2 Forest Soil Sampling, Humus Forms and Laboratory Analyses

Soil sampling was conducted in 2024-2025 at the 44 georeferenced sites using a composite sampling design. In each 10×10 m plot, three subsamples were collected in a triangular layout at three depths (0-10, 10-20, and 20-40 cm) and composited by depth.

Organic horizons (OL, OF, OH) were sampled where present following Zanella et al. (2011), using a defined area (18 cm quadrat) and composited per horizon. Mineral soil samples were air-dried, sieved at 2 mm, and analyzed for pH (1:2.5 soil:water ratio, potentiometric), total carbonates (Dietrich-Frühling calcimeter), SOC and total nitrogen (TN) (dry combustion, Flash EA 1112 elemental analyzer), available P (avP, Olsen & Dean, 1965), and three-fractions soil texture (pipette method, after sodium hexametaphosphate dispersion).

Organic samples were oven-dried, homogenized, and analyzed for OC, TN (dry combustion), and OM (loss on ignition at 550 °C).

Forest humus forms were classified following the European system (Zanella *et al.*, 2011, 2018) based on the morphology and thickness of organic horizons and A-horizon structure (zoogenic: biomacrostructured, biomesostructured, biomicrostructured; and non-zoogenic: single grain or massive). Three humus types were identified: Mull (rapid decomposition, thin/absent OL, high earthworm activity), Moder (intermediate decomposition rates, arthropod-dominated, with distinct OF horizon), and Mor (slow decomposition, fungal-dominated, characterized by thick OF and OH layers). Classification was performed in all plots with complete organic profiles and vegetation data.

2.3 Soil Organic Carbon Responses to Urban Forest Establishment

To assess the effect of urban forest establishment on soil organic carbon accumulation, we employed a paired comparison design contrasting forested plots with agricultural reference soils from the same pedolandscape context.

Urban forests in the Milan metropolitan area were established on former agricultural land, primarily cultivated as annual cropland over recent decades to centuries. These agricultural soils serve as the most appropriate baseline for quantifying SOC changes following afforestation, as they represent the typical pre-conversion condition rather than a degraded state (Guo & Gifford, 2002). The cropland management regime (plow tillage, annual crops, moderate fertilization) maintains SOC at a relatively stable equilibrium characteristic of intensive agriculture in the Po Plain.

Both forest and agricultural sites were classified into six Pedolandscape Units (PU 1-6) based on parent material, geomorphology, and pedogenic history, following regional soil survey frameworks for the Lombardy Plain. PUs represent distinct soil-landscape contexts with characteristic baseline SOC levels, texture, and drainage. By pairing forest and agricultural samples within PU, we controlled for this fundamental source of SOC variation, isolating the land-use effect (forest vs cropland) and age-related accumulation (within forests). PU distribution was unbalanced by necessity: PU 3 contained 19 forest plots (43% of dataset) spanning the widest age range, while PU 2, 4, 5, 6 contained 2-4 plots each. All PUs had equal agricultural replication (n = 6 profiles each).

Forest age distribution varied among the considered PU with PU 3 containing the widest age range (15-150 years). Other PU contained primarily young forests (<35 years; PU 2, 5, 6; n = 3-4 each) or intermediate ages (PU 1: 16-55 years, n = 13; PU 4: 18-89 years, n = 2).

Agricultural reference soils were sampled from 36 locations external to the Milan urban forests but within the same six PU, ensuring pedolandscape comparability (6 profiles per PU, systematically distributed). All agricultural sites were under active annual cropland management at the time of sampling, predominantly maize-wheat rotations typical of the Po Plain. Sites were selected to avoid recent (<5 years) land-use changes, irrigation infrastructure, or obvious soil disturbances beyond routine agricultural management.

Agricultural soils were treated as the reference condition representing pre-afforestation SOC levels, operationally coded as 'Age = 0' in statistical models. This assumes agricultural SOC has reached a quasi-equilibrium state, a reasonable assumption given long-term (>50 years) cultivation history throughout the study region.

Geographic coordinates for agricultural sites (Monte Mario / Italy zone 1, EPSG:3003) were transformed to match the forest coordinate system (EPSG:32632) using *pyproj* library for spatial proximity analysis.

2.4 Understory-Vegetation Survey

In the 44 plots with herbaceous cover >1%, we conducted 10×10 m surveys following Cornelissen et al. (2003). Species' cover (%) was visually estimated and recorded using a phytosociological approach (expert-based, ideally subdividing the whole plot into sub-plots of 2.5 × 2.5 to reduce the error; Gentili *et al.*, 2019); stand age was retrieved by forest owners (or managers) or assessing the series of historical aerial photos.

Functional traits and CSR strategies of recorded species were derived using *StrateFy tool* (Pierce *et al.*, 2017) from three leaf traits: Leaf Area (LA, mm^2), Leaf Fresh Weight (LFW, mg), and Leaf Dry Weight (LDW, mg). The tool computes derived traits - Succulence Index (SI), Leaf Water Content (LWC, %), Leaf Mass per Area (LMA, mg mm^{-2}), Leaf Dry Matter Content (LDMC, %), Specific Leaf Area (SLA, mm^2 mg^{-1}), Leaf Nitrogen Content (LNC, %), Leaf Carbon Content (LCC, %) - and assigns tertiary CSR classification (C%, S%, R%). Community-weighted means (CWMs) were calculated using species relative cover as weighting.

2.5 Statistical Analyses

All statistical analyses were performed in R version 4.4.3 (R Core Team, 2025) and structured in two main steps. First, an exploratory correlation analysis was conducted to identify bivariate relationships among soil properties, forest age, and herbaceous vegetation functional traits across soil depths. Spearman correlation matrix was calculated to assess depth-dependent soil-vegetation relationships.

Although forest age effects on soil properties were observed across all depths, subsequent multivariate analyses focused primarily on surface soil properties (0-10 cm), which showed the strongest associations with herbaceous vegetation traits and biomass. This approach reflects both ecological reasons (shallow herbaceous rooting and litter-soil interactions) and statistical coupling at 0-10 cm, allowing the results to be interpreted as representative of rhizosphere processes in shallow-rooted herbaceous communities.

Statistical methods are described below according to the specific objectives of the study: (i) SOC responses to urban forest establishment and forest age (Section 2.5.1), (ii) humus form effects on soil and vegetation properties (Section 2.5.2), and (iii) trait-environment relationships (Section 2.5.3).

Mixed-effects models were used to account for the unbalanced distribution of forest plots among PUs, with PU included as a random effect (Borcard *et al.*, 2011).

2.5.1 Soil Organic Carbon Responses to Urban Forest Establishment

Statistical analyses were designed to quantify the effects of urban forest establishment on SOC relative to agricultural land use and to characterize SOC accumulation with forest age. A hierarchical modeling framework was applied to disentangle land-use effects, forest age, pedolandscape context, and spatial structure with analyses conducted at the plot level and accounted for grouping within PUs and spatial dependence among observations. Analyses were conducted at the plot level, accounting for grouping within PUs and spatial dependence among observations.

Spatial autocorrelation in SOC and key predictors was evaluated prior to modeling revealing strong clustering in forest plots (Moran's $I > 0.85$, $p < 0.001$).

Residual spatial dependence not explained by pedolandscape structure was controlled using Moran's Eigenvector Maps (MEMs; Dray *et al.*, 2006), selected via forward selection ($\alpha = 0.05$).

Forested and agricultural soils were compared using linear mixed-effects models:

$$SOC \sim Land_{use} + (1 \mid PU)$$

where Land_use (Forest vs Agriculture) represents the fixed effect of afforestation and (1 | PU) accounts for pedolandscape-level variability. Effect sizes were quantified using Cohen's *d*.

SOC dynamics within forests were evaluated by modeling SOC as a function of forest age while controlling PUs and MEMs:

$$SOC_{forest} \sim Age + (1 \mid PU) + MEMs$$

and to account for potential nonlinear accumulation patterns, an alternative model included a quadratic age term:

$$SOC_{forest} \sim Age + Age^2 + (1 \mid PU) + MEMs$$

Fine-scale spatial confounding between forest and agricultural sites was assessed using spatial proximity analysis, correlating forest SOC with SOC in the nearest agricultural reference soil.

All analyses were performed using Python 3.12 (*pandas*, *scipy*, *statsmodels*, *scikit-learn*, *pyproj*) and R version 4.3 (*lme4*, *MuMIn*). Statistical significance was assessed at $\alpha = 0.05$. Effect sizes were interpreted following Cohen (1988), with thresholds of 0.2, 0.5, and 0.8 corresponding to small, medium, and large effects.

2.5.2 Humus Forms

Differences in soil properties and vegetation characteristics among humus forms were assessed using Kruskal-Wallis *H* tests for continuous variables, with Dunn's post hoc tests and Bonferroni correction. Relationships between humus forms (treated as an ordinal variable: Mull = 1, Moder = 2, Mor = 3) and forest age were evaluated using Spearman's rank correlation coefficient (ρ), while associations with green area types were tested using Chi-square tests of independence, with effect size quantified using Cramér's *V*.

Causal pathways linking humus forms, soil chemistry, and herbaceous biomass were analyzed using piecewise structural equation models (pSEMs; Lefcheck, 2016), which estimate path coefficients through linked linear models and allow inclusion of mixed-effects and spatial covariates, and are well suited to moderate sample sizes.Humus forms were represented using dummy variables (Humus_Moder and Humus_Mor), with Mull as the reference category. Two alternative models were tested:

Model 1 (mediation pathway) tested whether humus form effects on herbaceous biomass were fully mediated by soil chemical properties, with pH modeled as a function of humus form, SOC as a function of humus form and tree cover, and herbaceous biomass as a function of soil chemistry, tree cover, and spatial structure:

$$pH \sim Humus\_Moder + Humus\_Mor$$
$$SOC \sim Humus_{Moder} + Humus_{Mor} + Tree_{cover}$$
$$Herbaceous_{biomass} \sim pH + SOC + Tree_{cover} + MEMs$$

Model 2 (direct effects) tested whether humus forms exerted additional direct effects on herbaceous biomass, with humus dummy variables and available phosphorus (avP) added directly to the biomass equation:

$$pH \sim Humus_{Moder} + Humus_{Mor}$$
$$SOC \sim Humus_{Moder} + Humus_{Mor} + Tree_{cover}$$
$$Herbaceous_{biomass} \sim Humus_{Moder} + Humus_{Mor} + pH + SOC + Tree_{cover} + avP + MEMs$$

Tree cover was included as a predictor of SOC based on directed separation tests indicating a missing path in preliminary model evaluation. Selected Moran's Eigenvector Maps (MEMs), identified through forward selection, were included in the biomass equations to control for residual spatial autocorrelation.

Residual spatial autocorrelation was evaluated using Moran's I on model residuals, with non-significant values ($p > 0.05$) indicating adequate control of spatial structure.

Overall model fit was assessed using Fisher's *C* statistic, and competing models were compared using the Akaike Information Criterion (AIC). Standardized path coefficients were used to facilitate comparison of effect sizes among predictors.

Variance partitioning (Peres-Neto *et al.*, 2006) quantified contributions of humus forms, soil chemical variables (pH, SOC, tree cover, avP), and spatial structure (MEMs) to variation in herbaceous biomass, separating pure environmental, pure spatial, and shared components.

2.5.3 Trait-Environment Relationships

Trait-environment relationships were analyzed using RLQ ordination, linking environmental variables (R), species composition (L), and functional traits (Q) as implemented in the *ade4* package (Dray *et al.*, 2014). Humus forms were included as dummy variables (Humus_Moder, Humus_Mor, Mull as reference) alongside continuous soil chemical properties (pH, SOC, TN, avP) and structural variables (tree cover, forest age). Fourth-corner analysis (Legendre *et al.*, 1997) tested the significance of trait-environment associations, with 999 permutations using models 2 and 4 to account for both site and species constraints, and p-values were adjusted for multiple testing using the False Discovery Rate (FDR) method of Benjamini and Hochberg (1995).

3. Results

3.1 Soil Properties, Vegetation Functional Traits, and CSR Strategies

Surface soils showed higher organic matter and nutrient contents declining with depth. Mean SOC decreased from 4.3% (0-10 cm) to 1.4% (20-40 cm), while TN declined from 0.37% to 0.14%. Soil pH remained moderately acidic (5.2-5.3), and avP declined from 24 to 16 mg kg^{-1} with depth. Wide ranges among sites (SOC 1.5-9.2%, pH 3.8-7.3, avP 10-75 mg kg^{-1} in the first layer), together with high coefficients of variation (Table 3.1), reflected strong pedological heterogeneity.

Table 3.1. Descriptive statistics (n = 44) of soil physico-chemical properties measured in forest plots across three soil depth intervals (0-10, 10-20 and 20-40 cm). For each variable, mean, standard deviation (SD), coefficient of variation (CV, %), minimum and maximum values are reported. Variables include soil organic carbon (SOC), total nitrogen (TN), C:N ratio, pH, available phosphorus (avP), and particle-size fractions (sand, silt, and clay).

Variable	Depth	Mean	SD	CV %	Min	Max
SOC (%)	0-10 cm	4.31	2.29	53.1	1.49	9.19
	10-20 cm	2.18	0.68	31.2	0.91	3.57
	20-40 cm	1.43	0.50	35.4	0.32	2.82
TN (%)	0-10 cm	0.37	0.18	48.7	0.15	0.70
	10-20 cm	0.20	0.06	28.3	0.10	0.34
	20-40 cm	0.14	0.05	35.0	0.04	0.28
C:N ratio	0-10 cm	11.46	1.41	12.3	9.7	16.2
	10-20 cm	10.77	1.45	13.4	9.0	16.3
	20-40 cm	10.18	1.13	11.0	8.1	13.4
pH	0-10 cm	5.21	0.82	15.7	3.8	7.3
	10-20 cm	5.17	0.83	16.1	3.8	7.6
	20-40 cm	5.30	0.87	16.3	3.9	7.8
avP (mg kg^{-1})	0-10 cm	23.7	12.5	52.7	10.5	74.6
	10-20 cm	19.6	10.1	51.7	7.1	54.2
	20-40 cm	16.1	10.6	66.1	2.9	55.7
Sand (g kg^{-1})	0-10 cm	542.3	117.4	21.7	381	778
	10-20 cm	547.9	125.1	22.8	374	786
	20-40 cm	561.6	127.0	22.6	371	852
Silt (g kg^{-1})	0-10 cm	371.0	115.9	31.2	171	540
	10-20 cm	359.5	117.3	32.6	157	534
	20-40 cm	345.0	120.9	35.1	109	519
Clay (g kg^{-1})	0-10 cm	86.6	25.3	29.2	38	143
	10-20 cm	92.5	31.0	33.5	28	162
	20-40 cm	93.4	32.0	34.3	16	164

When soil properties were integrated over increasing soil thicknesses (0-10, 0-20, and 0-40 cm), a clear dilution effect was observed, with progressively lower concentrations resulting from the inclusion of deeper, less organic-rich layers (Appendix Figure A1).

Correlation analyses between soil properties and vegetation traits across three depth intervals (0-10, 0-20, 0-40 cm) demonstrated that surface soils exhibited the highest proportion of significant associations with

herbaceous vegetation (Appendix Table A1). Based on this pattern, subsequent analyses focused primarily on surface soil properties, while deeper layers were retained for comparative purposes.

Leaf functional traits exhibited wide interspecific variability across the understory species pool (Table 3.2). LA ranged from approximately 165 to over 40,500 mm^2, while LFW varied between ~24 and 10,500 mg and LDW between ~5 and 3,000 mg. Some derived traits also spanned broad ranges, with SLA varying from ~15 to 70 $m^2\ kg^{-1}$, LNC from ~1.4 to 5.7%, LMA from ~15 to 64 g m^{-2}, LDMC from ~9 to 33%, and SI from 2 to 21.

Table 3.2. Community-Weighted Mean (CWM) Functional Traits. CWM values calculated as abundance-weighted means: CWM = Σ(Cover_i × Trait_i) / Σ(Cover_i), where Cover_i is the percent cover of species i.

Trait	Mean	SD	CV %	Min	Max
CWM_LFW	677,7	1541,3	227,4	24,5	10499,4
CWM_LA	3406,9	5932,2	174,1	165,3	40522,5
CWM_LDW	164,2	441,0	268,5	4,7	2986,8
CWM_LDMC	21,2	5,5	26,1	9,5	32,9
CWM_SLA	34,8	13,0	37,4	15,7	68,1
CWM_LMA	35,1	10,9	31,1	15,3	63,9
CWM_SI	1,4	0,3	20,7	0,8	2,0
CWM_LWC	78,9	5,4	6,8	67,7	90,5
CWM_LNC	2,8	0,9	32,1	1,4	5,7
CWM_LCC	45,6	3,3	7,2	41,4	52,2

Notes: trait abbreviations. LFW = Leaf Fresh Weight (mg), LA = Leaf Area (mm^2), LDW = Leaf Dry Weight (mg), LDMC = Leaf Dry Matter Content (%), SLA = Specific Leaf Area ($mm^2\ mg^{-1}$), LMA = Leaf Mass per Area (mg mm^{-2}), SI = Succulence Index, LWC = Leaf Water Content (%), LNC = Leaf Nitrogen Content (%), LCC = Leaf Carbon Content (%). All traits based on standardized measurements of 40 herbaceous species.

CSR strategies were unevenly distributed across the 40 understory species. Competitive and competitive-ruderal (C and CR) strategies accounted for 45% of the species pool, followed by CSR strategies (22.5%). Stress-related strategies (CS and SR) represented 12.5% of species, while pure ruderal strategies accounted for 20%. No species were classified as pure stress-tolerators (S). The overall distribution of understory species within the CSR functional space is shown in Figure 3.1.

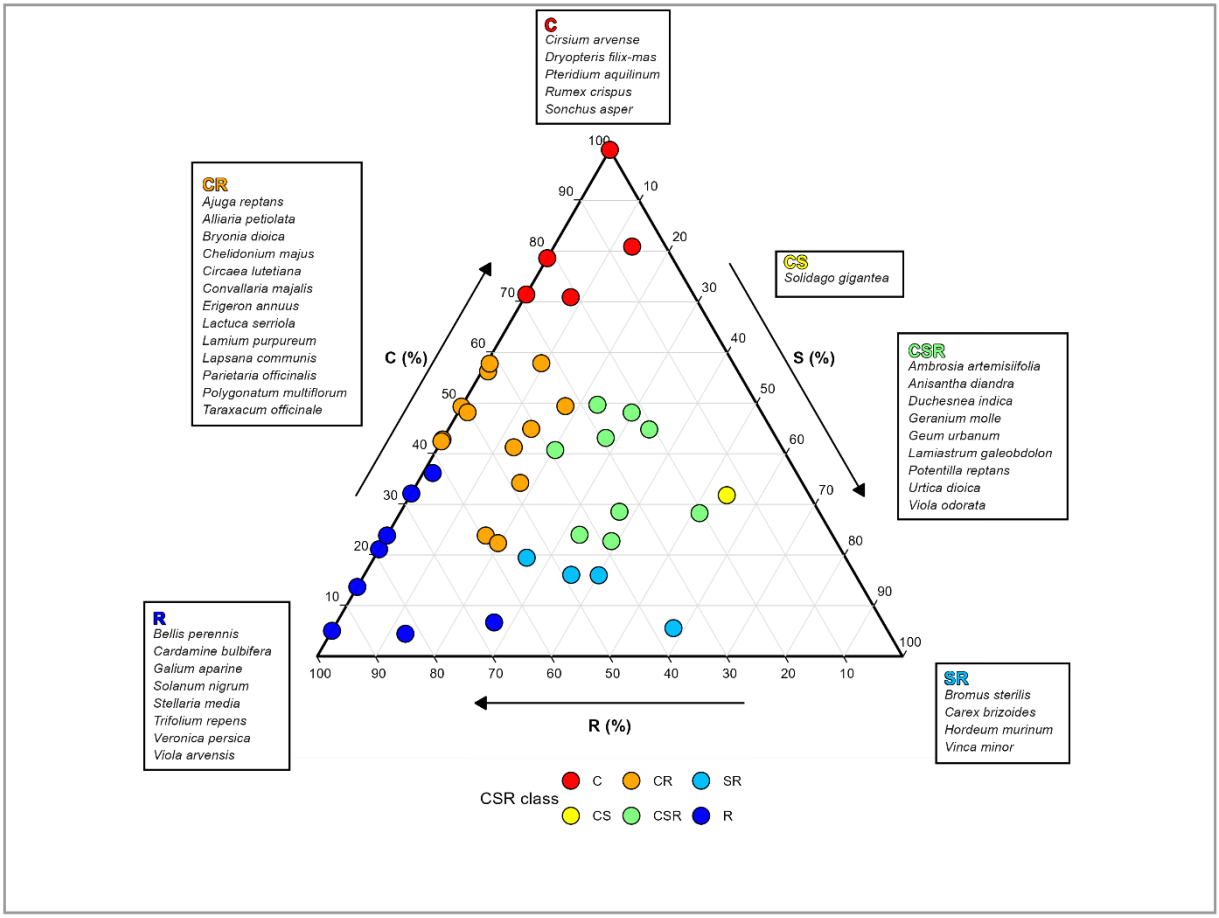

Figure 3.1. CSR functional strategy classification of 40 herbaceous species from Milan urban/peri-urban forests. Species positions are based on Competitor (C), Stress-tolerator (S), and Ruderal (R) scores derived from leaf functional traits using *StrateFy* (Pierce *et al.*, 2017).

Forest age showed strong associations with soil properties across depths, particularly with SOC and total nitrogen, with the strongest relationships observed in surface soils. Because forest age is treated explicitly as a driver of soil organic carbon accumulation, its effects are examined in detail in a dedicated section (see Section 3.2).

3.2 Forest Soil Organic Carbon

Urban forests exhibited substantially higher SOC than agricultural reference soils across all depths (Figure 3.2). At the surface horizon (0-10 cm), forest SOC (4.31 ± 2.29%, mean ± SD, n = 44) was 2.98% higher than agriculture (1.32 ± 0.41%, n = 36), representing a 225% increase ($t = 7.71$, df = 78, $p < 0.001$). Effect size was very large (Cohen's $d = 1.73$), indicating minimal overlap in SOC distributions between land uses (Figure 3.2 C).

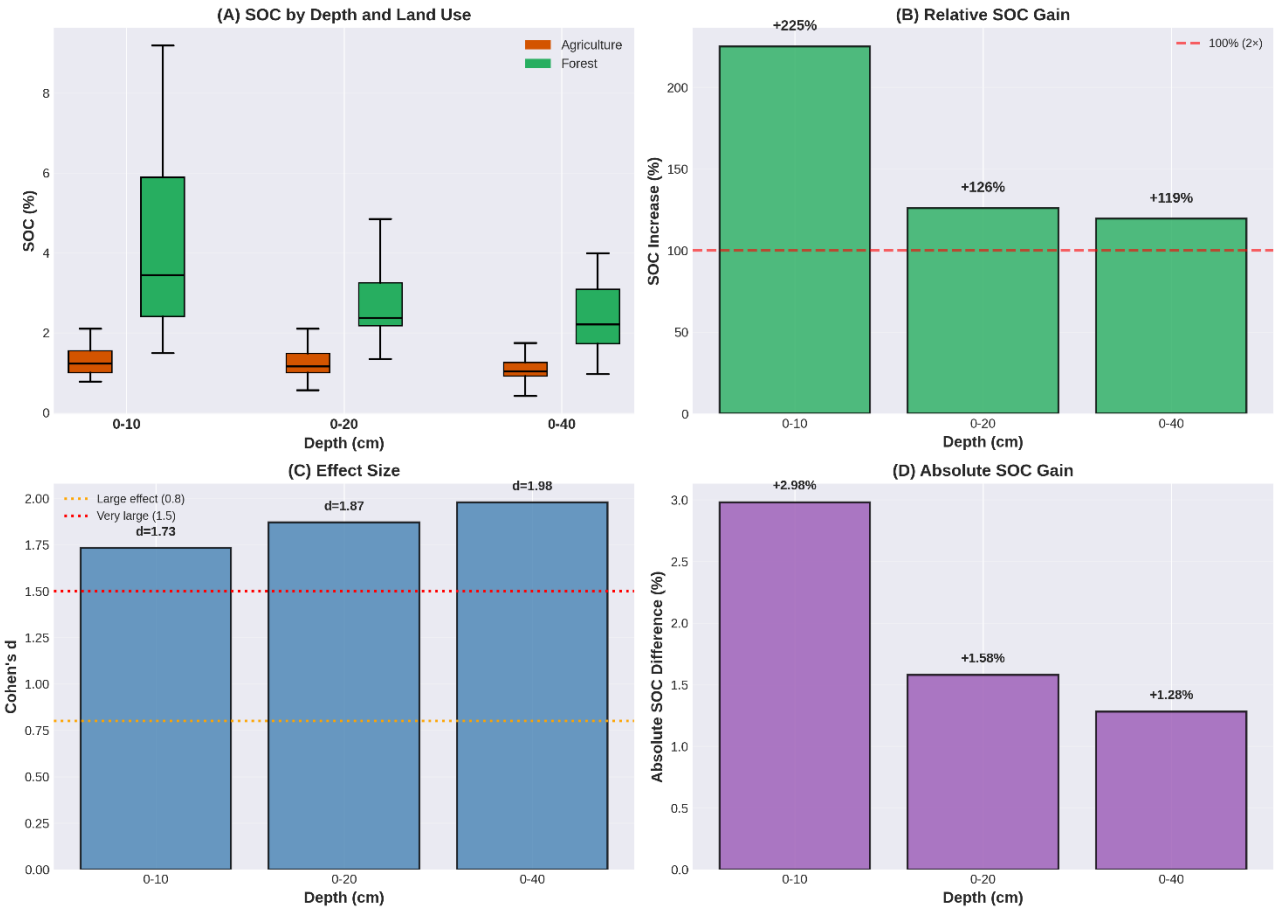

Figure 3.2. Overall forest vs agriculture comparison. (A) Soil organic carbon (SOC) distribution by depth and land use; boxplots show median, quartiles, and range. (B) Relative SOC increase in forests compared to agriculture. (C) Effect sizes (Cohen's *d*) showing very large effects ($d > 1.5$) at all depths. (D) Absolute SOC gain (forest minus agriculture). Error bars = ±SD. *** $p < 0.001$.

The forest advantage persisted at deeper horizons but attenuated with depth (Figure 3.3 A,B): 0-20 cm (+126%, Cohen's $d = 1.87$, $p < 0.001$) and 0-40 cm (+119%, Cohen's $d = 1.98$, $p < 0.001$). Notably, effect sizes increased with depth despite smaller absolute differences, reflecting reduced variance at deeper horizons.

Forest-agriculture SOC differences varied substantially among Pedolandscape Units, ranging from negligible to five-fold increases (Figure 3.3, Appendix Table A2). In the first layer, PU 3 (n=19 forest) exhibited the largest response (+4.98%, +486%, $t = 4.83$, $p < 0.001$), while PU 2 showed no significant forest effect (+0.09%, +5%, $t = 0.43$, $p = 0.683$), attributable to very young forest age (18-20 years) and a relatively high agricultural baseline (1.79%).

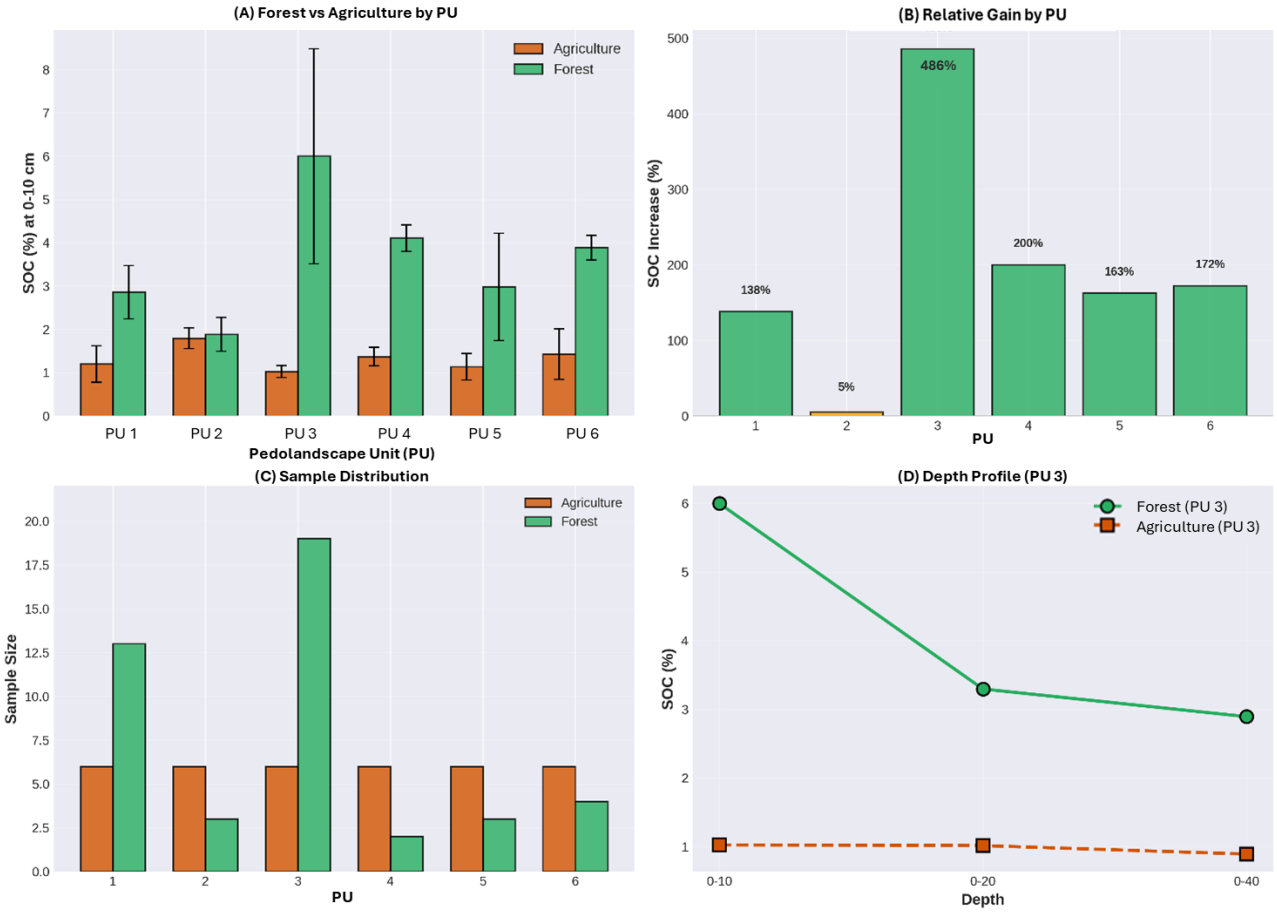

Figure 3.3. Pedolandscape-specific comparisons. (A) Mean SOC (±SD) at 0-10 cm for forest (green) and agriculture (orange) across six Pedolandscape Units (PUs). (B) Relative SOC gain by PU, ranging from 5% (PU 2, young forests) to 486% (PU 3, old forests). (C) Sample size distribution. (D) Depth profile for PU 3 (n=19 forest, 6 agriculture). *** $p < 0.001$, ** $p < 0.01$, * $p < 0.05$, ns = not significant.

Mixed effects model confirmed significant land-use and PU effects (0-10 cm): Land use $\beta = +2.89\%$, SE = 0.38, $t = 7.61$, $p < 0.001$; PU random effect variance $\sigma^2 = 1.12$ (ICC = 0.47). Nearly half of SOC variance (47%) was attributable to pedolandscape context, underscoring the importance of controlling for soil-landscape setting in land-use comparisons.

Within the forest subset, SOC at 0-10 cm increased significantly with stand age (Figure 3.4 A,B). A simple linear regression indicated an apparent accumulation rate of +0.43% SOC per decade ($R^2 = 0.701$, $p < 0.001$). However, both SOC and forest age exhibited strong spatial clustering (Moran's $I = 0.901$ and 0.868, respectively; $p < 0.001$), indicating substantial spatial confounding and inflation of the unadjusted age effect (Dormann *et al.*, 2007).

After controlling spatial structure using Moran's Eigenvector Maps (6 MEMs), the age effect reduced substantially but remained significant: $\beta = 0.0146 \pm 0.0035$ (SE), $t = 4.17$, $p < 0.001$ (Figure 3.4 B, Appendix Table A3). This represents a ~74% reduction relative to the uncorrected estimate, demonstrating that much of the apparent age-SOC relationship was driven by geographic clustering rather than local pedogenic processes. Nonetheless, the persistence of a significant age effect confirms progressive SOC accumulation with forest

maturation, consistent with temperate afforestation chronosequences (Poeplau *et al.*, 2011; Laganière *et al.*, 2010).

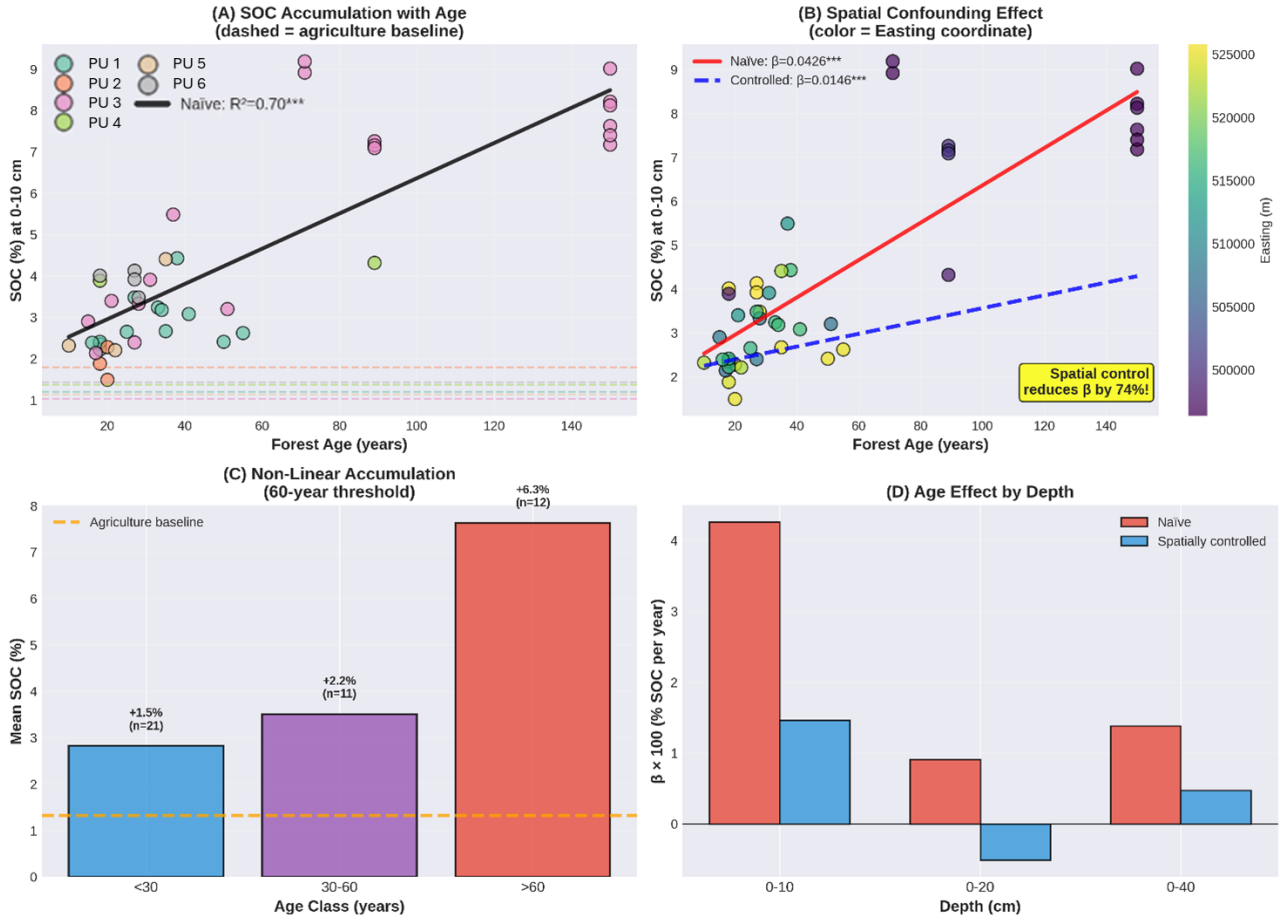

Figure 3.4. Age-related SOC accumulation within forests. (A) SOC vs forest age with agriculture baselines (dashed lines) by PU. Overall naïve regression (black line, $R^2 = 0.70$). (B) Spatial confounding effect: naïve model (red, $\beta = 0.0426$) vs spatially-controlled model (blue dashed, $\beta = 0.0146$). Point colour indicates Easting coordinate showing geographic clustering. (C) Non-linear accumulation pattern with 60-year threshold. Orange dashed line = agriculture baseline (1.32%). (D) Age effect ($\beta \times 100$) by depth for naïve and spatially-controlled models. *** $p < 0.001$.

Nonlinear age effects were detected at surface horizons, with a significant quadratic term at 0-10 and 0-20 cm, indicating accelerated SOC accumulation in older forests (Figure 3.4 C). Forests older than 60 years showed disproportionately high SOC stocks, consistent with a threshold response associated with humus form transitions (Mull → Moder/Mor) and reduced decomposition rates.

Agricultural SOC exhibited minimal spatial clustering across all depths (Appendix Table A4): 0-10 cm (Moran's $I = +0.193$, $p = 0.063$, not significant); 0-20 cm ($I = +0.383$, $p = 0.001$); 0-40 cm ($I = +0.221$, $p = 0.038$). At the surface horizon, agricultural SOC showed no significant spatial clustering, validating the assumption of spatially homogeneous cropland baselines within pedolandscapes.

The contrast with forest spatial structure is striking (Figure 3.5 A,B): Forest is 4.7× more clustered than agriculture at 0-10 cm ($I = +0.901$ vs $+0.193$), and 3.3× more clustered at 0-40 cm ($I = +0.734$ vs $+0.221$). This

asymmetric spatial structure confirms that spatial confounding primarily inflates forest age effects while leaving forest vs agriculture comparisons largely unaffected.

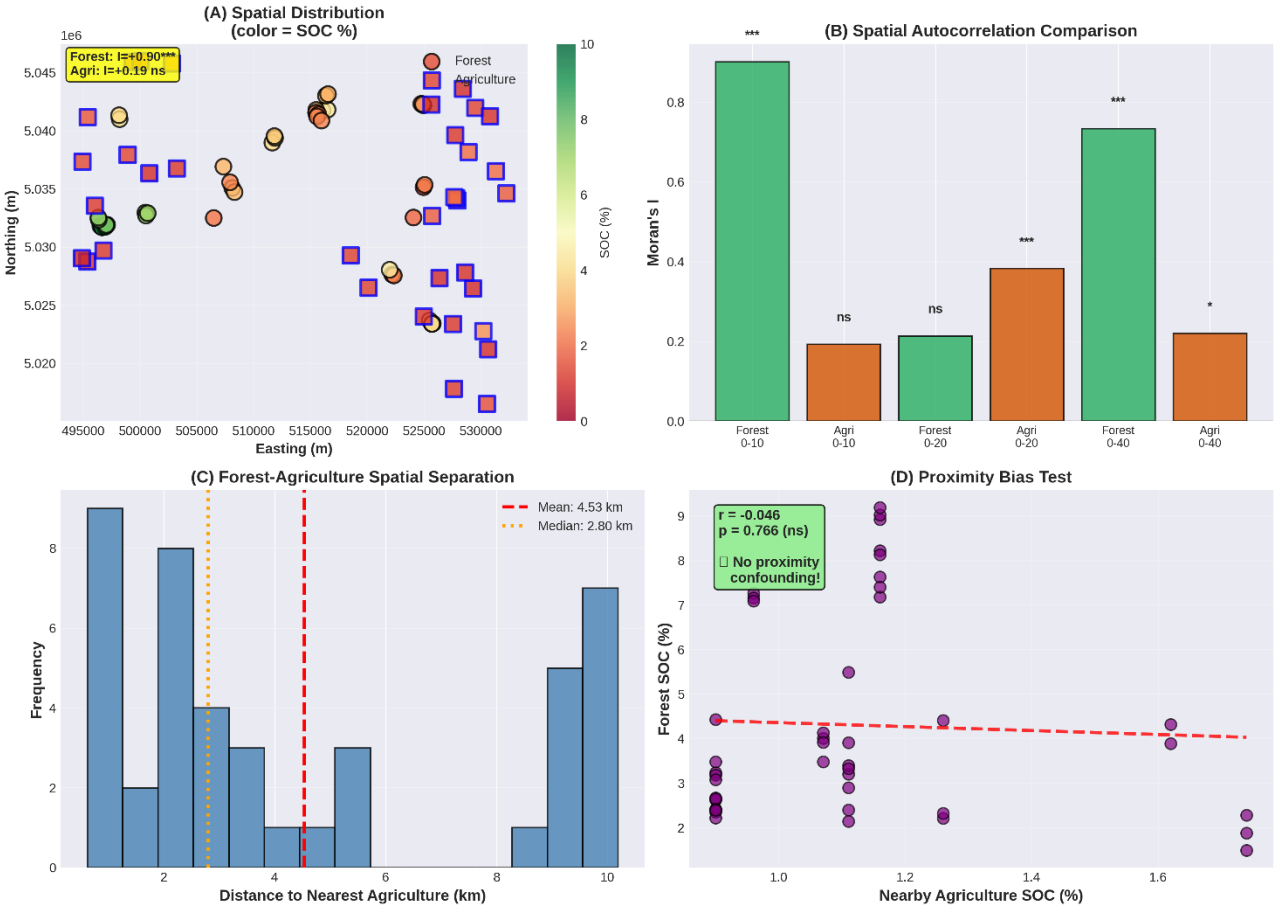

Figure 3.5. Spatial structure and proximity analysis. (A) Spatial distribution map showing forest (circles) and agriculture (squares) sites with SOC color-coded (green = high, red = low). Text box shows Moran's *I* values. (B) Moran's *I* comparison across depths and land uses. Forest exhibits 4.7× stronger spatial clustering than agriculture at 0-10 cm. (C) Distribution of distances from forest plots to nearest agricultural site (mean = 4.5 km, median = 2.8 km). (D) Proximity bias test: no correlation between forest SOC and nearby agriculture SOC (r = -0.046, p = 0.77), validating independence of land-use effects from site selection. *** $p < 0.001$, * $p < 0.05$, ns = not significant.

Forest and agricultural sites exhibited moderate spatial separation (Figure 3.5 C, Appendix Table A5), with mean distance 4.53 ± 2.81 km (range: 0.62-10.19 km). Critically, forest SOC showed no correlation with nearby agricultural SOC (r = -0.046, p = 0.766; Figure 3.5 D), indicating that high-SOC forests were not systematically located near high-SOC cropland. This confirms the forest advantage (+2.98%, +225% at 0-10 cm) reflects genuine land-use effects rather than site selection bias or broad geographic gradients.

Interestingly, forest-agriculture SOC differences decreased with spatial separation (r = -0.301, p = 0.047; Figure 3.6), with closer pairs (<2 km) exhibiting larger differences (+3.5% mean) than distant pairs (>8 km, +2.1% mean). This pattern may reflect edge effects, wherein peri-forest cropland experiences altered management, or greater pedolandscape comparability in proximate pairs. Regardless of mechanism, this

distance effect operates orthogonally to the main comparison (forest SOC independent of agricultural SOC), confirming robustness of afforestation effects.

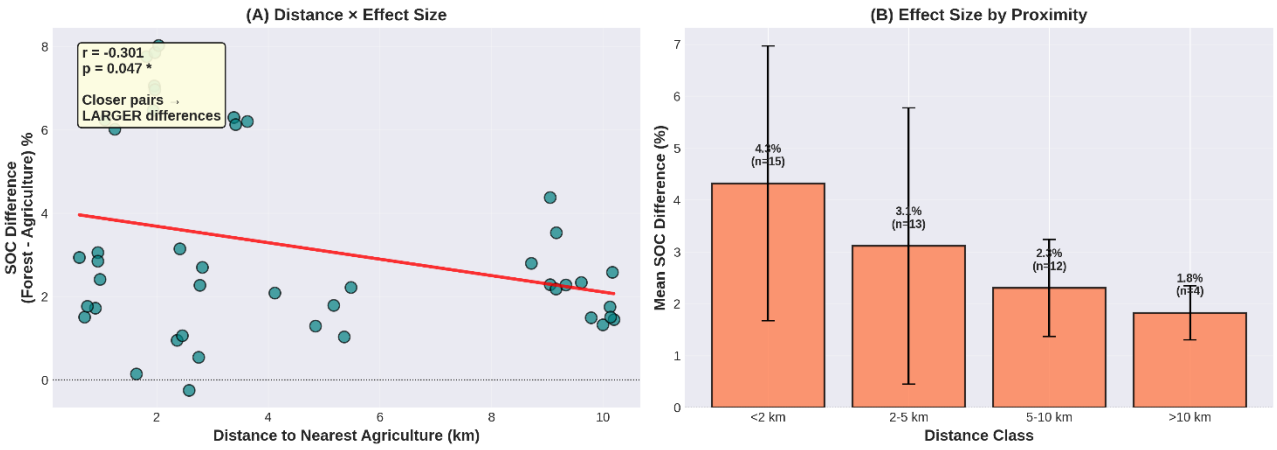

Figure 3.6. Spatial distance effects. (A) Relationship between spatial separation and SOC difference (forest minus agriculture). Closer forest-agriculture pairs exhibit larger differences (r = -0.30, p = 0.047). Red line = linear trend. (B) Mean SOC difference by distance class (<2 km, 2-5 km, 5-10 km, >10 km). Error bars = ±SD, numbers indicate sample size per class. * $p < 0.05$.

3.3 Humus Forms

Humus classification in 44 plots revealed: Mull (n = 31, 70.5%), Moder (n = 7, 15.9%), and Mor (n = 6, 13.6%). Distribution showed very strong association with green area type ($\chi^2 = 44.0$, $p < 0.001$, Cramér's $V = 0.707$), with Mull exclusive to PPf and SUF and Moder or Mor restricted to W.

Humus forms correlated extremely strongly with forest age (Spearman's $\rho = 0.705$, $p < 0.001$): Mull 27.7±11.2 years, Moder 96.3±44.9 years, Mor 123.7±40.8 years (Appendix Table A6).

Figure 3.7 illustrates these soil-humus relationships through boxplots for pH, SOC, avP, and forest age, showing clear separation among the three humus categories. Surface soil pH decreased sharply from Mull (5.61±0.58) to Moder (4.54±0.33) to Mor (3.92±0.12) ($H = 26.4$, $p < 0.001$), a 1.7-unit acidification gradient. All pairwise comparisons differed significantly ($p < 0.017$).

SOC nearly tripled from Mull (3.03±0.89%) to Mor (8.52±0.62%) ($H = 25.5$, $p < 0.001$), with TN increasing similarly (0.27% to 0.68%, $H = 27.1$, $p < 0.001$). C:N ratio increased modestly from 11.33 to 12.57 ($H = 7.5$, $p = 0.024$). AvP was higher in Mull (27.3±13.2 mg kg^{-1}) than Moder/Mor (~15 mg kg^{-1}) ($H = 17.5$, $p < 0.001$), reflecting agricultural legacy and progressive P occlusion. Tree cover increased from 65.2% (Mull) to 85.5% (Mor) ($H = 6.3$, $p = 0.042$) (Appendix Table A6).

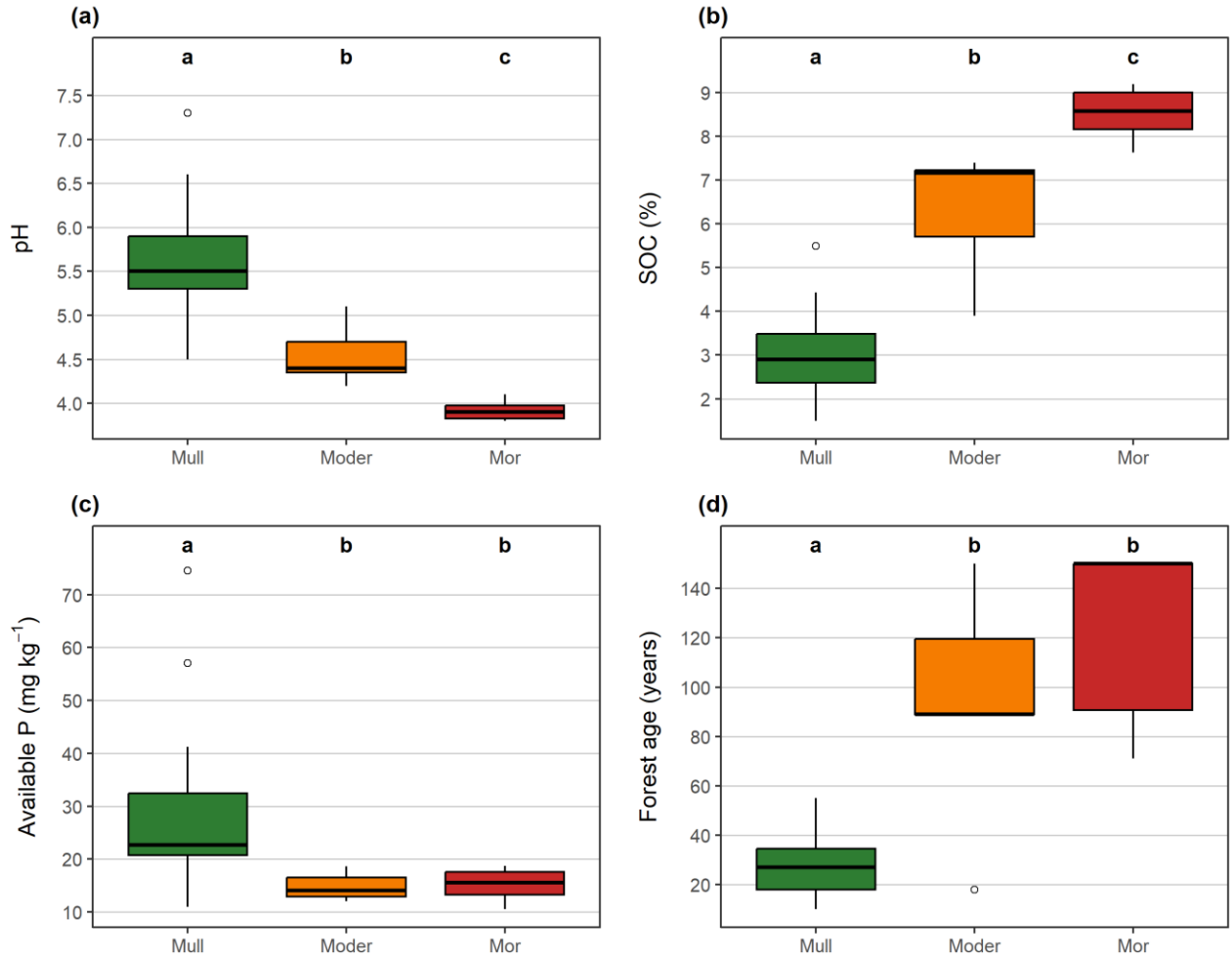

Figure 3.7. Soil property variation across humus forms (Mull, Moder, Mor) in Milan peri-urban forests. Boxplots show: (a) soil pH, (b) SOC (%), (c) available P (mg kg^{-1}), and (d) forest age (years). Boxes represent interquartile range (IQR), horizontal lines indicate medians, whiskers extend to 1.5×IQR, and points show outliers. Different letters indicate significant differences among humus forms based on Kruskal-Wallis tests followed by Dunn's post hoc comparisons ($p < 0.05$).

Stress-tolerant (S) strategies doubled from Mull (17.6±10.5%) to Mor (36.9±7.4%) ($H = 12.0$, $p = 0.003$), while competitive (C) strategies declined from 36.3% to 19.6% ($H = 9.3$, $p = 0.010$). Ruderal (R) strategies showed no trend ($H = 0.9$, $p = 0.629$). Leaf nitrogen content was higher in Moder/Mor (3.44-3.53%) vs. Mull (2.54%) ($H = 8.2$, $p = 0.016$) (Appendix Table A6).

Paradoxically, herbaceous biomass was threefold higher in Moder/Mor (35-39% cover) than Mull (12.7%) ($H = 11.6$, $p = 0.003$), despite lower pH and P availability.

Piecewise structural equation modeling with spatial control (one MEM) tested two alternative causal pathways linking humus forms to herbaceous biomass (indirect vs direct effects; Figure 3.8).

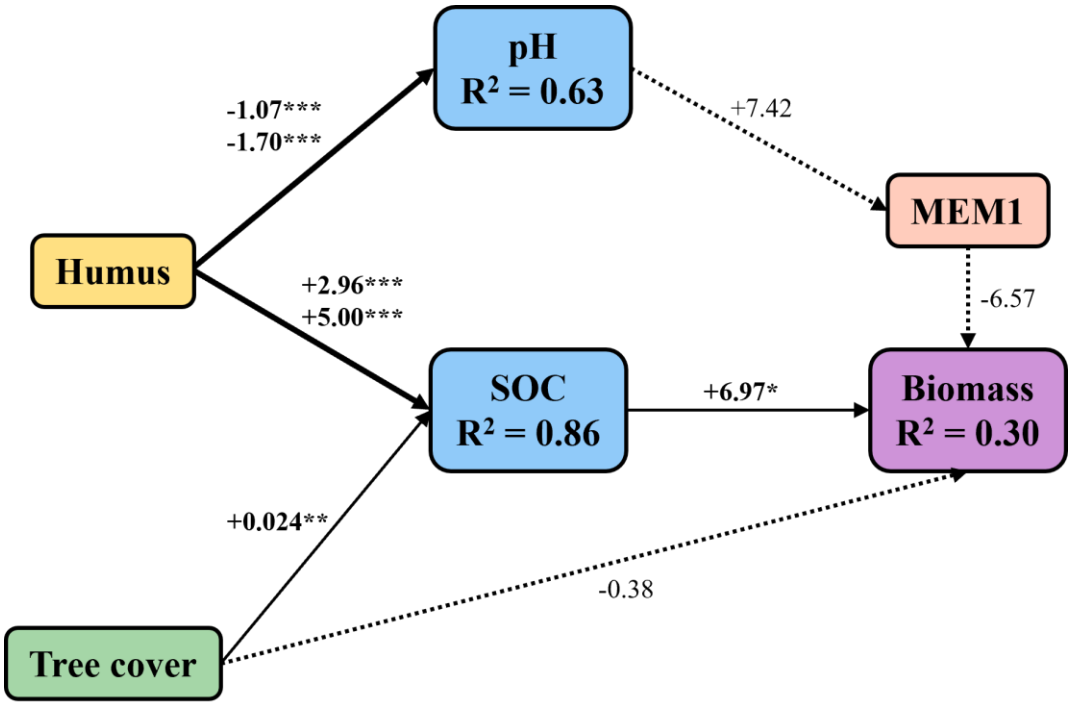

Figure 3.8. Conceptual path diagram for piecewise structural equation models testing alternative pathways linking humus forms to herbaceous biomass. Solid arrows represent the mediation pathway (Model 1: Humus → Soil chemistry [pH, SOC] → Biomass), while dashed arrows represent additional direct pathways tested in Model 2 (Humus + covariates → Biomass). Arrow thickness proportional to standardized path coefficients; significant paths (*** $p < 0.001$; ** $p < 0.01$; * $p < 0.05$) shown in bold. Tree cover influences both SOC accumulation and biomass directly (light competition). One Moran's Eigenvector Map (MEM) included as spatial control covariate. R^2 values indicate variance explained in each endogenous variable.

The mediation model (Model 1: Humus → Soil chemistry → Biomass) showed excellent fit (Fisher's $C = 10.1$, df = 12, $p = 0.61$, AIC = 595.9) and was preferred over the direct effects model (Model 2; Fisher's $C = 16.4$, df = 12, $p = 0.18$, AIC = 600.3; ΔAIC = 4.4), indicating full mediation of humus effects by soil chemistry. Residuals of both models showed no significant spatial autocorrelation (Moran's I $p > 0.75$), confirming successful removal of spatial structure.

In the selected mediation model, humus forms strongly predicted soil chemistry. The Humus → pH pathway explained 63% of variance, with Moder and Mor showing progressive acidification relative to Mull. The Humus + tree cover → SOC pathway explained 86% of SOC variance, with Moder and Mor accumulating substantially more carbon than Mull, and tree cover contributing independently but weakly.

Among soil properties, SOC emerged as the primary driver of herbaceous biomass after spatial control ($\beta = 6.97$, $p = 0.011$; Figure 3.8), whereas pH showed no significant direct effect and tree cover had a marginally negative influence. No direct humus-to-biomass effects remained once soil chemistry was accounted for, confirming complete mediation.

Path coefficients were largely stable after spatial control: Humus → pH and Humus → SOC relationships were unchanged, while the SOC → Biomass effect was reduced but remained significant, indicating that spatial structure inflated effect size but not inference. Model R^2 values highlighted strong explanatory power for soil

chemistry (pH: 0.63; SOC: 0.86) and moderate explanatory power for biomass (R^2 = 0.30), consistent with additional unmeasured controls on understory productivity (Figure 3.8).

Variance partitioning showed that environmental variables explained 31.1% of biomass variation, whereas pure spatial effects were negligible. The shared spatial-environmental fraction reflected the geographic clustering of humus forms and associated soil properties, rather than residual spatial confounding. Accordingly, spatially controlled models outperformed non-spatial models (ΔAIC = 9.1), confirming that SOC-mediated humus effects on vegetation are robust to spatial structure.

3.4 Soil-Vegetation Relationships

Surface soil properties (0-10 cm) showed strongest associations with functional traits across all analyses. RLQ explained 42% covariance for continuous traits and 18% for CSR strategies at 0-10 cm, with progressively weaker associations at deeper layers.

C strategies associated positively with avP (β = 0.45, p = 0.001), while S strategies correlated negatively with P (β = -0.32, p = 0.012) and positively with tree cover (β = 0.28, p = 0.019). R strategies showed no environmental associations ($p > 0.05$).

Preliminary analysis revealed significant spatial autocorrelation in key variables across the study area (spatial extent: 29.4 × 19.8 km). Moran's I statistics indicated strong spatial clustering for SOC (I = 0.77, $p < 0.001$), forest age (I = 0.69, $p < 0.001$), pH (I = 0.51, $p < 0.001$), tree cover (I = 0.27, $p < 0.001$), and herbaceous biomass (I = 0.21, p = 0.006). Humus forms themselves showed pronounced spatial clustering (Mull: I = 0.81, Moder: I = 0.55, Mor: I = 0.74, all $p < 0.001$), reflecting geographic concentration of mature woodlands in the northern and western portions of the study area and younger peri-urban parks in central and eastern zones.

To control for spatial confounding, forward selection identified one significant Moran's Eigenvector Map (MEM) explaining 14.2% of herbaceous biomass variation (p = 0.012). This MEM was included as a covariate in subsequent structural equation models. Spatial connectivity was defined using a Gabriel graph neighborhood structure, which connected plots where no other plot fell within the circle defined by the distance between the two focal plots. This approach yielded a mean of 2.3 neighbors per site (range: 1-4), providing conservative spatial weighting appropriate for irregularly-distributed plots across the metropolitan landscape.

In RLQ environmental ordination (Figure 3.9), PC1 (59.3% variance) represented a maturity/acidification gradient with strong loadings for SOC (+0.49), TN (+0.49), Humus_Mor (+0.38), and pH (-0.43). PC2 (15.8%) distinguished Moder (+0.77) from Mor (-0.52). The PCA biplot (Figure 3.9) illustrates the clear ordination of plots by humus type along the first principal component, with Mull plots clustering toward the left (high pH, low SOC, high P) and Moder/Mor plots toward the right (low pH, high SOC, low P).

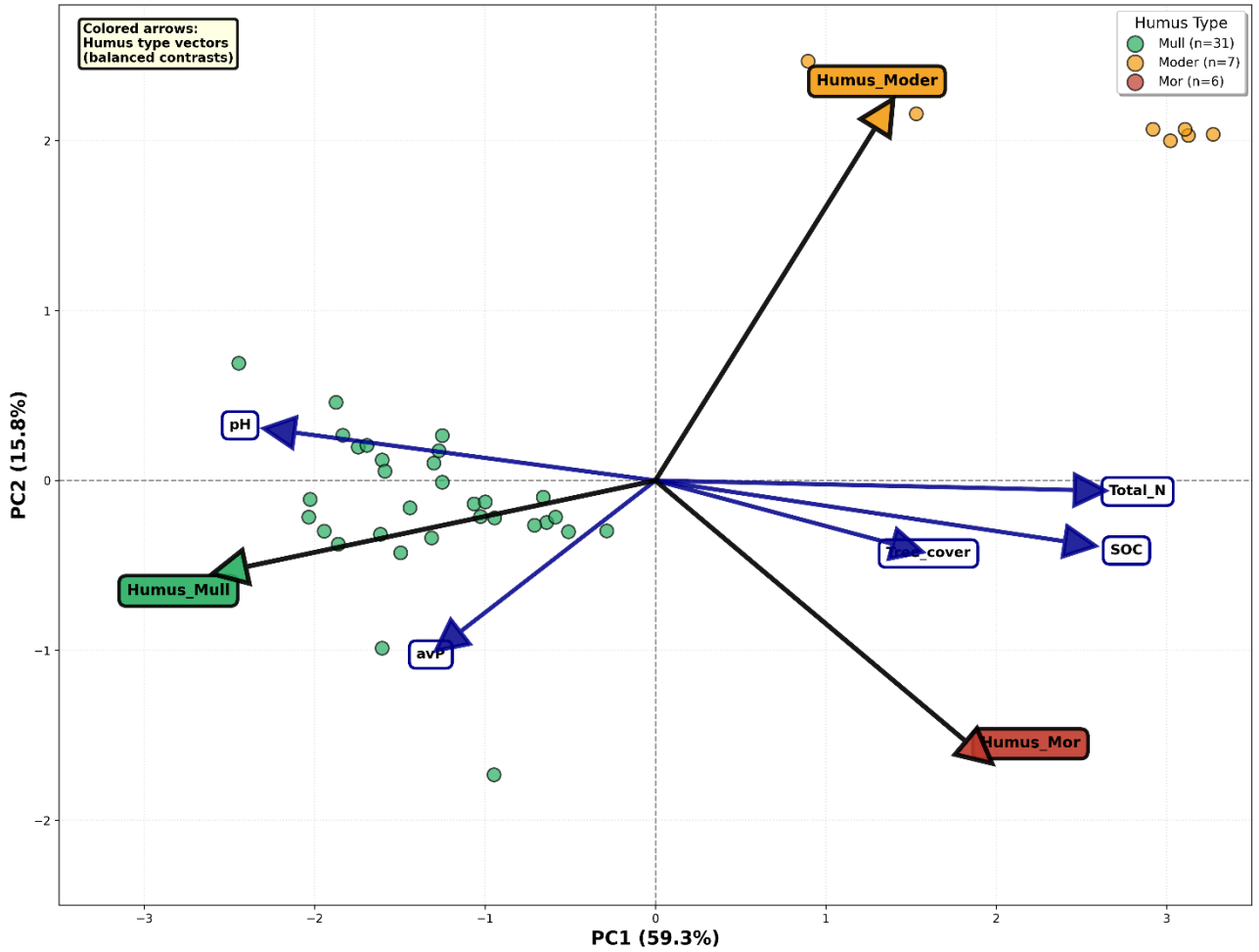

Figure 3.9. Environmental ordination (PCA of R matrix) from RLQ analysis. This represents the environmental space in which trait-environment relationships were tested using fourth-corner analysis. PC1 (59.3% variance) represents a maturity/acidification gradient with positive loadings for SOC, total N, and Humus_Mor, and negative loading for pH. PC2 (15.8% variance) distinguishes Moder from Mor. Points represent individual plots colored by humus type (Mull: green, Moder: orange, Mor: red). Arrows indicate environmental variable loadings. Clear spatial separation of humus types along PC1 confirms their role as integrative indicators of soil development.

Fourth-corner analysis revealed significant humus-trait associations (Appendix Table A7). Humus_Mor showed strong negative correlation with C-strategies (ρ = -0.43, p = 0.003) and positive with S-strategies (ρ = +0.45, p = 0.002), remaining significant after FDR correction. LNC showed marginal positive correlations with both Humus_Moder and Humus_Mor (ρ = +0.28-0.29, p = 0.060-0.069).

SLA correlated positively with avP (β = 0.38, p = 0.003) and negatively with tree cover (β = -0.29, p = 0.015). LDMC and LMA associated negatively with both avP (β = -0.35 to -0.41, p = 0.002-0.007) and tree cover (β = -0.30 to -0.33, p = 0.009-0.011). LNC correlated with TN (β = 0.40, p = 0.004).

4. Discussion

4.1 Carbon Sequestration in Urban Reforestation

Our study demonstrates that afforestation of former agricultural lands in urban and peri-urban contexts leads to substantial increases in SOC. Across depths, forest soils contained substantially more SOC than agricultural soils (119-225%), with very large effect sizes (Cohen's d = 1.7-2.0), indicating that urban and peri-urban reforestation can deliver SOC increases comparable to long-term temperate forest recovery (Cohen, 1988). The largest absolute increases occurred in the surface layer (0-10 cm), consistent with a top-down mechanism driven by litter inputs and near-surface stabilization processes. Importantly, forest effects extended to 40 cm, suggesting that SOC gains are not confined to the organic layer but involve the mineral profile as well (Rumpel & Kögel-Knabner, 2011; Jackson *et al.*, 1996).

Pedolandscape context explained a large share of SOC variability, underscoring that baseline SOC and SOC response potential are strongly conditioned by soil-landscape properties. Agricultural SOC differed among PUs (1.02-1.79%), and forest responses varied markedly across PUs, emphasizing the need to compare forest and cropland within the same pedolandscape context to avoid conflating land-use and site effects.

Among the considered pedolandscape units, PU3 - which includes the widest forest age range (15-150 years) - provides a particularly informative sequence for interpreting long-term SOC dynamics. However, the present study adopts a comparative, multi-site framework aimed at capturing general patterns across pedolandscape units rather than focusing on a single chronosequence. While a dedicated analysis of PU3 could further refine the interpretation of long-term trajectories, the consistent patterns observed across units support the robustness of the overall findings.

Within forests, SOC increased with stand age, but the strength and form of this relationship depended on spatial structure: models accounting for spatial autocorrelation yielded substantially lower age-related accumulation rates than spatially naïve analyses. The relationship was non-linear, with stronger accumulation in stands older than ~60 years, consistent with progressive organic horizon development and reduced decomposition rates in more mature systems (Ponge, 2003; Poeplau *et al.*, 2011). This pattern cautions against extrapolating linear age-SOC relationships to infer long-term sequestration.

From a management perspective, these results support (i) protection of existing mature urban woodlands, where SOC gains are greatest, and (ii) carbon inventories that sample beyond surface soil (≥30-40 cm). Because cropland reference soils maintained moderate SOC levels, the observed increases reflect conversion to a higher-carbon ecosystem rather than recovery from severely degraded conditions. Key limitations include the cross-sectional (space-for-time) design and potential contributions of unmeasured factors (e.g., tree composition, planting density, understory management), which warrant validation through longitudinal monitoring.

4.2 Pedogenic Trajectories and Humus Development

Soil properties showed consistent age-related trends indicative of progressive pedogenic transformation following urban afforestation. SOC and TN increased strongly with stand age in surface soils and remained

significant at 0-40 cm, while intermediate depths showed weaker associations, consistent with slower subsurface response and buffering by agricultural legacies (Jobbágy & Jackson, 2000). Increasing C:N ratios with age suggest accumulation of more recalcitrant organic matter typical of mature forest systems (Laganière *et al.*, 2010). The pH decline with age is consistent with acidification driven by organic acids and cation leaching during long-term biomass accumulation (Augusto *et al.*, 2002), while avP depletion likely reflects immobilization and sorption processes observed in temperate chronosequences (Turner & Condron, 2013).

Humus forms were strongly associated with forest age, supporting humus classification as an integrative indicator of ecosystem development. The prevalence of Mull in younger plantations and Moder/Mor in older woodlands reflects a shift toward slower decomposition and greater organic horizon development (Ponge, 2003; Zanella *et al.*, 2011). The associated gradients in pH and SOC align with successional theory linking decomposer communities and litter quality to organic matter dynamics (Wardle *et al.*, 2004). The strong association between humus form and green area type further suggests that young urban forests retain agricultural legacies, whereas protected mature woodlands converge toward conditions typical of long-established forests.

4.3 Humus-Mediated Vegetation Relationships

Humus forms were linked to understory composition through both soil-mediated and (potentially) direct pathways. Humus explained substantial variation in soil pH and SOC, consistent with humus morphology integrating multiple soil processes beyond routine chemistry (e.g., structure, faunal activity, moisture dynamics) (Zanella *et al.*, 2011). Along this gradient, acidification and SOC accumulation were associated with functional shifts from competitive to stress-tolerant strategies, consistent with trait-based theory and conservative resource-use strategies under low pH and nutrient limitation (Wright *et al.*, 2004).

Model comparisons indicate that humus effects on herbaceous biomass were primarily mediated through soil chemistry once spatial structure was controlled. After accounting for spatial autocorrelation, the mediation model showed better support than a direct-effects formulation, and direct humus coefficients were not statistically significant when soil variables were included. Together with SAR-based robustness checks, these results support a mechanistic interpretation in which humus influences understory productivity mainly through linked changes in SOM accumulation and acidification rather than geographic clustering or unmeasured biotic effects.

Notably, herbaceous biomass was higher in Moder/Mor plots than in Mull plots despite lower pH and avP. This pattern may reflect improved moisture buffering and nutrient retention in thicker organic horizons, coupled with a shift in species composition toward shade-adapted, conservative strategists capable of maintaining biomass under resource limitation (Wardle *et al.*, 2004; Grime, 1977). Canopy cover effects were comparatively weak, suggesting that soil-mediated filtering outweighed light limitation within the range of canopy conditions sampled.

4.4 Trait-Environment Relationships

Trait-environment relationships were strongest for surface soil properties (0-10 cm), consistent with shallow herbaceous rooting and intense litter-soil interactions near the surface (Schenk & Jackson, 2002). Available P emerged as a key environmental filter, with higher avP associated with acquisitive traits (higher SLA and C-strategies) and lower avP associated with conservative traits (higher LDMC/LMA), consistent with the leaf economics spectrum (Wright *et al.*, 2004). However, lower avP in mature Moder/Mor stands, alongside higher biomass and higher leaf N content, suggests that productivity cannot be explained by P availability alone. Instead, humus-mediated changes in soil structure and organic matter dynamics likely modulate resource availability and trait composition in ways that decouple simple nutrient-productivity expectations.

Across models, environmental filtering explained substantially more variation in traits and biomass than spatial structure, supporting the predominance of local soil conditions over dispersal limitation in shaping understory functional composition (Freschet *et al.*, 2017).

4.5 Soil Depth and Rooting Zone

Focusing multivariate analyses on surface soil (0-10 cm) was supported by stronger soil–vegetation associations at this depth. Nevertheless, forest age effects on key soil properties extended throughout the profile, including significant age-related changes in SOC, TN, and pH at 0-40 cm. The weaker signal at 0-20 cm may reflect transitional dynamics in subsurface recovery rather than ecological irrelevance. While our results capture shallow rhizosphere processes relevant to herbaceous communities, deeper horizons may become increasingly important for drought resilience, woody regeneration, and slow-turnover nutrient pools. Future studies integrating depth-weighted properties and root distribution data would help generalize trait–environment relationships across functional groups and soil depths.

4.6 Management and Conservation Implications

Our findings have practical implications for urban forest planning and restoration. First, protecting mature urban woodlands is critical, as the largest SOC gains and most developed humus systems occur in older stands. Second, restoration strategies should recognize that pedolandscape context constrains achievable trajectories; newly established forests should be evaluated against realistic successional benchmarks rather than assuming rapid convergence to ancient woodland conditions. Third, humus morphology offers a rapid, field-assessable indicator that integrates multiple soil functions and can support monitoring of soil development and understory changes (Zanella *et al.*, 2011). Management actions that retain litter and minimize disturbance may accelerate organic horizon development and enhance long-term SOC storage, while excessive soil disruption could reset humus trajectories and associated understory assemblages. Climate change may further modulate these processes through altered decomposition and nutrient cycling, highlighting the need for adaptive monitoring.

4.7 Limitations and Future Directions

Several limitations warrant consideration. Our trait dataset focused on aboveground traits; incorporating root traits and microbial indicators would improve mechanistic inference regarding decomposition and nutrient cycling (Freschet *et al.*, 2021). The study is confined to one biogeographic region with specific edaphic and land-use histories; replication across metropolitan regions would test generality. The cross-sectional design limits causal inference, and longitudinal monitoring is needed to confirm humus transitions and SOC trajectories over time. Sample sizes for Moder and Mor were relatively small, potentially limiting statistical power, and expanding sampling in mature woodlands would improve precision. Finally, strong covariation among humus form, forest age, and green area category complicates attribution of unique effects; targeted comparisons within age classes and natural experiments (e.g., contrasting tree species within similar pedolandscape contexts) would help isolate drivers.

5. Conclusions

This study provides comprehensive evidence that urban and peri-urban afforestation on former agricultural lands in the Milan metropolitan area drives substantial pedogenic changes and shapes understory vegetation composition through soil-mediated pathways. Our findings address critical knowledge gaps in urban forest ecology and offer practical insights for restoration management.

First, urban forests accumulated 119-225% more SOC than paired agricultural reference soils, with gains persisting to 40 cm depth. SOC increased nonlinearly with forest age, with accelerated accumulation in stands older than 60 years coinciding with humus form transitions from Mull to Moder/Mor. Critically, spatial autocorrelation inflated naïve age-SOC estimates by approximately 74%, underscoring the necessity of explicit spatial control in observational studies of urban forests.

Second, humus form classification emerged as a powerful integrative indicator of pedogenic development, explaining 63-86% of variance in soil pH and SOC. The strong association between humus forms and forest age (ρ = 0.705) confirms that morphological classification captures successional trajectories from mineralization-dominated (Mull) to accumulation-dominated (Moder/Mor) systems. The exclusive occurrence of Moder and Mor in mature woodlands (>60 years) reflects centuries-long pedogenic processes that cannot be replicated through short-term management interventions.

Third, piecewise structural equation modeling with spatial control demonstrated that humus effects on herbaceous biomass operate primarily through soil chemistry mediation (SOC accumulation and acidification) rather than through direct unmeasured pathways. The mediation model achieved superior fit over the direct effects model, indicating that routine soil analyses (pH, SOC) capture the mechanistic pathways linking humus development to vegetation composition.

Fourth, trait-environment relationships revealed that available phosphorus and soil pH act as primary environmental filters on understory functional composition. C strategies associated positively with P availability, while S strategies increased with soil acidification in mature Moder/Mor systems. Surface soil

properties (0-10 cm) showed the strongest associations with herbaceous traits, consistent with shallow rooting patterns and the concentration of litter-soil interactions at the surface.

These findings carry direct implications for urban forest management and conservation. Maximum carbon sequestration benefits are achieved in forests older than 60 years, highlighting the irreplaceable value of protecting existing mature urban woodlands. Humus morphology provides a rapid, field-assessable proxy for monitoring pedogenic development without requiring laboratory analyses. Restoration strategies should prioritize litter retention, native species producing recalcitrant litter, and minimized disturbance to facilitate progressive soil development.

The substantial spatial structure documented across the metropolitan landscape-with mature Moder/Mor systems concentrated in ancient forest remnants-provides a biogeographic template for conservation prioritization. However, this spatial clustering also represents a fundamental constraint: newly established plantations should not be expected to rapidly converge with ancient forest conditions, and restoration targets must be calibrated to realistic successional trajectories spanning decades to centuries.

Future research should incorporate root traits and microbial community composition to better link humus dynamics with belowground processes, extend sampling to additional metropolitan regions to assess generalizability, and establish longitudinal monitoring to track humus form transitions and validate the chronosequence-based inferences presented here.

References

Augusto, L., Ranger, J., Binkley, D., & Rothe, A. (2002). Impact of several common tree species of European temperate forests on soil fertility. *Annals of Forest Science*, 59(3), 233-253. https://doi.org/10.1051/forest:2002020.

Benjamini, Y., & Hochberg, Y. (1995). Controlling the False Discovery Rate: a practical and powerful approach to multiple testing. *Journal of the Royal Statistical Society: Serie B (Methodological)*, 57(1), 289-300. https://doi.org/10.1111/j.2517-6161.1995.tb02031.x.

Berg, B., & McClaugherty, C. (2014). Plant litter: decomposition, humus formation, carbon sequestration (3rd ed.). Springer-Verlag, Berlin, Heidelberg. https://doi.org/10.1007/978-3-642-38821-7.

Borcard, D., Legendre, P., & Dray, S. (2011). *Numerical Ecology with R*. Springer. https://doi.org/10.1007/978-1-4419-7976-6.

Cambou, A., Shaw, R. K., Huot, H., Vidal-Beaudet, L., Hunault, G., Cannavo, P., Nold, F., & Schwartz, C. (2018). Estimation of soil organic carbon stocks of two cities, New York City and Paris. *Science of The Total Environment*, 644, 452-464. https://doi.org/10.1016/j.scitotenv.2018.06.322.

Canedoli, C., Ferrè, C., Abu El Khair, D., Padoa-Schioppa, E., & Comolli, R. (2020). Soil organic carbon stock in different urban land uses: high stock evidence in urban parks. *Urban Ecosystems*, 23(1), 159-171. https://doi.org/10.1007/s11252-019-00901-6.

Churkina, G., Brown, D. G., & Keoleian, G. (2010). Carbon stored in human settlements: the conterminous United States. *Global Change Biology*, 16(1), 135-143. https://doi.org/10.1111/j.1365-2486.2009.02002.x.

Cohen, J. (1988). Statistical Power Analysis for the Behavioral Sciences (2nd ed.). Lawrence Erlbaum Associates. https://doi.org/10.4324/9780203771587.

Cornelissen, J. H. C., Lavorel, S., Garnier, E., Díaz, S., Buchmann, N., Gurvich, D. E., Reich, P. B., ter Steege, H., Morgan, H. D., van der Heijden, M. G. A., Pausas, J. G., & Poorter, H. (2003). A handbook of protocols for standardised and easy measurement of plant functional traits worldwide. *Australian Journal of Botany*, 51(4), 335-380. https://doi.org/10.1071/BT02124.

Don, A., Schumacher, J., & Freibauer, A. (2011). Impact of tropical land-use change on soil organic carbon stocks - a meta-analysis. *Global Change Biology*, 17(4), 1658-1670. https://doi.org/10.1111/j.1365-2486.2010.02336.x.

Dormann, C. F., McPherson, J. M., Araújo, M. B., Bivand, R., Bolliger, J., Carl, G., Davies, R. G., Hirzel, A., Jetz, W., Kissling, W. D., Kühn, I., Ohlemüller, R., Peres-Neto, P. R., Reineking, B., Schröder, B., Schurr, F. M., Wilson, R. (2007). Methods to account for spatial autocorrelation in the analysis of species distributional data: a review. *Ecography*, 30(5), 609-628. https://doi.org/10.1111/j.2007.0906-7590.05171.x.

Dray, S., Legendre, P., & Peres-Neto, P. R. (2006). Spatial modelling: a comprehensive framework for principal coordinate analysis of neighbour matrices (PCNM). *Ecological Modelling*, 196(3-4), 483-493. https://doi.org/10.1016/j.ecolmodel.2006.02.015.

Dray, S., Choler, P., Dolédec, S., Peres-Neto, P. R., Thuiller, W., Pavoine, S., & ter Braak, C. J. F. (2014). Combining the fourth-corner and the RLQ methods for assessing trait responses to environmental variation. *Ecology*, 95(1), 14-21. https://doi.org/10.1890/13-0196.1.

Freschet, G. T., Violle, C., Bourget, M. Y., Scherer-Lorenzen, M., & Fort, F. (2017). Allocation, morphology, physiology, architecture: the multiple facets of plant above- and below-ground responses to resource stress. *New Phytologist*, 219(4), 1338-1352. https://doi.org/10.1111/nph.15225.

Freschet, G. T., Roumet, C., Comas, L. H., Weemstra, M., Bengough, A. G., Rewald, B., Bardgett, R. D., De Deyn, G. B., Johnson, D., Klimešová, J., Lukac, M., McCormack, M. L., Meier, I. C., Pagès, L., Poorter, H., Prieto, I., Wurzburger, N., Zadworny, M., Bagniewska-Zadworna, A., Blancaglor, E. B., Brunner, I., Gessler, A., Hobbie, S. E., Iversen, C. M., Mommer, L., Picon-Cochard, C., Postma, J. A., Rose, L., Ryser, P., Scherer-Lorenzen, M., Soudzilovskaia, N. A., Sun, T., Valverde-Barrantes, O. J., Weigelt, A., York, L. M., & Stokes, A. (2021). Root traits as drivers of plant and ecosystem functioning: current understanding, pitfalls and future research needs. *New Phytologist*, 232(3), 1123-1158. https://doi.org/10.1111/nph.17072.

Gentili, R., Ferrè, C., Cardarelli, E., Montagnani, C., Bogliani, G., Citterio, S., & Comolli, R. (2019). Comparing negative impacts of *Prunus serotina*, *Quercus rubra* and *Robinia pseudoacacia* on native forest ecosystems. *Forests*, 10(10), 842. https://doi.org/10.3390/f10100842.

Grime, J. P. (1977). Evidence for the existence of three primary strategies in plants and its relevance to ecological and evolutionary theory. *The American Naturalist*, 111(982), 1169-1194. https://doi.org/10.1086/283244.

Guo, L. B., & Gifford, R. M. (2002). Soil carbon stocks and land use change: a meta analysis. *Global Change Biology*, 8(4), 345-360. https://doi.org/10.1046/j.1354-1013.2002.00486.x.

Jabiol, B., Zanella, A., Ponge, J. F., Sartori, G., Englisch, M., van Delft, B., de Waal, R., & Le Bayon, R. C. (2013). A proposal for including humus forms in the World Reference Base for Soil Resources (WRB-FAO). *Geoderma*, 192, 286-294. https://doi.org/10.1016/j.geoderma.2012.08.002.

Jackson, R. B., Canadell, J., Ehleringer, J. R., Mooney, H. A., Sala, O. E., & Schulze, E. D. (1996). A global analysis of root distributions for terrestrial biomes. *Oecologia*, 108(3), 389-411. https://doi.org/10.1007/BF00333714.

Jobbágy, E. G., & Jackson, R. B. (2000). The vertical distribution of soil organic carbon and its relation to climate and vegetation. *Ecological Applications*, 10(2), 423-436. https://doi.org/10.1890/1051-0761(2000)010[0423:TVDOSO]2.0.CO;2.

Laganière, J., Angers, D. A., & Paré, D. (2010). Carbon accumulation in agricultural soils after afforestation: a meta-analysis. *Global Change Biology*, 16(1), 439-453. https://doi.org/10.1111/j.1365-2486.2009.01930.x.

Lefcheck, J. S. (2016). PiecewiseSEM: Piecewise structural equation modelling in R for ecology, evolution, and systematics. *Methods in Ecology and Evolution*, 7(5), 573-579. https://doi.org/10.1111/2041-210X.12512.

Legendre, P., Galzin, R., & Harmelin-Vivien, M. L. (1997). Relating behaviour to habitat: solutions to the fourth-corner problem. *Ecology*, 78(2), 547-562. https://doi.org/10.1890/0012-9658(1997)078[0547:RBTHST]2.0.CO;2.

Mayer, M., Prescott, C. E., Abaker, W. E. A., Augusto, L., Cécillon, L., Ferreira, G. W. D., James, J., Jandl, R., Katzensteiner, K., Laclau, J.-P., Laganière, J., Nouvellon, Y., Paré, D., Stanturf, J. A., Vanguelova, E. I., & Vesterdal, L. (2020). Tamm review: Influence of forest management activities on soil organic carbon stocks: A knowledge synthesis. *Forest Ecology and Management*, 466, 118127. https://doi.org/10.1016/j.foreco.2020.118127.

Morel, J. L., Chenu, C., & Lorenz, K. (2015). Ecosystem services provided by soils of urban, industrial, traffic, mining, and military areas (SUITMAs). *Journal of Soils and Sediments*, 15(8), 1659-1666. https://doi.org/10.1007/s11368-014-0926-0.

Olsen, S. R., & Dean, L. R. (1965). Phosphorus. In C. A. Black (Ed.), Methods of soil analysis: Part 2 Chemical and microbiological properties (pp. 1035-1049). American Society of Agronomy, Madison, WI.

Peres-Neto, P. R., Legendre, P., Dray, S., & Borcard, D. (2006). Variation partitioning of species data matrices: estimation and comparison of fractions. *Ecology*, 87(10), 2614-2625. https://doi.org/10.1890/0012-9658(2006)87[2614:VPOSDM]2.0.CO;2.

Pierce, S., Negreiros, D., Cerabolini, B. E. L., Kattge, J., Díaz, S., Kleyer, M., Shipley, B., Wright, S. J., Soudzilovskaia, N. A., Onipchenko, V. G., van Bodegom, P. M., Frenette-Dussault, C., Weiher, E., Pinho, B. X., Cornelissen, J. H. C., Grime, J. P., Thompson, K., Hunt, R., Wilson, P. J., Buffa, G., Nyakunga, O. C., Reich, P. B., Caccianiga, M., Mangili, F., Ceriani, R. M., Luzzaro, A., Brusa, G., Siefert, A., Barbosa, N. P. U., Chapin, F. S., III, Cornwell, W. K., Fang, J., Fernandes, G. W., Garnier, E., Le Stradic, S., Peñuelas, J., Melo, F. P. L., Slaviero, A., Tabarelli, M. & Tampucci, D. (2017). A global method for calculating plant CSR ecological strategies applied across biomes world-wide. *Functional Ecology*, 31(2), 444-457. https://doi.org/10.1111/1365-2435.12722.

Poeplau, C., Don, A., Vesterdal, L., Leifeld, J., Van Wesemael, B., Schumacher, J., & Gensior, A. (2011). Temporal dynamics of soil organic carbon after land-use change in the temperate zone - carbon response functions as a model approach. *Global Change Biology*, 17(7), 2415-2427. https://doi.org/10.1111/j.1365-2486.2011.02408.x.

Ponge, J. F. (2003). Humus forms in terrestrial ecosystems: a framework to biodiversity. *Soil Biology and Biochemistry*, 35(7), 935-945. https://doi.org/10.1016/S0038-0717(03)00149-4.

Pouyat, R. V., Yesilonis, I. D., & Nowak, D. J. (2006). Carbon storage by urban soils in the United States. *Journal of Environmental Quality*, 35(4), 1566-1575. https://doi.org/10.2134/jeq2005.0215.

R Core Team (2025) R: A Language and Environment for Statistical Computing. *R Foundation for Statistical Computing*. https://www.r-project.org/.

Reich, P. B. (2014). The world-wide 'fast-slow' plant economics spectrum: a traits manifesto. *Journal of Ecology*, 102(2), 275-301. https://doi.org/10.1111/1365-2745.12211.

Resemini, R., Geroldi, C., Capotorti, G., De Toni, A., Parisi, F., De Sanctis, M., Cabai, T., Rossini, M., Vignali, L., Poli, M. U., Lo Piccolo, E., Mariotti, B., Arcidiacono, A., Biella, P., Alghisi, E., Bani, L., Bertini, M., Blasi, C., Buffi, F., ..., & Gentili, R. (2025). Building greener cities together: urban afforestation requires multiple

skills to address social, ecological, and climate challenges. *Plants*, 14(3), 404. https://doi.org/10.3390/plants14030404.

Rumpel, C., & Kögel-Knabner, I. (2011). Deep soil organic matter - a key but poorly understood component of terrestrial C cycle. *Plant and Soil*, 338(1), 143-158. https://doi.org/10.1007/s11104-010-0391-5.

Salbitano, F., Borelli, S., Conigliaro, M., & Chen, Y. (2016). Guidelines on urban and peri-urban forestry. FAO Forestry Paper No. 178. Food and Agriculture Organization of the United Nations, Rome.

Schenk, H. J., & Jackson, R. B. (2002). Rooting depths, lateral root spreads and belowground/above-ground allometries of plants in water-limited ecosystems. *Journal of Ecology*, 90(3), 480-494. https://doi.org/10.1046/j.1365-2745.2002.00682.x.

Schittko, C., Bernard-Verdier, M., Heger, T., Buchholz, S., Kowarik, I., von der Lippe, M., Seitz, B., Joshi, J., & Jeschke, J. M. (2020). A multidimensional framework for measuring biotic novelty: How novel is a community? *Global Change Biology*, 26(8), 4401-4417. https://doi.org/10.1111/gcb.15140.

Turner, B. L., & Condron, L. M. (2013). Pedogenesis, nutrient dynamics, and ecosystem development: the legacy of T.W. Walker and J.K. Syers. *Plant and Soil*, 367(1-2), 1-10. https://doi.org/10.1007/s11104-013-1750-9.

Vasenev, V. I., Stoorvogel, J. J., Vasenev, I. I., & Valentini, R. (2014). How to map soil organic carbon stocks in highly urbanized regions? *Geoderma*, 226-227, 103-115. https://doi.org/10.1016/j.geoderma.2014.03.007.

Wardle, D. A., Bardgett, R. D., Klironomos, J. N., Setälä, H., van der Putten, W. H., & Wall, D. H. (2004). Ecological linkages between aboveground and belowground biota. *Science*, 304(5677), 1629-1633. https://doi.org/10.1126/science.1094875.

Wright, I. J., Reich, P. B., Westoby, M., Ackerly, D. D., Baruch, Z., Bongers, F., Cavender-Bares, J., Chapin, T., Cornelissen, J. H. C., Diemer, M., Flexas, J., Garnier, E., Groom, P. K., Gulias, J., Hikosaka, K., Lamont, B. B., Lee, T., Lee, W., Lusk, C., Midgley, J. J., Navas, M.-L., Niinemets, Ü., Oleksyn, J., Osada, N., Poorter, H., Poot, P., Prior, L., Pyankov, V. I., Roumet, C., Thomas, S. C., Tjoelker, M. G., Veneklaas, E. J., & Villar, R. (2004). The worldwide leaf economics spectrum. *Nature*, 428(6985), 821-827. https://doi.org/10.1038/nature02403.

Zanella, A., Jabiol, B., Ponge, J. F., Sartori, G., De Waal, R., Van Delft, B., Graefe, U., Cools, N., Katzensteiner, K., Hager, H., & Englisch, M. (2011). A European morpho-functional classification of humus forms. *Geoderma*, 164(3-4), 138-145. https://doi.org/10.1016/j.geoderma.2011.05.016.

Zanella, A., Ponge, J. F., Jabiol, B., Sartori, G., Kolb, E., Le Bayon, R.-C., Gobat, J. M., Aubert, M., De Waal, R., Van Delft, B., Vacca, A., Serra, G., Chersich, S., Andreetta, A., Kõlli, R., Brun, J. J., Cools, N., English, M., Hager, H., Katzensteiner, K., Brêthes, A., De Nicola, C., Testi, A., Bernier, N., Graefe, U., Wolf, U., Juilleret, J., Garlato, A., Obber, S., Galvan, P., Zampedri, R., Frizzera, L., Tomasi, M., Banas, D., Bureau, F., Tatti, D., Salmon, S., Menardi, R., Fontanella, F., Carraro, V., Pizzeghello, D., Concheri, G., Squartini, A., Cattaneo, D., Scattolin, L., Nardi, S., Nicolini, G., & Viola, F. (2018). Terrestrial humus systems and forms - Keys of classification of humus systems and forms. *Applied Soil Ecology*, 122(Part 1), 75-86. https://doi.org/10.1016/j.apsoil.2017.06.012.

Appendix

Figure A1

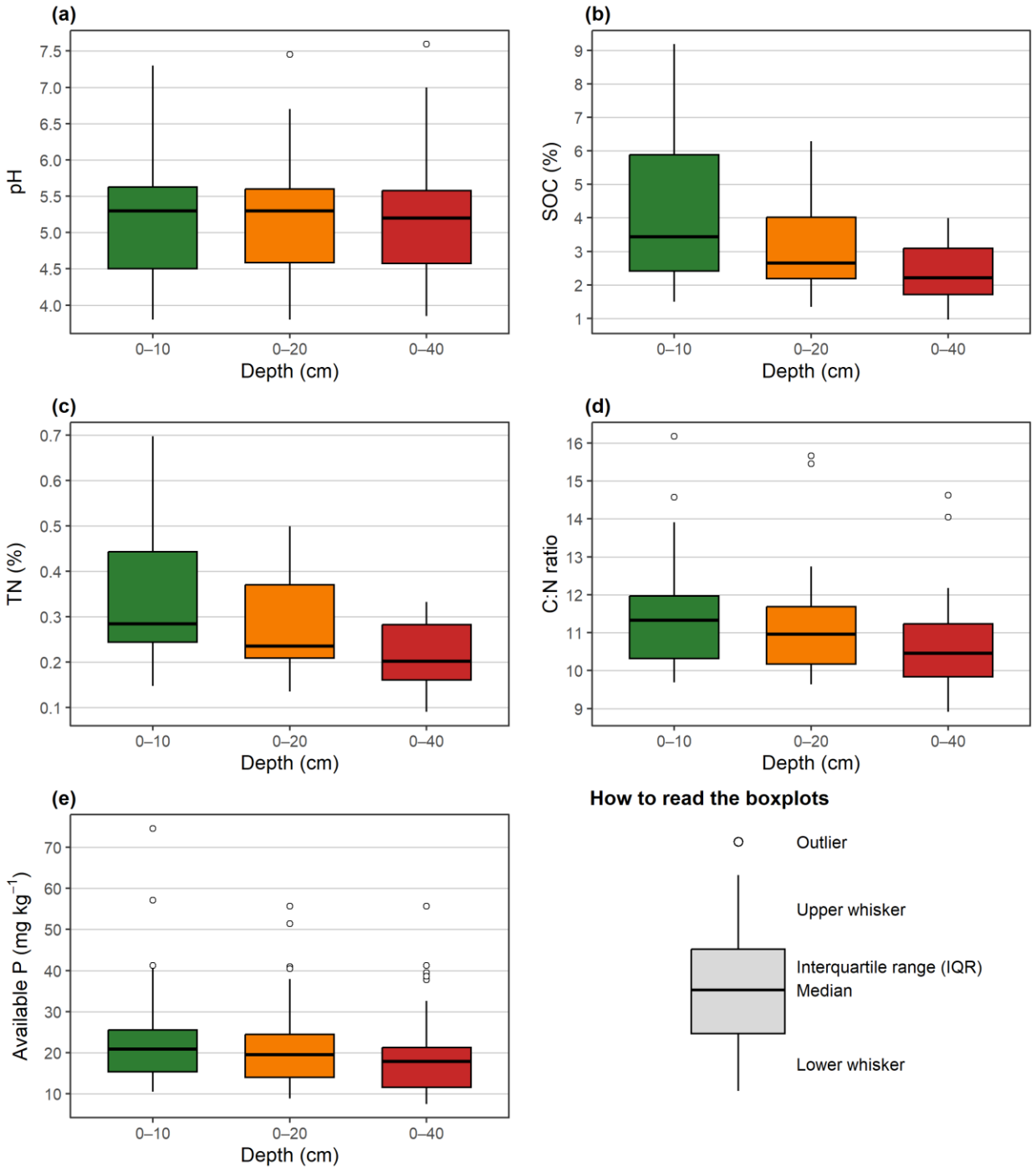

Figure A1. Soil property distributions across three depth intervals (0-10, 0-20, and 0-40 cm) in Milan urban forests (n = 44 plots). Boxplots show: (a) soil pH, (b) SOC (%), (c) TN (%), (d) C:N ratio, and (e) available P (mg kg^{-1}). Boxes represent interquartile range (IQR), horizontal lines indicate medians, whiskers extend to 1.5×IQR, and points show outliers. The schematic panel illustrates how boxplots should be interpreted.

Tables A1-A7

Table A1. Spearman rank correlation matrix - Soil variables by depth. 37 variables: Soil properties at three depths (0-10, 0-20, 0-40 cm: pH, SOC, TN, CN, avP, Sand, Silt, Clay), CWM functional traits (LDMC, SLA, LMA, LNC, LCC), CSR strategy components (C, S, R), and other variables (Age, Tree_cover, Bush_cover, Exotic_cover, Herbaceous_biomass).

	Soil 0-10cm								Soil 0-20cm								Soil 0-40cm								CWM Traits					CSR			Other				
	pH_010	SOC_010	Ntot_010	C:N_010	Pass_010	Sand_010	Silt_010	Clay_010	pH_020	SOC_020	Ntot_020	C:N_020	Pass_020	Sand_020	Silt_020	Clay_020	pH_040	SOC_040	Ntot_040	C:N_040	Pass_040	Sand_040	Silt_040	Clay_040	CWM_LDMC	CWM_SLA	CWM_LMA	CWM_LNC	CWM_LCC	CWM_C	CWM_S	CWM_R	Age	Tree_cover	Bush_cover	Exotic_cover	Herbaceous_biomass
pH_010	1.000	-0.587***	-0.602***	-0.190	0.318*	-0.409**	0.392**	-0.147	0.569***	-0.192	-0.159	-0.171	0.436**	-0.147	0.246	-0.381*	**0.923*** **	-0.626***	-0.649***	-0.338*	0.428**	-0.384*	0.390**	-0.151	-0.189	0.079	0.038	-0.196	-0.346*	0.506***	-0.370*	-0.080	-0.650***	-0.344*	0.117	-0.261	-0.384**
SOC_010	-0.587***	1.000	**0.961*** **	0.640***	-0.304*	0.552***	-0.543***	-0.073	-0.116	0.622***	0.374*	0.667***	-0.406**	0.296	-0.397**	0.163	-0.600***	**0.847*** **	**0.708*** **	**0.773*** **	-0.346*	0.542***	-0.529***	-0.125	0.095	-0.080	-0.046	0.464**	0.360*	-0.392**	0.298*	0.085	**0.772*** **	**0.615*** **	-0.018	0.328*	0.419**
Ntot_010	-0.602***	**0.961*** **	1.000	0.454**	-0.380*	0.497***	-0.492***	-0.023	-0.141	0.624***	0.474**	0.495***	-0.467**	0.268	-0.356*	0.181	-0.611***	**0.891*** **	**0.809*** **	0.663***	-0.391**	0.493***	-0.466**	-0.100	0.165	-0.173	0.044	0.449**	0.389**	-0.350*	0.376*	0.008	**0.765*** **	0.600***	-0.046	0.339*	0.353*
CN_010	-0.190	0.640***	0.454**	1.000	-0.004	0.300*	-0.270	-0.260	0.111	0.281	-0.145	**0.894*** **	-0.111	0.057	-0.134	-0.033	-0.268	0.320*	0.059	**0.738*** **	-0.092	0.305*	-0.301*	-0.231	-0.221	0.206	-0.223	0.331*	-0.015	-0.296	-0.080	0.228	0.399**	0.381*	0.160	0.083	0.334*
Pass_010	0.318*	-0.304*	-0.380*	-0.004	1.000	-0.207	0.261	-0.238	0.088	-0.026	-0.080	0.097	**0.958*** **	-0.093	0.181	-0.386**	0.354*	-0.322*	-0.361*	-0.020	**0.932*** **	-0.255	0.288	-0.146	-0.455**	0.373*	-0.296	-0.380*	-0.548***	0.122	-0.525***	0.286	-0.335*	-0.205	0.261	-0.359*	-0.457**
Sand_010	-0.409**	0.552***	0.497***	0.300*	-0.207	1.000	**0.973*** **	-0.083	-0.049	0.334*	0.165	0.277	-0.226	**0.846*** **	**0.887*** **	0.018	-0.407**	0.588***	0.538***	0.423**	-0.195	**0.988*** **	**0.958*** **	-0.224	0.202	-0.229	0.145	0.303*	0.389**	-0.290	0.314*	-0.062	0.550***	0.252	-0.080	0.255	0.593***
Silt_010	0.392**	-0.543***	-0.492***	-0.270	0.261	**0.973*** **	1.000	-0.094	0.019	-0.318*	-0.161	-0.273	0.272	**-0.810*** **	**0.900*** **	-0.170	0.382*	-0.582***	-0.525***	-0.434**	0.242	**0.974*** **	**0.984*** **	0.075	-0.274	0.326*	-0.230	-0.309*	-0.438**	0.210	-0.375*	0.151	-0.538***	-0.302*	0.151	-0.283	**-0.600*** **
Clay_010	-0.147	-0.073	-0.023	-0.260	-0.238	-0.083	-0.094	1.000	-0.124	-0.088	0.047	-0.149	-0.213	-0.108	-0.067	**0.825*** **	-0.113	0.001	0.039	-0.044	-0.217	-0.066	-0.094	**0.843*** **	0.206	-0.248	0.177	-0.107	0.248	0.080	0.276	-0.190	0.020	0.099	-0.239	-0.001	-0.073
pH_020	0.569***	-0.116	-0.141	0.111	0.088	-0.049	0.019	-0.124	1.000	-0.390**	-0.487***	0.042	0.066	-0.210	0.172	-0.014	0.581***	-0.175	-0.230	0.068	0.173	-0.017	0.054	-0.231	-0.139	0.135	-0.092	0.096	0.036	0.166	-0.042	0.017	-0.241	-0.065	0.272	-0.116	-0.217
SOC_020	-0.192	0.622***	0.624***	0.281	-0.026	0.334*	-0.318*	-0.088	-0.390**	1.000	**0.870*** **	0.492***	0.002	0.471**	-0.432**	-0.231	-0.202	**0.631*** **	0.520***	0.503***	0.010	0.329*	-0.292	-0.155	0.067	-0.171	0.100	0.112	0.126	-0.035	0.063	-0.028	0.352*	0.376*	-0.182	0.278	0.141
Ntot_020	-0.159	0.374*	0.474**	-0.145	-0.080	0.165	-0.161	0.047	-0.487***	**0.870*** **	1.000	0.089	-0.003	0.419**	-0.343*	-0.198	-0.139	0.522***	0.549***	0.163	-0.016	0.161	-0.120	-0.020	0.177	-0.279	0.212	-0.019	0.136	0.094	0.122	-0.166	0.197	0.215	-0.185	0.257	-0.009
CN_020	-0.171	0.667***	0.495***	**0.894*** **	0.097	0.277	-0.273	-0.149	0.042	0.492***	0.089	1.000	0.001	0.107	-0.174	-0.053	-0.186	0.406**	0.122	**0.877*** **	0.019	0.277	-0.280	-0.175	-0.160	0.179	-0.214	0.248	0.022	-0.195	-0.057	0.140	0.397**	0.384**	0.083	0.121	0.238
Pass_020	0.436**	-0.406**	-0.467**	-0.111	**0.958*** **	-0.226	0.272	-0.213	0.066	0.002	-0.003	0.001	1.000	-0.022	0.131	-0.435**	0.458**	-0.378*	-0.406**	-0.102	**0.948*** **	-0.268	0.299*	-0.128	-0.386**	0.283	-0.200	-0.451**	-0.555***	0.185	-0.486***	0.215	-0.438**	-0.267	0.232	-0.375*	-0.453**
Sand_020	-0.147	0.296	0.268	0.057	-0.093	**0.846*** **	**-0.810*** **	-0.108	-0.210	0.471**	0.419**	0.107	-0.022	1.000	**-0.955*** **	-0.204	-0.141	0.372*	0.374*	0.162	-0.059	**0.839*** **	**0.804*** **	-0.247	0.228	-0.311*	0.261	0.100	0.241	-0.081	0.207	-0.198	0.345*	0.042	-0.142	0.239	0.473**
Silt_020	0.246	-0.397**	-0.356*	-0.134	0.181	**0.887*** **	**0.900*** **	-0.067	0.172	-0.432**	-0.343*	-0.174	0.131	**-0.955*** **	1.000	-0.029	0.224	-0.439**	-0.416**	-0.265	0.163	**0.886*** **	**0.906*** **	0.075	-0.258	0.350*	-0.271	-0.180	-0.312*	0.111	-0.275	0.213	-0.439**	-0.175	0.193	-0.318*	-0.538***
Clay_020	-0.381*	0.163	0.181	-0.033	-0.386**	0.018	-0.170	**0.825*** **	-0.014	-0.231	-0.198	-0.053	-0.435**	-0.204	-0.029	1.000	-0.381*	0.169	0.186	0.114	-0.424**	0.023	-0.185	**0.791*** **	0.187	-0.146	0.042	0.159	0.334*	-0.177	0.352*	-0.015	0.263	0.233	-0.161	0.056	0.128
pH_040	**0.923*** **	-0.600***	-0.611***	-0.268	0.354*	-0.407**	0.382*	-0.113	0.581***	-0.202	-0.139	-0.186	0.458**	-0.141	0.224	-0.381*	1.000	-0.629***	-0.628***	-0.326*	0.430**	-0.387**	0.387**	-0.147	-0.161	0.101	0.005	-0.282	-0.262	0.498***	-0.348*	-0.090	-0.662***	-0.379*	0.079	-0.183	-0.435**
SOC_040	-0.626***	**0.847*** **	**0.891*** **	0.320*	-0.322*	0.588***	-0.582***	0.001	-0.175	**0.631*** **	0.522***	0.406**	-0.378*	0.372*	-0.439**	0.169	-0.629***	1.000	**0.941*** **	0.668***	-0.277	0.584***	-0.535***	-0.125	0.156	-0.184	0.060	0.375*	0.395**	-0.321*	0.391**	0.019	0.608***	0.477**	-0.053	0.337*	0.349*
Ntot_040	-0.649***	**0.708*** **	**0.809*** **	0.059	-0.361*	0.538***	-0.525***	0.039	-0.230	0.520***	0.549***	0.122	-0.406**	0.374*	-0.416**	0.186	-0.628***	**0.941*** **	1.000	0.410**	-0.312*	0.530***	-0.472**	-0.083	0.185	-0.220	0.108	0.323*	0.407**	-0.275	0.416**	-0.024	0.542***	0.318*	-0.081	0.355*	0.277
CN_040	-0.338*	**0.773*** **	0.663***	**0.738*** **	-0.020	0.423**	-0.434**	-0.044	0.068	0.503***	0.163	**0.877*** **	-0.102	0.162	-0.265	0.114	-0.326*	0.668***	0.410**	1.000	-0.035	0.409**	-0.413**	-0.101	-0.051	0.077	-0.152	0.303*	0.186	-0.299*	0.093	0.163	0.477**	0.508***	0.069	0.173	0.280
Pass_040	0.428**	-0.346*	-0.391**	-0.092	**0.932*** **	-0.195	0.242	-0.217	0.173	0.010	-0.016	0.019	**0.948*** **	-0.059	0.163	-0.424**	0.430**	-0.277	-0.312*	-0.035	1.000	-0.234	0.293	-0.175	-0.420**	0.323*	-0.252	-0.427**	-0.481***	0.171	-0.467**	0.247	-0.415**	-0.196	0.303*	-0.350*	-0.504***
Sand_040	-0.384*	0.542***	0.493***	0.305*	-0.255	**0.988*** **	**0.974*** **	-0.066	-0.017	0.329*	0.161	0.277	-0.268	**0.839*** **	**0.886*** **	0.023	-0.387**	0.584***	0.530***	0.409**	-0.234	1.000	**0.964*** **	-0.249	0.247	-0.276	0.197	0.297	0.410**	-0.250	0.349*	-0.118	0.533***	0.256	-0.114	0.280	**0.610*** **
Silt_040	0.390**	-0.529***	-0.466**	-0.301*	0.288	**0.958*** **	**0.984*** **	-0.094	0.054	-0.292	-0.120	-0.280	0.299*	**0.804*** **	**0.906*** **	-0.185	0.387**	-0.535***	-0.472**	-0.413**	0.293	**0.964*** **	1.000	0.046	-0.260	0.290	-0.198	-0.344*	-0.410**	0.255	-0.360*	0.124	-0.543***	-0.292	0.169	-0.296	**-0.658*** **
Clay_040	-0.151	-0.125	-0.100	-0.231	-0.146	-0.224	0.075	**0.843*** **	-0.231	-0.155	-0.020	-0.175	-0.128	-0.247	0.075	**0.791*** **	-0.147	-0.125	-0.083	-0.101	-0.175	-0.249	0.046	1.000	0.108	-0.093	0.027	-0.051	0.113	-0.014	0.149	-0.043	0.000	0.094	-0.222	-0.068	-0.070
CWM_LDMC	-0.189	0.095	0.165	-0.221	-0.455**	0.202	-0.274	0.206	-0.139	0.067	0.177	-0.160	-0.386**	0.228	-0.258	0.187	-0.161	0.156	0.185	-0.051	-0.420**	0.247	-0.260	0.108	1.000	**-0.775*** **	0.669***	-0.222	0.624***	0.019	**0.756*** **	-0.576***	0.272	0.095	-0.130	0.052	0.401**
CWM_SLA	0.079	-0.080	-0.173	0.206	0.373*	-0.229	0.326*	-0.248	0.135	-0.171	-0.279	0.179	0.283	-0.311*	0.350*	-0.146	0.101	-0.184	-0.220	0.077	0.323*	-0.276	0.290	-0.093	**-0.775*** **	1.000	**0.947*** **	0.172	-0.336*	-0.331*	-0.522***	0.690***	-0.165	-0.198	0.296	-0.087	-0.311*
CWM_LMA	0.038	-0.046	0.044	-0.223	-0.296	0.145	-0.230	0.177	-0.092	0.100	0.212	-0.214	-0.200	0.261	-0.271	0.042	0.005	0.060	0.108	-0.152	-0.252	0.197	-0.198	0.027	**0.669*** **	**0.947*** **	1.000	-0.211	0.131	0.467**	0.387**	**0.732*** **	0.069	0.040	-0.294	0.021	0.208
CWM_LNC	-0.196	0.464**	0.449**	0.331*	-0.380*	0.303*	-0.309*	-0.107	0.096	0.112	-0.019	0.248	-0.451**	0.100	-0.180	0.159	-0.282	0.375*	0.323*	0.303*	-0.427**	0.297	-0.344*	-0.051	-0.222	0.172	-0.211	1.000	0.048	-0.133	-0.019	0.126	0.384*	0.289	0.093	0.273	0.325*
CWM_LCC	-0.346*	0.360*	0.389**	-0.015	-0.548***	0.389**	-0.438**	0.248	0.036	0.126	0.136	0.022	-0.555***	0.241	-0.312*	0.334*	-0.262	0.395**	0.407**	0.186	-0.481***	0.410**	-0.410**	0.113	0.624***	-0.336*	0.131	0.048	1.000	-0.321*	0.634***	-0.051	0.325*	0.199	-0.150	0.274	0.407**
CWM_C	0.506***	-0.392**	-0.350*	-0.296	0.122	-0.290	0.210	0.080	0.166	-0.035	0.094	-0.195	0.185	-0.081	0.111	-0.177	0.498***	-0.321*	-0.275	-0.299*	0.171	-0.250	0.255	-0.014	0.019	-0.331*	0.467**	-0.133	-0.321*	1.000	-0.354*	-0.580***	-0.307*	-0.086	-0.250	0.014	-0.444**
CWM_S	-0.370*	0.298*	0.376*	-0.080	-0.525***	0.314*	-0.375*	0.276	-0.042	0.063	0.122	-0.057	-0.486***	0.207	-0.275	0.352*	-0.348*	0.391**	0.416**	0.093	-0.467**	0.349*	-0.360*	0.149	**0.756*** **	-0.522***	0.387**	-0.019	0.634***	-0.354*	1.000	-0.423**	0.362*	0.130	-0.003	0.078	0.489***
CWM_R	-0.080	0.085	0.008	0.228	0.286	-0.062	0.151	-0.190	0.017	-0.028	-0.166	0.140	0.215	-0.198	0.213	-0.015	-0.090	0.019	-0.024	0.163	0.247	-0.118	0.124	-0.043	-0.576***	0.690***	**0.732*** **	0.126	-0.051	-0.580***	-0.423**	1.000	-0.065	-0.030	0.211	-0.125	-0.058
Age	-0.650***	**0.772*** **	**0.765*** **	0.399**	-0.335*	0.550***	-0.538***	0.020	-0.241	0.352*	0.197	0.397**	-0.438**	0.345*	-0.439**	0.263	-0.662***	0.608***	0.542***	0.477**	-0.415**	0.533***	-0.543***	0.000	0.272	-0.165	0.069	0.384*	0.325*	-0.307*	0.362*	-0.065	1.000	0.473**	0.023	0.219	0.391**
Tree_cover	-0.344*	0.615***	0.600***	0.381*	-0.205	0.252	-0.302*	0.099	-0.065	0.376*	0.215	0.384**	-0.267	0.042	-0.175	0.233	-0.379*	0.477**	0.318*	0.508***	-0.196	0.256	-0.292	0.094	0.095	-0.198	0.040	0.289	0.199	-0.086	0.130	-0.030	0.473**	1.000	-0.108	0.206	0.101
Bush_cover	0.117	-0.018	-0.046	0.160	0.261	-0.080	0.151	-0.239	0.272	-0.182	-0.185	0.083	0.232	-0.142	0.193	-0.161	0.079	-0.053	-0.081	0.069	0.303*	-0.114	0.169	-0.222	-0.130	0.296	-0.294	0.093	-0.150	-0.250	-0.003	0.211	0.023	-0.108	1.000	-0.202	-0.212
Exotic_cover	-0.261	0.328*	0.339*	0.083	-0.359*	0.255	-0.283	-0.001	-0.116	0.278	0.257	0.121	-0.375*	0.239	-0.318*	0.056	-0.183	0.337*	0.355*	0.173	-0.350*	0.280	-0.296	-0.068	0.052	-0.087	0.021	0.273	0.274	0.014	0.078	-0.125	0.219	0.206	-0.202	1.000	0.202
Herbaceous_biomass	-0.384**	0.419**	0.353*	0.334*	-0.457**	0.593***	**-0.600*** **	-0.073	-0.217	0.141	-0.009	0.238	-0.453**	0.473**	-0.538***	0.128	-0.435**	0.349*	0.277	0.280	-0.504***	**0.610*** **	**-0.658*** **	-0.070	0.401**	-0.311*	0.208	0.325*	0.407**	-0.444**	0.489***	-0.058	0.391**	0.101	-0.212	0.202	1.000

*Method: Spearman correlation (ρ) used for all pairs due to non-normality in 76% of variables. Significance: *** p < 0.001, ** p < 0.01, * p < 0.05; Color coding: Red (|ρ| > 0.9), Orange (|ρ| > 0.7), Yellow (|ρ| > 0.6).*

Table A2. Forest vs agriculture SOC comparison by Pedolandscape Unit (PU) and depth. Values are mean ± standard deviation. Significance from independent *t*-tests.

Depth (cm)	PU	Forest n	Forest Mean (%)	Forest SD	Agri n	Agri Mean (%)	Agri SD	Difference (%)	Relative Change (%)	*t*-statistic	Sig.
0-10	1	13	2.86	0.62	6	1.20	0.42	+1.66	138	5.92	***
0-10	2	3	1.88	0.40	6	1.79	0.24	+0.09	5	0.43	ns
0-10	3	19	6.00	2.49	6	1.02	0.14	+4.98	486	4.83	***
0-10	4	2	4.11	0.30	6	1.37	0.21	+2.74	200	14.49	***
0-10	5	3	2.98	1.24	6	1.14	0.31	+1.84	163	3.67	**
0-10	6	4	3.89	0.28	6	1.43	0.58	+2.46	172	7.75	***
0-20	1	13	2.35	0.33	6	1.10	0.27	+1.25	114	8.02	***
0-20	2	3	1.46	0.13	6	1.78	0.23	-0.32	-18	-2.19	ns
0-20	3	19	3.29	1.37	6	1.01	0.16	+2.28	225	4.00	***
0-20	4	2	3.73	0.09	6	1.37	0.21	+2.36	172	14.52	***
0-20	5	3	2.53	0.62	6	0.94	0.23	+1.58	168	5.85	***
0-20	6	4	3.01	0.31	6	1.32	0.26	+1.70	129	9.33	***
0-40	1	13	1.90	0.36	6	0.90	0.18	+1.00	112	6.41	***
0-40	2	3	1.04	0.10	6	1.43	0.26	-0.40	-28	-2.51	*
0-40	3	19	2.89	0.80	6	0.89	0.23	+2.00	225	5.94	***
0-40	4	2	3.23	0.02	6	1.27	0.18	+1.95	154	14.79	***
0-40	5	3	1.86	0.41	6	0.77	0.23	+1.08	141	5.23	**
0-40	6	4	2.22	0.27	6	1.18	0.12	+1.04	88	8.59	***

*** $p < 0.001$; ** $p < 0.01$; * $p < 0.05$; ns = not significant.

Table A3. Age effect on forest SOC with and without spatial control. Naïve models use simple linear regression (Age only). Spatially-controlled models include Moran's Eigenvector Maps (MEMs) as covariates. β = slope coefficient (% SOC per year).

Model	Depth (cm)	β (% per year)	R^2	*p*-value	Interpretation
Naïve (no spatial control)	0-10	0.0426	0.701	<0.001 ***	+0.43% per decade
Spatially controlled (MEMs)	0-10	0.0146	0.587	<0.001 ***	+0.15% per decade
Reduction (%)	0-10	-74%	-16%	-	Spatial confounding effect
Naïve	0-20	0.0091	0.140	0.025 *	+0.09% per decade
Spatially controlled	0-20	-0.0051	0.089	0.413	No effect after control
Naïve	0-40	0.0138	0.560	<0.001 ***	+0.14% per decade
Spatially controlled	0-40	0.0047	0.442	0.024 *	+0.05% per decade

*** $p < 0.001$; ** $p < 0.01$; * $p < 0.05$.

Table A4. Spatial autocorrelation (Moran's *I*) comparison between forest and agricultural soils. Tests conducted using Gabriel graph connectivity matrix with distance weighting.

Land Use	Depth (cm)	Moran's *I*	*z*-score	*p*-value	Significance
Forest	0-10	+0.901	+4.81	<0.001	***
Agriculture	0-10	+0.193	+1.86	0.063	ns
Forest	0-20	+0.214	+1.26	0.207	ns
Agriculture	0-20	+0.383	+3.41	0.001	***
Forest	0-40	+0.734	+3.92	<0.001	***
Agriculture	0-40	+0.221	+2.07	0.038	*

*** $p < 0.001$; ** $p < 0.01$; * $p < 0.05$; ns = not significant.

Table A5. Spatial proximity statistics between forest and agricultural sites. Distances calculated after coordinate transformation (EPSG:3003 → EPSG:32632). Proximity bias test: correlation between forest SOC and nearest agriculture SOC. Distance effect test: correlation between spatial separation and SOC difference.

Metric	Value
Mean distance (km)	4.53
Median distance (km)	2.80
Min distance (km)	0.62
Max distance (km)	10.19
Very close (<2 km) %	34.1
Close (2-5 km) %	29.5
Medium (5-10 km) %	27.3
Far (>10 km) %	9.1
Correlation: Forest SOC vs Nearby Agri SOC (*r*)	-0.046
p-value (proximity bias test)	0.766 (ns)
Correlation: Distance vs SOC Difference (*r*)	-0.301
p-value (distance effect test)	0.047 *

* $p < 0.05$; ns = not significant.

Table A6. Soil and vegetation properties by humus form. Values are mean ± SD. *H*-statistics and *p*-values from Kruskal-Wallis tests.

Property	Mull (n = 31)	Moder (n = 7)	Mor (n = 6)	*H*	*p*-value	Significance
pH	5.61 ± 0.58	4.54 ± 0.33	3.92 ± 0.12	26.4	<0.001	***
SOC (%)	3.03 ± 0.89	6.33 ± 1.53	8.52 ± 0.62	25.5	<0.001	***
TN (%)	0.27 ± 0.05	0.57 ± 0.13	0.68 ± 0.02	27.1	<0.001	***
C:N ratio	11.33 ± 1.57	11.09 ± 0.39	12.57 ± 0.71	7.5	0.024	*
avP (mg kg^{-1})	27.31 ± 13.17	14.77 ± 2.59	15.19 ± 3.16	17.5	<0.001	***
Forest age (years)	27.7 ± 11.2	96.3 ± 44.9	123.7 ± 40.8	27.9	<0.001	***
Tree cover (%)	65.2 ± 20.9	79.3 ± 13.1	85.5 ± 6.8	6.3	0.042	*
Herbaceous biomass (%)	12.7 ± 21.1	35.7 ± 27.8	39.3 ± 29.0	11.6	0.003	**
C-strategy (%)	36.3 ± 10.1	35.0 ± 23.5	19.6 ± 5.3	9.3	0.010	**
S-strategy (%)	17.6 ± 10.5	29.4 ± 14.2	36.9 ± 7.4	12.0	0.003	**
R-strategy (%)	46.0 ± 15.8	35.6 ± 16.9	43.5 ± 8.7	0.9	0.629	ns
LNC (%)	2.54 ± 0.65	3.44 ± 1.13	3.53 ± 1.15	8.2	0.016	*

*$p < 0.05$; **$p < 0.01$; ***$p < 0.001$; ns = not significant

Table A7. Fourth-corner correlations between humus forms and plant functional traits/strategies. Spearman's ρ and *p*-values reported; bold indicates FDR-corrected significance ($p < 0.05$).

Humus Variable	Trait	ρ	*p*-value	Significance
Humus_Mor	C-strategy	-0.43	0.003	**
Humus_Mor	S-strategy	+0.45	0.002	**
Humus_Mor	R-strategy	+0.05	0.737	ns
Humus_Moder	C-strategy	-0.09	0.559	ns
Humus_Moder	S-strategy	+0.19	0.221	ns
Humus_Moder	R-strategy	-0.14	0.350	ns
Humus_Mor	SLA	-0.06	0.686	ns
Humus_Moder	SLA	-0.25	0.106	ns
Humus_Mor	LDMC	+0.17	0.279	ns
Humus_Moder	LDMC	+0.21	0.176	ns
Humus_Mor	LNC	+0.28	0.069	marginal
Humus_Moder	LNC	+0.29	0.060	marginal

**$p < 0.01$ after FDR correction; ns = not significant

Chapter 2.
PyC distribution across the Metropolitan City of Milan

This chapter explores the distribution and stabilization of pyrogenic carbon across a heterogeneous mosaic of urban and peri-urban green areas at the city scale. Through the analysis of soil depth profiles and physical fractionation into POM and MAOM, it investigates how land-use history and ecosystem development influence PyC persistence. The chapter further examines spatial patterns within the urban matrix, providing insights into the role of combustion-derived carbon in urban soil functioning.

1. Introduction

Soils represent one of the largest terrestrial carbon reservoirs and play a central role in regulating biogeochemical cycles, ecosystem functioning and climate feedbacks. In urban and peri-urban environments, soil organic carbon (SOC) dynamics are profoundly affected by anthropogenic pressures, including land-use change, atmospheric deposition of pollutants, soil sealing and vegetation management, resulting in highly heterogeneous and functionally altered soil systems (Canedoli *et al.*, 2020).

Among SOC fractions, pyrogenic carbon (PyC) has emerged as a key component of soil carbon pools. PyC is formed during incomplete combustion of biomass and fossil fuels and spans a wide continuum of materials from partially charred residues to highly condensed soot particles (Bird *et al.*, 2015; Masiello, 2004). For a long time considered highly inert and environmentally persistent, PyC is now recognized as a heterogeneous pool, subject to redistribution and interaction with mineral and biological components of soils (Bird *et al.*, 2015).

Urban ecosystems represent hotspots for PyC accumulation due to continuous inputs from vehicular traffic, domestic heating systems, industrial activities and waste combustion. These combustion-derived inputs are often spatially concentrated and temporally persistent, especially in large metropolitan areas (Hofman *et al.*, 2018).

A critical mechanism controlling the persistence and environmental behaviour of both SOC and PyC is their association with distinct soil physical fractions. The physical separation of soil organic matter into particulate organic matter (POM) and mineral-associated organic matter (MAOM) provides a functional framework to distinguish between relatively labile and physically protected pools. POM is generally characterized by weak organo-mineral interactions and faster turnover, whereas MAOM is stabilized through strong sorption onto mineral surfaces and microaggregation.

Emerging evidence suggests that PyC is not uniformly distributed across these fractions. While traditionally regarded as a highly stable material, part of PyC can be retained in coarse, labile pools, particularly in environments subject to recent combustion inputs. Conversely, long-term stabilization appears to be linked to mineral association, suggesting that MAOM may represent an important sink for persistent PyC (Bird *et al.*, 2015).

Vertical gradients add another level of complexity. Both SOC and PyC typically decrease with soil depth, reflecting declining organic inputs and biological activity. Several studies have demonstrated that pyrogenic carbon represents a non-negligible fraction of total soil organic carbon, although its relative contribution varies widely depending on land use, depth, and environmental context, ranging from a few percent in background soils to more than one-third of total organic carbon in urban environments (Nam *et al.*, 2008; Edmondson *et al.*, 2015; Lutfalla *et al.*, 2017). Understanding how PyC and SOC are distributed across soil depth and physical fractions is essential for predicting carbon persistence in urban soils (Masiello, 2004).

In this context, understanding the distribution of PyC at the city scale is particularly relevant for interpreting urban soil functioning. PyC contributes to long-term carbon storage, influences the stabilization of organic matter, and may interact with co-occurring contaminants. Moreover, spatial patterns of PyC reflect land-use

legacy, atmospheric deposition, and ecosystem development, making city-scale assessments essential for linking biogeochemical processes to urban biodiversity and management strategies.

However, despite growing interest in PyC, most existing studies have focused either on its climatic relevance or on its role in natural and agricultural systems. Comparatively little attention has been given to urban and peri-urban soils, and even fewer studies have simultaneously addressed PyC, its physical partitioning into POM and MAOM, and its vertical distribution across multiple soil depths in an integrated framework (Bird *et al.*, 2015).

The Metropolitan City of Milan (Northern Italy) represents a highly suitable model system to investigate urban and peri-urban PyC distribution and stabilization. As the second largest metropolitan area in Italy and a medium-sized city in a global context, Milan is characterized by a long industrial history, intense vehicular traffic and domestic heating emissions. These long-term atmospheric pressures, combined with heterogeneous land-use trajectories, have generated a complex mosaic of urban, peri-urban and remnant semi-natural ecosystems, including forests, grasslands and intensively managed green spaces, within a relatively constrained geographic area. Previous research has highlighted the ecological relevance of urban soils in this region and their surprisingly high SOC stocks, especially within urban parks (Canedoli *et al.*, 2020).

The objectives of this study were to: (i) characterize depth-dependent patterns of SOC and PyC across urban and peri-urban soils (0-10, 10-20, 20-40 cm); (ii) assess the physical partitioning of PyC between POM and MAOM as an indicator of stabilization pathways; (iii) evaluate differences in PyC concentration and partitioning across green area categories, including age-stratified peri-urban forests; and (iv) test the influence of spatial position within the urban matrix (concentric zones) on PyC-related properties.

This integrated framework aims to improve our understanding of how combustion-derived carbon is distributed and stabilized within urban and peri-urban soils, and how land-use history, ecosystem development and soil depth jointly shape PyC persistence.

2. Materials and Methods

2.1 Study Area and Site Classification

The study was carried out in the Metropolitan City of Milan (Northern Italy), one of the most densely urbanized areas in Europe. The territory extends over approximately 1,600 km² and includes the city of Milan and 133 municipalities, characterized by intensive urbanization, high population density (2,063 inhabitants/km^2), and a complex mosaic of built-up areas (41%), agricultural lands (50%), and green infrastructures (8%).

The Metropolitan City of Milan is located in the central-western sector of the Po Valley alluvial plain, with predominantly flat topography (mean elevation ~100 m a.s.l.) and a continental climate. Mean annual precipitation is approximately 920-940 mm, and mean minimum and maximum daily temperatures are 8 °C and 17 °C, respectively. Natural soils are mainly *Fluvisols*, *Cambisols* and *Luvisols* developed on alluvial deposits, with localized *Gleysols* and *Umbrisols* according to the World Reference Base for Soil Resources (IUSS Working Group WRB, 2022). In intensely urbanized sectors, natural soil patterns are frequently replaced or deeply modified by *Technosols* due to prolonged anthropogenic disturbances and the incorporation of technogenic materials.

A total of 134 georeferenced soil sampling sites were included in the study, spanning wide gradients of urbanization intensity, land-use history and vegetation structure across the Metropolitan City of Milan (Figure 2.1; Appendix Tables A1-A2).

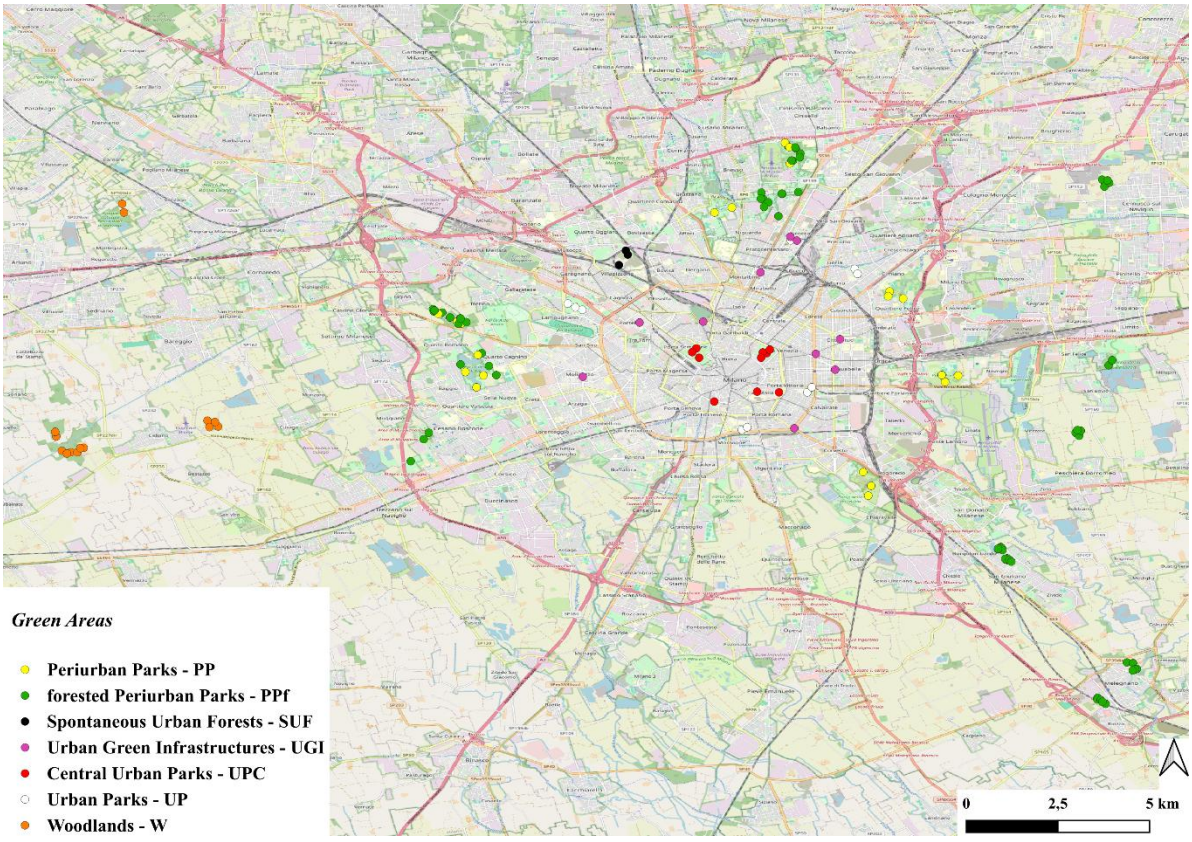

Figure 2.1. Spatial distribution of the 134 soil sampling sites across the Metropolitan City of Milan (Northern Italy), classified according to green area typology. Site characteristics are reported in Appendix Tables A1-A2.

The dataset integrates two complementary sampling campaigns conducted with comparable field and laboratory protocols but originally designed to address different research questions: 74 sites were collected within the framework of the present PhD project, while 60 sites derive from the doctoral work of De Feudis (2026). Although the two datasets share common sampling depths and analytical procedures, they were conceived independently and later harmonized for the purposes of the present analysis. Site age information was available only for forested systems and is therefore reported exclusively for forested sites (Appendix Table A1).

Sampling sites were classified into seven green area categories reflecting increasing levels of anthropogenic pressure and decreasing structural complexity. Peri-urban parks (PP; n = 21) include grass-dominated and recreational green areas lacking a developed forest canopy. Forested peri-urban parks (PPf; n = 66) comprise afforested systems established on former agricultural land; within this category, forest stands were further stratified by age into young (PPfy, 10-20 years), mid-aged (PPfm, 21-40 years) and older stands (PPfo, 41-60 years), and these age classes were treated as categorical levels in graphical and statistical analyses. Urban parks (UP; n = 10) are public green areas embedded within the urban matrix but located outside the historical city centre, whereas central urban parks (UPC; n = 10) correspond to green spaces located within the historical core of Milan.

Highly fragmented and intensively managed green spaces, such as traffic islands and small pocket gardens, were grouped under the category Urban Green Infrastructure (UGI; n = 10). Spontaneously established forest patches embedded within the dense urban fabric and developed on former industrial land were classified as Spontaneous Urban Forests (SUF; n = 3), represented in this study by the La Goccia area (Appendix Table A1). Finally, ancient peri-urban woodlands (W; n = 14) include long-established forest remnants, often older than 150 years, representing relics of the original lowland forests.

For clarity, all category abbreviations (PP, PPf, UP, UPC, UGI, SUF, W) are consistently used across figures and statistical analyses.

This classification was used as a categorical explanatory variable in all subsequent analyses.

2.2 Soil Sampling and Laboratory Analyses

Soil sampling was conducted between 2023 and 2024 using a gouge auger (Eijkelkamp, 2.5 cm diameter). Mineral soil samples were collected from three depth intervals (0-10 cm, 10-20 cm, 20-40 cm) at each georeferenced site.

In the sampling campaign conducted within this PhD project, a 10 × 10 m plot was established at each site, and three subsampling points were located following a triangular scheme at approximately 2 m from the plot centre. Subsamples were composited by depth layer to obtain one representative sample per site and depth.

In the complementary dataset derived from De Feudis (2026), soil sampling was performed within smaller plots (4 × 4 m), and composite samples were obtained by pooling five subsampling points per plot (one at the centre and four placed along the plot axes at 2 m from the centre), again composited by depth layer.

Despite differences in plot size and number of subsamples, both datasets share the same sampling depths and consistent compositing and analytical procedures. Accordingly, in all subsequent analyses the statistical unit is the site-level composite sample for each depth layer.

Mineral soil samples were air-dried for one week. Aggregates were manually broken with rubber tools, and coarse fragments (e.g., stones, bricks, roots) were removed. The fine earth fraction (< 2 mm) was used for analyses. Sub-samples milled < 0.2 mm were prepared for SOC, total N, and PyC analyses.

Analytical procedures included pH in H_2O (1:2.5 soil-to-solution ratio; potentiometric method), total carbonates ($CaCO_3$, Dietrich-Frühling calcimeter; ISO 10693), SOC and total N (dry combustion; Flash EA 1112 NCSoil elemental analyzer, Thermo Fisher Scientific, Pittsburgh, PA, USA), available phosphorus (avP) (ascorbic acid method; Olsen & Dean, 1965), and texture (pipette method, after sodium hexametaphosphate dispersion; Day, 1965).

2.2.1 PyC Quantification Method

PyC was quantified on all soil samples using the Chemo-Thermal Oxidation method (CTO); we employ a modified version of the CTO protocol - originally introduced by Gustafsson *et al.* (1997) and refined in Gustafsson *et al.* (2001) - lowering the oxidation temperature from 375 °C to 360 °C to improve selectivity toward the most thermally stable PyC fraction, consistent with evidence from Elmquist *et al.* (2004) regarding thermal thresholds for soot preservation.

The CTO-360 protocol was selected to specifically target the most thermally and chemically stable fraction of PyC, thus focusing on the long-term persistent pool most relevant for urban soil carbon stabilization and potential contaminant interactions.

Prior to analysis, carbonates were removed by acid pre-treatment with 1 M HCl. Sub-samples (<0.2 mm) were oven-dried, weighed and oxidized in a muffle furnace at 360 °C for 18 hours under a 20% O_2/air mixture. The remaining residue was analysed for carbon content by elemental analyzer.

2.2.2 Physical Fractionation of SOC and PyC

Physical fractionation was performed on samples from the 0-10 cm and 10-20 cm layers, which encompass the biologically most active and management-sensitive portion of the mineral soil profile and capture the depth interval where recent inputs and stabilization processes are expected to vary most strongly.

Samples (<2 mm) were dispersed with sodium hexametaphosphate (0.5%), sieved at 53 µm, and separated into POM and MAOM fractions (Cotrufo *et al.*, 2019). Both fractions were oven-dried (60 °C) and analysed for SOC and PyC (CTO-360; Section 2.2.1).

Following fractionation, SOC associated with the particulate and mineral-associated fractions was defined as SOC_POM and SOC_MAOM, respectively, while PyC in these fractions was defined as PyC_POM and PyC_MAOM.

2.3 Data Preparation and Statistical Analyses

All statistical analyses were performed using R version 4.4.3 (R Core Team, 2025).

Soil variables were organized in a long-format dataset, with sampling site as the experimental unit and soil depth layers (0-10, 10-20, 20-40 cm) treated as repeated observations within each site.

Green areas were classified according to green area category and, for forested periurban parks (PPf), further stratified into age classes (PPfy, PPfm, PPfo).

PyC concentrations were derived from the CTO-360 method. Where required, relative indices were calculated, including:

- the PyC:SOC ratio, expressing the proportional contribution of pyrogenic carbon to total soil organic carbon;
- the PyC_POM:PyC_MAOM ratio, describing the relative dominance of particulate versus mineral-associated PyC pools.

Physical fractionation data were available only for the upper two soil layers (0-10 and 10-20 cm) and were analysed accordingly.

The main analytical approach was based on linear mixed-effects models (LMMs), explicitly accounting for the hierarchical structure of the dataset, with multiple soil layers nested within sampling sites.

Models followed the general structure:

$$y \sim \textit{fixed effects} + (1 \mid \textit{site})$$

where *y* represents the response variable, *fixed effects* included soil depth, green area category (and age class where applicable), and *site* was included as a random intercept.

LMMs were fitted using the *lmer* function from the *lmerTest* package.

Model assumptions (normality of residuals and homogeneity of variance) were evaluated visually using diagnostic plots. When assumptions were violated, appropriate transformations of the response variable (logarithmic, square root, Box-Cox, or Yeo-Johnson) were applied.

If transformed LMMs still failed to meet assumptions, generalized linear mixed models (GLMMs) were used, selecting an appropriate error distribution: Gamma distribution with *log link* for strictly positive, right-skewed continuous variables.

GLMMs were fitted using the *lme4* framework.

For all parametric models (LMM and GLMM), estimated marginal means (EMMs) were calculated using the *emmeans* package.

For GLMMs, EMMs were regridded to the response scale prior to interpretation.

Pairwise comparisons among factor levels were performed using:

- Tukey-adjusted tests for single-factor comparisons;
- Sidak-adjusted tests when multiple fixed factors were included, with stratification specified using the by argument.

Results of post-hoc comparisons were summarized using compact letter displays (CLD) generated with the *cld* function from the *multcomp* package.

When neither LMM nor GLMM approaches were appropriate, non-parametric analyses were conducted as a complementary approach.

Global differences among groups were tested using Kruskal-Wallis tests, followed by pairwise Wilcoxon rank-sum tests.

To control for multiple comparisons, Benjamini-Hochberg false discovery rate (FDR) correction was applied.

Significance groupings from non-parametric tests were derived using the *multcompView* package.

Analyses were structured to reflect the organization of the Results section:

- Depth effects were tested across the full soil profile (0-10, 10-20, 20-40 cm) using mixed-effects models.
- Green area category effects were evaluated separately within each depth layer where appropriate.
- For physical fractionation data, analyses were restricted to the 0-10 and 10-20 cm layers.
- The influence of urban concentric zones (inner, intermediate, outer) was tested using mixed-effects models including green area age as a covariate.

Throughout the analyses, statistical significance was assessed at $\alpha = 0.05$.

3. Results

3.1 Soil Physicochemical Properties and Depth-related Patterns

Soil physicochemical properties exhibited clear and consistent vertical gradients across the three investigated depth layers (0-10, 10-20, and 20-40 cm), highlighting a pronounced depth-dependent structuring of organic matter and nutrient-related variables (Figure 3.1; Appendix Table A3).

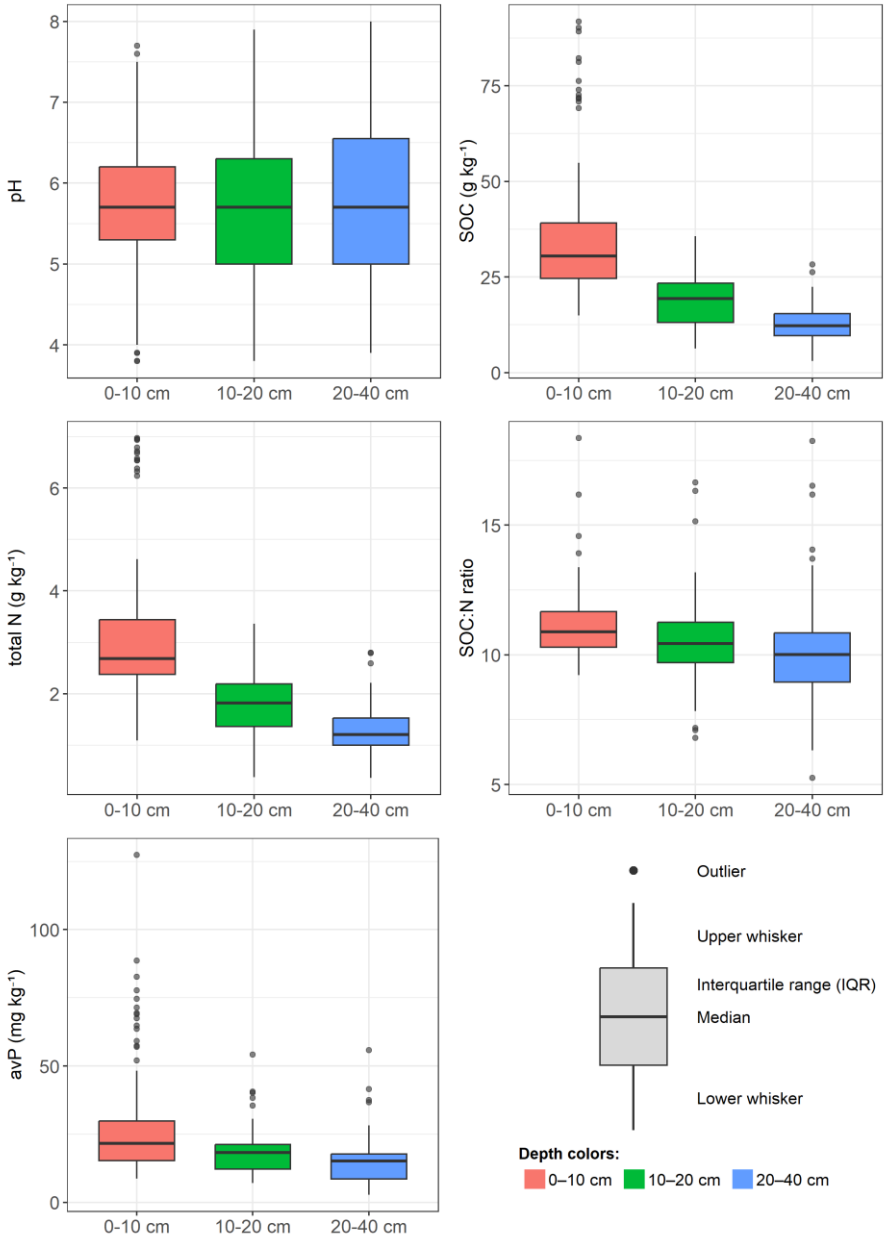

Figure 3.1. Distribution of selected pedological properties across soil depth layers. Soil pH, SOC, total N, SOC:N ratio, and available P (avP) exhibit clear depth-dependent patterns across the three sampled layers (0-10, 10-20, and 20-40 cm). Colors indicate soil depth layers. Boxes represent the interquartile range (IQR), horizontal lines indicate median values, whiskers extend to 1.5 × IQR, and points denote outliers. The schematic panel provides a guide for interpreting boxplots.

Among the investigated properties, SOC and total N showed the most marked depth-related patterns. Both variables decreased significantly with increasing soil depth, with mean SOC values declining from 34.9 g kg^{-1} in the 0-10 cm layer to 19.0 g kg^{-1} at 10-20 cm and 12.8 g kg^{-1} at 20-40 cm, and total N decreasing from 3.11 to 1.28 g kg^{-1} across the same depth range (Appendix Table A3). Linear mixed-effects models, accounting for repeated measurements within soil profiles, confirmed a highly significant effect of depth for both SOC and N ($p < 0.001$), with all pairwise comparisons among depth layers being statistically significant (Table 3.1). The intermediate layer (10-20 cm) consistently displayed values between surface and deeper soils, indicating a gradual vertical transition rather than an abrupt shift.

Table 3.1. Effects of soil depth on selected soil physicochemical properties based on linear mixed-effects models. Estimated marginal means (EMMs) ± standard error (SE) are reported.

Variable	Depth (cm)	EMM	SE	Group
SOC (g kg^{-1})	0-10	3.49	0.09	a
	10-20	1.90	0.09	b
	20-40	1.28	0.09	c
N (g kg^{-1})	0-10	0.311	0.007	a
	10-20	0.180	0.007	b
	20-40	0.128	0.007	c
PyC (g kg^{-1})	0-10	0.434	0.027	a
	10-20	0.214	0.027	b
	20-40	0.129	0.028	c
avP (mg kg^{-1})	0-10	27.0	1.59	a
	10-20	23.0	1.63	b
	20-40	19.8	1.64	c
pH	0-10	5.74	0.09	a
	10-20	5.76	0.09	a
	20-40	5.94	0.09	b

Note: different letters indicate statistically significant differences among depth layers ($p < 0.05$, Tukey-adjusted pairwise comparisons).

AvP concentrations also showed a significant decrease with depth, from an average of 27.0 mg kg^{-1} in the 0-10 cm layer to 23.0 mg kg^{-1} at 10-20 cm and 19.8 mg kg^{-1} at 20-40 cm (Figure 3.1; Appendix Table A3). Mixed-effects models indicated a highly significant depth effect ($p < 0.001$; Table 3.1), with statistically distinct avP levels among all depth layers. However, avP exhibited high coefficients of variation at all depths (CV ≈ 47-70%), reflecting pronounced spatial heterogeneity likely related to localized nutrient inputs and legacy fertilization effects.

In contrast, soil pH displayed comparatively modest vertical variation. Mean pH values increased slightly with depth, ranging from 5.74 in surface soils to 5.94 at 20-40 cm (Appendix Table A3). Although the absolute

differences were small, the effect of depth was statistically significant ($p < 0.01$; Table 3.1), with the deepest layer showing higher pH values than the two overlying layers. The SOC:N ratio exhibited only minor changes along the soil profile, decreasing slightly from 11.18 in the topsoil to 10.09 at 20-40 cm, while variability increased with depth (Figure 3.1; Appendix Table A3).

PyC concentrations followed a depth-dependent pattern closely resembling that of SOC. Descriptive statistics for SOC, PyC and PyC:SOC ratios across soil depth layers are reported in Appendix Table A4. Mean PyC values decreased from 4.3 g kg^{-1} in surface soils to 2.1 g kg^{-1} at 10-20 cm and 1.3 g kg^{-1} at 20-40 cm. The effect of depth on PyC was statistically significant ($p < 0.001$; Table 3.1), with distinct differences among all three layers. Despite this decline in absolute PyC concentrations, the relative contribution of PyC to SOC remained remarkably stable along the soil profile, with PyC:SOC ratios consistently around 10-11% across all depth layers (Appendix Table A4), suggesting proportional co-variation of pyrogenic and total organic carbon pools with depth.

Overall, these results demonstrate a strong vertical organization of soil physicochemical properties in the investigated urban and peri-urban forest soils. The consistent and statistically significant depth-related patterns observed for SOC, N, PyC, and avP highlight the dominant role of soil depth in controlling organic matter distribution and nutrient availability. The 10-20 cm layer emerges as a transitional horizon, retaining substantial amounts of organic carbon and nutrients while already reflecting increasing heterogeneity and declining concentrations compared to surface soils. This depth-dependent framework provides the basis for exploring the stabilization mechanisms and fractionation of PyC within soil organic matter pools, addressed in the following section.

3.2 Physical Fractionation of SOC and PyC into POM and MAOM

Physical fractionation highlighted a clear partitioning of both SOC and PyC between POM and MAOM fractions in the upper soil layers (0-10 and 10-20 cm; Table 3.2).

Table 3.2. Partitioning of soil organic carbon (SOC) and pyrogenic carbon (PyC) between particulate organic matter (POM) and mineral-associated organic matter (MAOM) fractions in surface (0-10 cm) and subsurface (10-20 cm) soil layers. Values are reported as mean ± standard deviation. Minimum and maximum values are shown in parentheses. Physical fractionation was performed only for the upper two soil layers.

Depth (cm)	SOC_POM (g kg^{-1})	SOC_MAOM (g kg^{-1})	PyC_POM (g kg^{-1})	PyC_MAOM (g kg^{-1})
0-10	23.54 ± 14.02 (8.74-70.04)	11.37 ± 4.98 (3.52-35.98)	2.24 ± 2.27 (0.43-12.38)	2.10 ± 3.17 (0.15-16.18)
10-20	12.96 ± 5.44 (3.74-28.56)	6.04 ± 2.5 (2.01-14.66)	1.13 ± 0.71 (0.27-3.85)	1.01 ± 0.92 (0.11-5.43)

Absolute SOC and PyC Contents

In absolute terms, both SOC and PyC contents decreased significantly with depth in both organic matter fractions. Mean SOC_POM declined from 23.54 ± 14.02 g kg^{-1} in the 0-10 cm layer to 12.96 ± 5.44 g kg^{-1} at 10-20 cm, while SOC_MAOM decreased from 11.37 ± 4.98 to 6.04 ± 2.57 g kg^{-1} over the same depth interval (Table 3.2). Linear mixed-effects models confirmed a highly significant effect of depth for both SOC_POM and SOC_MAOM ($p < 0.001$; Appendix Table A5).

Similarly, PyC concentrations showed a marked decline with depth in both fractions. Mean PyC_POM decreased from 2.24 ± 2.27 g kg^{-1} at 0-10 cm to 1.13 ± 0.71 g kg^{-1} at 10-20 cm, while PyC_MAOM decreased from 2.10 ± 3.17 to 1.01 ± 0.92 g kg^{-1} (Table 3.2). Depth effects were statistically significant for both PyC_POM and PyC_MAOM ($p < 0.001$; Appendix Table A5), indicating a consistent reduction of pyrogenic carbon with increasing depth regardless of the organic matter fraction considered.

Relative Distribution of SOC between POM and MAOM

When expressed as relative contributions, SOC exhibited a significant redistribution between fractions with depth. The proportion of SOC associated with the POM fraction increased slightly from 65.5% at 0-10 cm to 67.3% at 10-20 cm, while the relative contribution of SOC_MAOM decreased accordingly (Appendix Table A5). Mixed-effects models indicated that these changes were statistically significant ($p < 0.05$), suggesting a modest but systematic shift in SOC partitioning along the soil profile.

Relative Distribution of PyC between POM and MAOM

In contrast, the relative distribution of PyC between POM and MAOM fractions did not differ significantly between depths. PyC_POM accounted for approximately 56-57% of total PyC, while PyC_MAOM represented 43-44%, with no significant depth-related changes detected ($p > 0.05$; Appendix Table A5). This stability indicates that, unlike bulk SOC, the proportional allocation of PyC between organic matter pools remains conserved across the investigated depth range.

PyC:SOC Ratios within Fractions

Consistently, PyC:SOC ratios calculated separately for POM and MAOM fractions did not show significant depth-related differences ($p > 0.05$; Appendix Table A5). Mean PyC:SOC ratios were comparable between 0-10 and 10-20 cm in both fractions, indicating proportional co-variation of pyrogenic and total organic carbon within each pool.

Overall, these results indicate that while absolute amounts of SOC and PyC decrease significantly with depth in both POM and MAOM fractions, the relative partitioning of PyC between organic matter pools remains remarkably stable. The significant redistribution observed for SOC, contrasted with the conservative behavior of PyC, supports the hypothesis that a substantial fraction of pyrogenic carbon becomes associated with mineral surfaces at early stages and maintains a stable allocation with depth. This depth-independent

partitioning and proportional co-variation with SOC suggest early and persistent stabilization mechanisms for PyC within soil organic matter pools.

3.3 Effects of Urban Concentric Zones on PyC-related Properties

The influence of the spatial position of green areas within the urban matrix was evaluated by comparing PyC-related properties across concentric urban zones (inner, intermediate, and outer), using linear mixed-effects models accounting for site-level variability and green area age.

Across surface and subsurface layers (0-10 and 10-20 cm), neither absolute PyC (PyC_abs) concentrations nor PyC:SOC ratios differed significantly among urban zones ($p > 0.1$; Table 3.3). Estimated marginal means were comparable across zones, and confidence intervals largely overlapped, indicating a limited effect of spatial position within the city on near-surface PyC abundance and its relative contribution to total soil organic carbon.

Table 3.3. Effects of urban concentric zones on PyC-related properties across soil depth layers. Estimated marginal means (EMMs) ± standard error (SE) derived from linear mixed-effects models including urban zone as fixed effect and site as random effect. Green area age was included as a covariate.

Variable	Depth (cm)	Urban zone	EMM ± SE	Group	*p* (urban zone)
PyC_abs (g kg^{-1})	0-10	inner	0.545 ± 0.091	a	0.420
		intermediate	0.484 ± 0.038	a	
		outer	0.565 ± 0.061	a	
	10-20	inner	0.323 ± 0.044	a	0.304
		intermediate	0.247 ± 0.019	a	
		outer	0.258 ± 0.030	a	
	20-40	inner	0.248 ± 0.030	a	***0.0077***
		intermediate	0.139 ± 0.012	b	
		outer	0.129 ± 0.020	b	
PyC:SOC ratio	0-10	inner	0.133 ± 0.014	a	0.125
		intermediate	0.113 ± 0.006	a	
		outer	0.130 ± 0.009	a	
	10-20	inner	0.157 ± 0.017	a	0.446
		intermediate	0.133 ± 0.008	a	
		outer	0.129 ± 0.012	a	
	20-40	inner	0.168 ± 0.021	a	0.101
		intermediate	0.117 ± 0.009	a	
		outer	0.113 ± 0.014	a	

Note: different letters indicate statistically significant differences among urban zones ($p < 0.05$). Estimated marginal means (EMMs) ± standard error (SE) derived from linear mixed-effects models testing the effect of urban concentric zones (inner, intermediate, outer) on bulk pyrogenic carbon properties. Models included green area age as a covariate and site as a random effect. Different letters indicate statistically significant differences among urban zones ($p < 0.05$).

In contrast, a significant effect of urban zone was detected for PyC concentrations in the deepest investigated layer (20-40 cm; $p = 0.0077$; Table 3.3). In this layer, inner urban soils exhibited higher PyC concentrations compared to both intermediate and outer zones, which did not differ from each other. This pattern suggests a greater accumulation or persistence of PyC in deeper mineral soils within the urban core.

Indices describing PyC stabilization pathways were not affected by urban zoning. Neither the PyC POM:MAOM ratio nor the MAOM-associated PyC share showed significant differences among zones at either 0-10 or 10-20 cm depth ($p > 0.3$; Appendix Table A6), indicating comparable partitioning of PyC between particulate and mineral-associated pools regardless of spatial position within the city.

Overall, these results indicate that while urban concentric position may influence PyC storage in deeper soil layers, particularly within the urban core, PyC abundance, relative contribution to SOC, and stabilization pathways in surface soils are primarily controlled by factors other than spatial location within the urban matrix.

3.4 PyC across Green Area Categories

3.4.1 PyC Concentration and Relative Contribution to SOC across Green Area Categories

PyC concentrations in surface soils (0-10 cm) differed significantly among green area categories, reflecting contrasts in land-use history, vegetation structure, management intensity, and ecosystem development stage (Figure 3.2; Table 3.4).

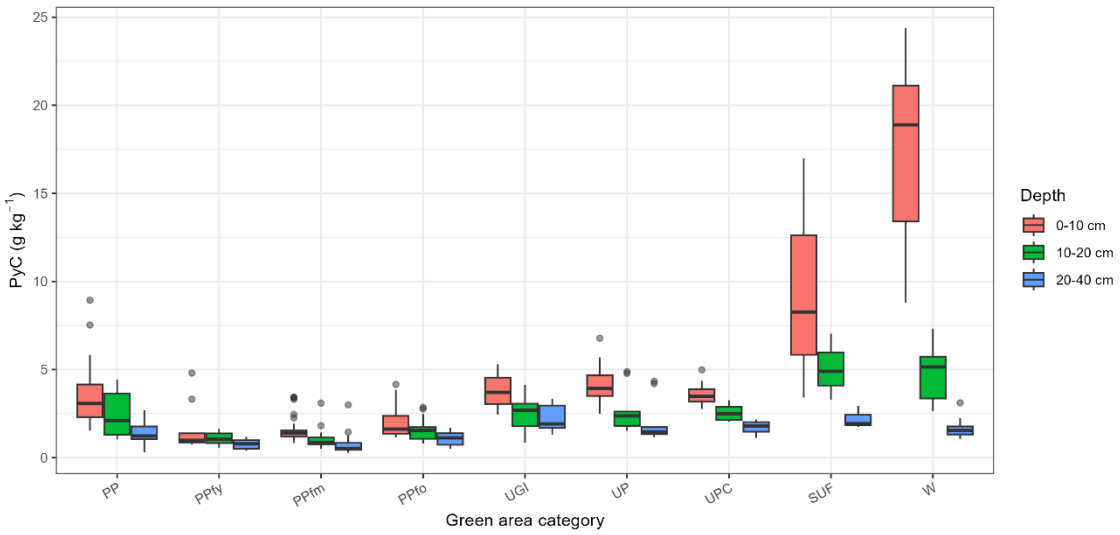

Figure 3.2. Distribution of pyrogenic carbon (PyC) concentrations across green area categories, shown separately for the three sampled soil depth layers (0-10 cm, 10-20 cm, and 20-40 cm). Colors indicate soil depth layers. Boxes represent the interquartile range (IQR), horizontal lines indicate median values, whiskers extend to 1.5 × IQR, and points denote outliers. Green area category abbreviations are defined in Materials and Methods (Section 2.1).

Table 3.4. Estimated marginal means (emmean), standard errors (SE), and significance groups (group) for soil parameters across green area categories (age-stratified), obtained from parametric mixed-effects models (LMM/GLMM). Significance groups are based on post-hoc comparisons of estimated marginal means using Tukey-adjusted tests; for GLMMs, estimated marginal means were regridded to the response scale prior to post-hoc comparisons. Green area category abbreviations are defined in Section 2.1.

Parameter	Statistic	PP	PPfy	PPfm	PPfo	UGI	UP	UPC	SUF	W
SOC1	emmean	1.132	0.988	1.099	0.963	1.139	1.176	1.164	1.450	1.811
	SE	0.069	0.086	0.081	0.081	0.100	0.100	0.100	0.419	0.208
	group	ab	a	a	a	ab	ab	ab	ab	b
SOC2	emmean	1.728	2.109	1.848	1.637	1.771	1.591	2.040	1.799	2.928
	SE	0.131	0.165	0.133	0.144	0.189	0.189	0.189	0.530	0.266
	group	a	ab	a	a	a	a	ab	ab	b
SOC3	emmean	-0.020	0.591	0.230	0.029	0.297	0.021	0.222	0.080	0.531
	SE	0.104	0.131	0.121	0.122	0.159	0.159	0.151	0.603	0.303
	group	a	b	a	a	ab	ab	ab	ab	ab
PyC2	emmean	0.203	0.122	0.122	0.111	0.221	0.237	0.249	0.502	0.478
	SE	0.024	0.019	0.017	0.016	0.039	0.041	0.044	0.349	0.167
	group	b	ab	ab	a	ab	ab	ab	ab	ab
SOC_MAOM1	emmean	0.802	0.616	0.708	0.700	0.677	0.786	1.002	0.607	0.802
	SE	0.043	0.060	0.043	0.049	0.063	0.063	0.063	0.156	0.078
	group	ab	a	a	a	a	ab	b	ab	ab
SOC_POM2	emmean	1.152	1.431	1.201	1.092	1.263	1.067	1.001	1.384	2.339
	SE	0.094	0.123	0.096	0.105	0.137	0.137	0.137	0.373	0.187
	group	a	a	a	a	a	a	a	ab	b
SOC_MAOM2	emmean	0.441	0.513	0.486	0.423	0.404	0.413	0.706	0.342	0.456
	SE	0.033	0.041	0.033	0.036	0.047	0.047	0.047	0.133	0.067
	group	a	ab	a	a	a	a	b	ab	ab
PyC_POM2	emmean	0.111	0.069	0.066	0.062	0.137	0.129	0.141	0.306	0.183
	SE	0.014	0.011	0.010	0.009	0.025	0.024	0.026	0.229	0.069
	group	a	a	a	a	a	a	a	a	a
PyC:SOC2 ratio	emmean	0.125	0.059	0.065	0.076	0.140	0.165	0.125	0.279	0.164
	SE	0.011	0.007	0.007	0.008	0.018	0.021	0.016	0.136	0.040
	group	c	a	a	ab	c	c	bc	abc	abc
PyC_POM:MAOM2 ratio	emmean	0.538	0.574	0.538	0.532	0.588	0.518	0.539	0.584	0.366
	SE	0.018	0.025	0.018	0.021	0.026	0.026	0.026	0.065	0.032
	group	b	b	b	b	b	b	b	ab	a

Although the overall mean PyC content in the 0-10 cm layer was 4.34 ± 5.18 g kg^{-1} (Appendix Table A4), category-specific values spanned more than one order of magnitude, highlighting pronounced heterogeneity across the urban and peri-urban landscape.

The lowest PyC concentrations were consistently observed in Periurban Parks (PP) dominated by grasslands and recreational lawns, where the absence of developed forest canopies was associated with limited PyC accumulation. Within forested Periurban Parks (PPf), a clear age-dependent pattern emerged. Young forest stands (PPfy, 10-20 years) and mid-aged stands (PPfm, 21-40 years) showed relatively low surface PyC

contents (generally < 2 g kg^{-1}), whereas older afforestations (PPfo, 41-60 years) exhibited higher values, approaching those observed in more structurally complex systems.

Intermediate PyC concentrations characterized Urban Parks (UP), Central Urban Parks (UPC), and Urban Green Infrastructures (UGI). Despite strong differences in spatial configuration and fragmentation, these categories typically showed mean surface PyC contents between ~3 and 4 g kg^{-1}, suggesting that repeated anthropogenic inputs and mixed vegetation structures can sustain moderate PyC levels even in highly managed or fragmented environments.

In contrast, the highest PyC concentrations were recorded in Spontaneous Urban Forests (SUF) and ancient Woodlands (W). Spontaneous Urban Forests showed elevated surface PyC values (mean 9.55 ± 6.88 g kg^{-1}), while ancient peri-urban woodlands exhibited the largest accumulation (17.56 ± 5.00 g kg^{-1}), with local maxima exceeding 15-20 g kg^{-1} (Figure 3.2). These two categories consistently occupied the upper significance groups in post-hoc comparisons, indicating significantly higher PyC concentrations compared to most other green area types (Table 3.4). Patterns of significance were consistent when tested using non-parametric approaches, with grouping results from Kruskal-Wallis and post-hoc Wilcoxon tests reported as supporting information in Appendix Table A7.

Across all green area categories, PyC concentrations declined with soil depth, following the general vertical pattern described above. Mean PyC values decreased to 2.14 ± 1.50 g kg^{-1} at 10-20 cm and to 1.29 ± 0.76 g kg^{-1} at 20-40 cm (Appendix Table A4). Differences among categories were most pronounced in surface soils, weakened at 10-20 cm, and largely disappeared at 20-40 cm, where PyC contents became more homogeneous and no single category consistently differed from all others.

The relative contribution of PyC to soil organic carbon, expressed as the PyC:SOC ratio, showed patterns broadly consistent with those observed for absolute PyC concentrations (Figure 3.3; Table 3.4).

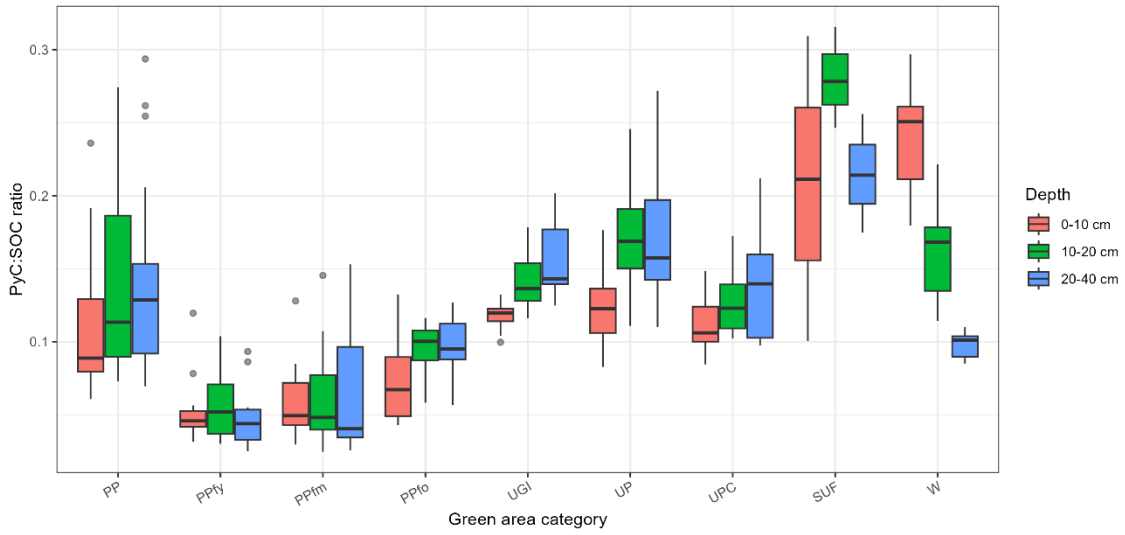

Figure 3.3. Distribution of the PyC:SOC ratio across green area categories (age-stratified) for the three sampled soil depth layers (0-10 cm, 10-20 cm, and 20-40 cm). Boxplots show median values (horizontal line), interquartile range (box), and whiskers extending to 1.5 × IQR.

In surface soils, PP and younger PPf stands exhibited low PyC:SOC ratios, whereas higher ratios characterized older forested systems (W) and SUF. Intermediate values were observed in UP, UPC, and UGI. Category-specific differences in PyC:SOC ratios were statistically significant in the 0-10 cm layer ($p < 0.001$) and remained detectable at 10-20 cm ($p < 0.05$), but contrasts among categories largely disappeared at 20-40 cm depth ($p > 0.05$).

Overall, these results indicate that land-use legacy and ecosystem development stage exert strong control on both absolute PyC concentrations and its proportional contribution to SOC, with the clearest category-specific signals confined to surface and subsurface soils (0-20 cm) and progressively weaker differentiation with increasing depth.

3.4.2 Partitioning of PyC between POM and MAOM Fractions across Green Area Categories

Physical fractionation revealed marked differences in the partitioning of PyC between POM and MAOM fractions across green area categories, highlighting contrasting stabilization pathways along the urban-peri-urban gradient (Figure 3.4; Table 3.5).

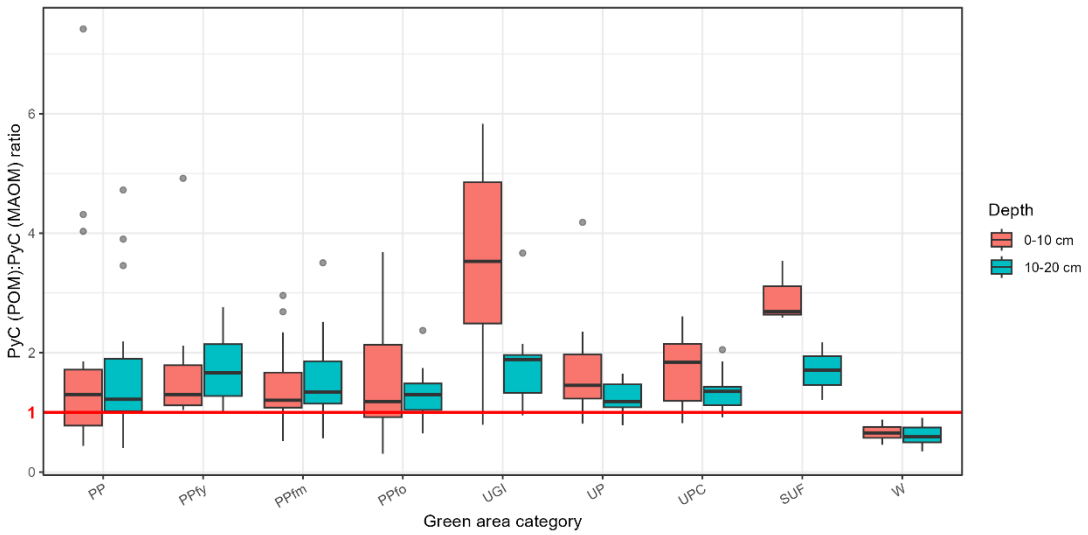

Figure 3.4. Distribution of the PyC (POM):PyC (MAOM) ratio across green area categories (age-stratified) for the two surface soil layers (0-10 cm and 10-20 cm). Boxplots display median values (horizontal line), interquartile range (box), and whiskers extending to 1.5 × IQR. The horizontal red line marks a ratio of 1, separating POM-dominated (>1) from MAOM-dominated (<1) PyC partitioning.

Table 3.5. Partitioning of pyrogenic carbon (PyC) between particulate organic matter (PyC_POM) and mineral-associated organic matter (PyC_MAOM) fractions across green area categories and soil depth layers (0-10 and 10-20 cm). Values are reported as mean ± standard deviation, with minimum and maximum values shown in parentheses. The PyC_POM:MAOM ratio expresses the relative dominance of particulate- versus mineral-associated PyC within each soil layer and green area category.

Green area	Depth (cm)	n	PyC_POM (g kg^{-1})	PyC_MAOM (g kg^{-1})	PyC_POM:MAOM
PP	0-10	21	2.12 ± 1.60 (0.89-7.25)	1.53 ± 0.87 (0.64-4.03)	1.72 ± 1.65 (0.44-7.42)
PP	10-20	21	1.38 ± 0.80 (0.55-2.90)	1.00 ± 0.60 (0.44-2.19)	1.62 ± 1.11 (0.40-4.72)
PPfy	0-10	11	0.88 ± 0.64 (0.45-2.53)	0.68 ± 0.66 (0.15-2.27)	1.72 ± 1.12 (1.04-4.92)
PPfy	10-20	11	0.67 ± 0.24 (0.38-1.17)	0.41 ± 0.17 (0.16-0.70)	1.78 ± 0.58 (1.01-2.77)
PPfm	0-10	36	0.90 ± 0.38 (0.43-2.02)	0.72 ± 0.38 (0.27-1.91)	1.39 ± 0.55 (0.52-2.96)
PPfm	10-20	36	0.57 ± 0.26 (0.27-1.73)	0.43 ± 0.22 (0.11-1.37)	1.50 ± 0.60 (0.57-3.51)
PPfo	0-10	19	1.02 ± 0.27 (0.75-1.74)	1.01 ± 0.82 (0.24-3.06)	1.55 ± 0.97 (0.31-3.68)
PPfo	10-20	19	0.83 ± 0.28 (0.40-1.37)	0.71 ± 0.39 (0.26-1.68)	1.30 ± 0.40 (0.65-2.37)
UGI	0-10	10	2.87 ± 0.94 (1.08-3.99)	0.93 ± 0.36 (0.48-1.37)	3.57 ± 1.70 (0.79-5.83)
UGI	10-20	10	1.56 ± 0.59 (0.42-2.29)	0.95 ± 0.48 (0.36-1.84)	1.83 ± 0.77 (0.95-3.67)
UP	0-10	10	2.51 ± 0.77 (1.61-3.89)	1.69 ± 0.83 (0.88-3.14)	1.76 ± 0.98 (0.81-4.18)
UP	10-20	10	1.45 ± 0.75 (0.80-2.89)	1.18 ± 0.50 (0.59-2.12)	1.23 ± 0.27 (0.78-1.65)
UPC	0-10	10	2.21 ± 0.50 (1.82-3.40)	1.40 ± 0.49 (0.76-2.39)	1.75 ± 0.62 (0.82-2.61)
UPC	10-20	10	1.43 ± 0.24 (1.19-1.91)	1.10 ± 0.28 (0.67-1.41)	1.37 ± 0.36 (0.92-2.05)
SUF	0-10	3	7.09 ± 4.99 (2.46-12.38)	2.46 ± 1.91 (0.95-4.61)	2.94 ± 0.52 (2.59-3.54)
SUF	10-20	3	3.06 ± 0.80 (2.25-3.85)	2.01 ± 1.09 (1.04-3.18)	1.70 ± 0.48 (1.21-2.17)
W	0-10	14	6.95 ± 2.15 (3.18-10.05)	10.61 ± 3.10 (4.77-16.18)	0.66 ± 0.13 (0.46-0.88)
W	10-20	14	1.75 ± 0.49 (0.95-2.58)	3.03 ± 1.09 (1.52-5.43)	0.61 ± 0.16 (0.35-0.91)

Patterns were most pronounced in surface soils (0-10 cm), whereas results for the 10-20 cm layer showed similar but generally attenuated trends. In surface soils, younger afforested systems and intensively managed green spaces were characterized by a predominance of POM-associated PyC, while older forested systems exhibited a progressively greater association of PyC with the MAOM fraction.

Ancient peri-urban woodlands (W) showed a clear dominance of MAOM-associated PyC already in surface soils, with mean PyC_MAOM concentrations (10.61 ± 3.10 g kg^{-1}) exceeding PyC_POM values (6.95 ± 2.15 g kg^{-1}) and resulting in consistently low PyC_POM:MAOM ratios (< 1; mean 0.66 ± 0.13; Table 3.5). This pattern indicates advanced stabilization of PyC within mineral-associated pools in long-established forest ecosystems.

In contrast, Urban Green Infrastructures (UGI) and Spontaneous Urban Forest (SUF) exhibited higher PyC_POM:MAOM ratios in the 0-10 cm layer (UGI: 3.57 ± 1.70; SUF: 2.94 ± 0.52), suggesting a greater relative contribution of particulate PyC despite relatively high total PyC concentrations. These systems appear to retain a substantial fraction of PyC in more labile, POM-associated forms.

Forested peri-urban parks (PPf) displayed intermediate behaviour. Across the three age classes (PPfy, PPfm, PPfo), absolute PyC concentrations were lower than in mature forests, yet a considerable proportion of PyC was already associated with the MAOM fraction. In surface soils, PyC_POM:MAOM ratios ranged between 1.39 ± 0.55 and 1.72 ± 1.12, corresponding to MAOM-associated PyC shares of approximately 40-45% (Table 3.5; Appendix Table A8). Comparable MAOM shares were observed in the 10-20 cm layer, although with reduced absolute PyC contents. This indicates that mineral-associated stabilization processes are active even in relatively young forested systems, albeit at lower overall PyC contents.

Across all green area categories, PyC concentrations in both POM and MAOM fractions generally decreased with depth (10-20 cm), while category-specific differences in PyC partitioning remained detectable but weaker than in surface soils (Figure 3.4; Table 3.5). Parametric mixed-effects models confirmed a significant effect of green area category on PyC partitioning in surface soils (0-10 cm; $p < 0.05$), whereas differences among categories were less pronounced and not consistently significant at 10-20 cm depth (Table 3.4). Non-parametric analyses yielded comparable grouping patterns and are reported as supporting information in Appendix Table A7.

Overall, these results demonstrate that land-use legacy and ecosystem development strongly influence not only the amount of PyC stored in soils but also its stabilization pathway, with a progressive shift from POM-dominated PyC pools in younger or intensively managed systems toward predominantly MAOM-associated PyC in older and structurally complex forest ecosystems.

4. Discussion

Overall, the magnitude of PyC concentrations observed in Milanese urban and peri-urban soils is consistent with values reported for other urban environments worldwide.

Comparable levels of combustion-derived carbon have been documented in urban greenspaces across European settings, particularly in the United Kingdom. For instance, studies conducted in the city of Leicester and across urban soils in the North-East of England reported substantial stocks and concentrations of combustion-derived carbon within surface and subsurface horizons, highlighting the long-term accumulation of pyrogenic material in urban soils subjected to chronic atmospheric inputs (Edmondson *et al.*, 2012; Edmondson *et al.*, 2015).

In the Milan context, these findings align well with previous evidence showing elevated soil carbon stocks in urban green areas, including parks and long-established greenspaces, where atmospheric deposition and limited soil disturbance promote carbon accumulation (Canedoli *et al.*, 2020).

At a broader scale, inventories and syntheses indicate that PyC constitutes a widespread and persistent component of urban soil organic matter across contrasting climatic and land-use contexts, although its absolute abundance and relative contribution to SOC vary markedly among sites (Reisser *et al.*, 2016).

Similar PyC concentrations have also been reported in non-European cities, such as rapidly urbanizing regions in China, where urban soils receive sustained inputs from traffic and fossil fuel combustion (Wang, 2010).

Together, these studies support the interpretation that the PyC concentrations measured in Milan fall within the upper range reported for urban soils, particularly in long-established and weakly disturbed green areas, reinforcing the relevance of Milan as a representative case study for investigating PyC accumulation and stabilization in urban and peri-urban environments.

4.1 Depth-dependent Patterns of SOC and PyC in Urban and Peri-urban Soils

The observed decline of SOC and total N concentrations with increasing soil depth is consistent with well-established patterns reported for both natural and managed soils, reflecting decreasing organic inputs, biological activity and root density with depth (Jobbágy & Jackson, 2000; Kögel-Knabner *et al.*, 2008). In the present study, this vertical gradient was particularly pronounced for SOC and total N, whereas PyC showed a parallel but less steep decrease across soil layers.

As a consequence, the PyC:SOC ratio remained relatively stable along the soil profile, indicating that pyrogenic carbon represents a persistent component of the soil organic carbon pool beyond surface horizons. Similar depth-invariant contributions of PyC to SOC have been reported for urban and peri-urban soils in European contexts, where combustion-derived carbon accounts for a substantial and relatively constant fraction of SOC across multiple depth layers (Edmondson *et al.*, 2015; Lehndorff *et al.*, 2014).

The persistence of PyC at depth likely reflects a combination of mechanisms, including downward transport of fine pyrogenic particles, physical protection within aggregates, and progressive stabilization through organo-mineral associations (Hockaday *et al.*, 2007; Major *et al.*, 2010; Lehmann & Kleber, 2015). These

processes may act in parallel to redistribute PyC within the upper mineral soil while limiting its microbial mineralization.

The intermediate properties observed in the 10-20 cm layer further support the interpretation of a gradual vertical transition rather than an abrupt stratification. This horizon retained considerable amounts of SOC, PyC and nutrients, while already exhibiting increased variability and declining concentrations compared to surface soils. Such behaviour highlights the functional relevance of the subsoil interface in urban soil profiles, where both surface-derived inputs and deeper soil-forming processes interact.

4.2 Influence of Green Area Type and Ecosystem Development on PyC Accumulation

Beyond depth effects, green area category emerged as a major control on PyC accumulation in surface soils. The lowest PyC concentrations were consistently observed in younger afforested peri-urban parks (PPfy and PPfm), suggesting limited time for the accumulation of combustion-derived carbon in recently established forest soils (Reisser *et al.*, 2016; Santín *et al.*, 2015). Although these sites are currently forested, their soils developed under agricultural land use, which may have constrained baseline SOC stocks prior to afforestation and limited the long-term capacity of these soils to retain combustion-derived carbon inputs (Compton & Boone, 2000).

In contrast, spontaneous Urban Forests (SUF) and mature peri-urban forests (W) exhibited markedly higher PyC concentrations, with values locally exceeding 15-20 g kg^{-1}. These systems represent long-established ecosystems with prolonged exposure to atmospheric deposition from traffic emissions, domestic heating, and historical combustion sources. In the case of SUF, the exceptionally high PyC contents are likely further amplified by the industrial legacy of the site, which developed on former gasometer and industrial land (La Goccia), historically exposed to intense fossil-fuel combustion and soot deposition. Their well-developed canopy structure, persistent litter layers, and reduced soil disturbance likely enhance the interception, retention, and gradual incorporation of combustion-derived particles into surface soils, promoting long-term PyC accumulation (Ponette-González *et al.*, 2022). Over decades, this combination of sustained inputs and stabilizing ecosystem conditions appears to favour the progressive enrichment of PyC in surface horizons.

Semi-natural grasslands and urban parks displayed intermediate PyC levels, suggesting that both land-use legacy and management intensity modulate PyC accumulation. Frequent mowing, litter removal, and soil disturbance may limit the long-term retention of PyC despite ongoing atmospheric inputs, resulting in PyC concentrations lower than those observed in mature forests but higher than in recently afforested systems. Similar patterns have been reported for urban soils in other metropolitan areas, where vegetation structure and management regime were found to strongly influence black carbon and PyC contents (Schifman *et al.*, 2018). Overall, these results indicate that ecosystem development stage and green area typology exert a stronger control on PyC accumulation than simple exposure to urban emission sources. Long-established forested systems act as effective sinks for combustion-derived carbon, whereas younger or intensively managed green spaces show reduced PyC storage capacity, despite their location within the urban and peri-urban matrix.

4.3 PyC Contribution to SOC and Implications for Urban Carbon Persistence

The PyC:SOC ratio provided additional insight into the functional role of pyrogenic carbon within the total organic carbon pool. Younger afforested systems displayed low PyC:SOC ratios, reflecting SOC pools dominated by biogenic inputs and limited long-term accumulation of combustion-derived carbon (Santín *et al.*, 2015; Reisser *et al.*, 2016). In contrast, mature forests (W) and Spontaneous Urban Forests (SUF) exhibited substantially higher ratios, indicating that PyC represents a significant and non-negligible fraction of total SOC in these systems, consistent with observations from other urban and peri-urban environments (Edmondson *et al.*, 2015; Reisser *et al.*, 2016).

The persistence of category-specific differences in PyC:SOC ratios down to 10-20 cm depth suggests that ecosystem development influences not only surface accumulation but also the vertical redistribution and stabilization of PyC within mineral soil layers. This pattern supports the hypothesis that pyrogenic particles can be progressively incorporated into deeper soil horizons through physical translocation, aggregate formation and organo-mineral interactions (Schmidt *et al.*, 2011; Wang *et al.*, 2016).

At greater depth (20-40 cm), the convergence of PyC:SOC ratios across categories indicates that deeper soil layers are less sensitive to land-use history and vegetation structure, and increasingly governed by general soil-forming processes and long-term stabilization mechanisms (Lehmann & Kleber, 2015; Cotrufo *et al.*, 2019).

Overall, these findings reinforce the view that PyC is not merely an inert background component of urban soils but a dynamic contributor to SOC pools, with implications for long-term carbon persistence, stabilization pathways and soil carbon turnover in urban and peri-urban ecosystems (Schmidt *et al.*, 2011; Santín *et al.*, 2015).

4.4 Stabilization Pathways of PyC: POM versus MAOM Association

Physical fractionation revealed clear differences in PyC stabilization pathways along the urban-peri-urban gradient, with marked contrasts among green area categories consistent with the patterns observed. In younger and managed systems, PyC was predominantly associated with the POM fraction, indicating relatively recent inputs and limited interaction with mineral surfaces. This pattern suggests that, despite the intrinsic chemical recalcitrance of PyC, particulate-associated PyC remains comparatively exposed to physical disturbance and microbial processing (Schmidt *et al.*, 2011; Hockaday *et al.*, 2007).

In contrast, mature forests showed a dominant association of PyC with the MAOM fraction, even in surface soils. The high proportion of MAOM-associated PyC (>50% of total PyC) observed in these systems indicates effective long-term stabilization through organo-mineral interactions. This shift toward MAOM-dominated PyC pools mirrors well-established stabilization pathways described for non-pyrogenic SOC and supports current conceptual frameworks emphasizing mineral association as a key mechanism controlling long-term carbon persistence in soils (Cotrufo *et al.*, 2013; Cotrufo *et al.*, 2019; Angst *et al.*, 2017).

Experimental fractionation and density-based studies have shown that combustion-derived carbon can occur in both particulate and mineral-associated pools, with mineral association enhancing long-term persistence through sorption and aggregation processes (Llorente *et al.*, 2010).

Spontaneous urban forests and peri-urban planted forests showed intermediate behaviour. Although total PyC contents were lower than in mature forests, a substantial fraction of PyC was already associated with the MAOM pool, particularly in older afforestation stages. This suggests that mineral-associated stabilization processes can become active relatively early during ecosystem development, even under urban conditions, provided that soil disturbance is limited and vegetation structure becomes sufficiently complex (Wang *et al.*, 2016; Poeplau *et al.*, 2024).

Across all categories, PyC concentrations in both POM and MAOM fractions declined with depth, while category-specific differences in PyC partitioning became less pronounced at 10-20 cm depth. This attenuation with depth is consistent with reduced biological inputs, lower aggregate turnover, and increasing dominance of long-term stabilization mechanisms in subsurface horizons (Schmidt *et al.*, 2011; Lehmann & Kleber, 2015). Overall, these results demonstrate that land-use legacy and ecosystem development strongly influence not only the amount of PyC stored in soils but also its dominant stabilization pathway.

4.5 Limited Role of Spatial Position within the Urban Matrix

The absence of significant differences in PyC-related properties among concentric urban zones indicates that spatial position within the city plays a secondary role compared to green area category and ecosystem development stage. Despite expected gradients in traffic intensity, population density and atmospheric deposition across the urban core and peri-urban areas, PyC accumulation, and relative contribution to SOC stabilization pathways did not differ consistently among inner, intermediate and outer zones.

This finding suggests that local-scale controls - such as vegetation structure, soil properties, land-use history and management intensity - override broader urbanization gradients in shaping PyC dynamics. Similar conclusions have been reported for other soil carbon fractions in urban environments, where site-specific characteristics were shown to be stronger predictors of SOC quantity and quality than simple distance-to-centre metrics (Edmondson *et al.*, 2014; Lorenz & Lal, 2018).

The lack of a clear concentric pattern further implies that atmospheric PyC inputs may be relatively diffuse at the scale of the Milan metropolitan area, or that post-depositional processes rapidly redistribute and stabilize PyC within soils regardless of source proximity. This reinforces the view that urban soil carbon dynamics cannot be fully explained by spatial urbanization gradients alone, but require explicit consideration of ecosystem development and soil stabilization processes (Reisser *et al.*, 2016; Santín *et al.*, 2015).

5. Conclusions

This study provides a comprehensive assessment of PyC dynamics in urban and peri-urban soils across the Metropolitan City of Milan, integrating depth distribution, land-use history and physical stabilization mechanisms.

The main conclusions can be summarized as follows:

- PyC represents a substantial and persistent component of soil organic carbon in urban soils, accounting on average for approximately 10-11% of total SOC across the investigated soil profile (0-40 cm), despite a marked decline in absolute concentrations with depth.
- Green area type and ecosystem development strongly control PyC accumulation. Mature peri-urban forests and spontaneous urban forests exhibited the highest PyC contents, with surface concentrations locally exceeding 15-20 g kg^{-1} and elevated PyC:SOC ratios, whereas younger afforested systems remained dominated by biogenic SOC and showed comparatively lower PyC storage.
- Non-forested urban green areas, including urban parks, central parks and green infrastructures, displayed intermediate PyC concentrations, indicating that even intensively managed and fragmented green spaces can retain appreciable amounts of combustion-derived carbon under sustained atmospheric inputs.
- Physical fractionation revealed a clear shift in PyC stabilization pathways, from predominantly POM-associated pools in younger or managed systems to MAOM-dominated pools in older forest ecosystems, where more than 50% of total PyC was mineral-associated, indicating progressive long-term stabilization.
- Spatial position within the urban matrix plays a minor role, as PyC abundance, relative contribution to SOC and stabilization pathways did not differ consistently among concentric urban zones once ecosystem type and development stage were accounted for.

Overall, these findings highlight the importance of considering PyC as an integral component of urban soil carbon pools. Urban forests and long-established green areas not only store substantial amounts of SOC but also act as effective sinks for stabilized PyC, with important implications for urban carbon budgets, soil functioning and the long-term legacy of combustion-derived inputs in cities.

References

Angst, G., Mueller, K. E., Kögel-Knabner, I., Freeman, K. H., & Mueller, C. W. (2017). Aggregation controls the stability of lignin and lipids in clay-sized particulate and mineral associated organic matter. *Biogeochemistry*, 132(3), 307-324. https://doi.org/10.1007/s10533-017-0304-2.

Bird, M. I., Wynn, J. G., Saiz, G., Wurster, C. M., & McBeath, A. (2015). The pyrogenic carbon cycle. *Annual Review of Earth and Planetary Sciences*, 43, 273-298. https://doi.org/10.1146/annurev-earth-060614-105038.

Canedoli, C., Ferrè, C., Abu El Khair, D., Padoa-Schioppa, E., & Comolli, R. (2020). Soil organic carbon stock in different urban land uses: high stock evidence in urban parks. *Urban Ecosystems*, 23, 159-171. https://doi.org/10.1007/s11252-019-00901-6.

Compton, J. E., & Boone, R. D. (2000). Long-term impacts of agriculture on soil carbon and nitrogen in New England forests. *Ecology*, 81(8), 2314-2330. https://doi.org/10.1890/0012-9658(2000)081[2314:LTIOAO]2.0.CO;2.

Cotrufo, M. F., Ranalli, M. G., Haddix, M. L., Six, J., & Lugato, E. (2019). Soil carbon storage informed by particulate and mineral-associated organic matter. *Nature Geoscience*, 12, 989-994. https://doi.org/10.1038/s41561-019-0484-6.

Cotrufo, M. F., Wallenstein, M. D., Boot, C. M., Denef, K., & Paul, E. (2013). The Microbial Efficiency-Matrix Stabilization (MEMS) framework integrates plant litter decomposition with soil organic matter stabilization: do labile plant inputs form stable soil organic matter? *Global Change Biology*, 19(4), 988-95. https://doi.org/10.1111/gcb.12113.

Day, R. P. (1965) Pipette Method of Particle Size Analysis. In: *Methods of Soil Analysis*, Agronomy No. 9, ASA, Madison, 553-562.

De Feudis, C. (2026). Ecological condition and functioning of urban soils in public green spaces: a multi-dimensional assessment in Milan, Italy. *Doctoral Dissertation*, Milano-Bicocca University.

Edmondson, J. L., Davies, Z. G., Gaston, K. J., & Leake, J. R. (2014). Urban cultivation in allotments maintains soil qualities adversely affected by conventional agriculture. *Journal of Applied Ecology*, 51(4), 880-889. https://doi.org/10.1111/1365-2664.12254.

Edmondson, J. L., Davies, Z. G., McHugh, N. Gaston, K. L., & Leake, J. R. (2012). Organic carbon hidden in urban ecosystems. *Scientific Reports*, 2, 963. https://doi.org/10.1038/srep00963.

Edmondson, J. L., Stott, I., Potter, J., Lopez-Capel, E., Manning, D. A. C., Gaston, K. J., & Leake, J. R. (2015). Black carbon contribution to organic carbon stocks in urban soil. *Environmental Science & Technology*, 49(14), 8339-8346. https://doi.org/10.1021/acs.est.5b00313.

Elmquist, M., Gustafsson, Ö., & Andersson, P. (2004). Quantification of sedimentary black carbon using the chemothermal oxidation method: an evaluation of ex situ pretreatments and standard additions approaches. *Limnology and Oceanography: Methods*, 2, 417-427. https://doi.org/10.4319/lom.2004.2.417.

Gustafsson, Ö., Bucheli, T. D., Kukulska, Z., Andersson, M., Largeau, C., Rouzaud, J-N., Reddy, C. M. & Eglinton, T. I. (2001). Evaluation of a protocol for the quantification of black carbon in sediments. *Global Biogeochemical Cycles*, 15(4), 881-890. https://doi.org/10.1029/2000GB001380.

Gustafsson, Ö., Haghseta, F., Chan, C., MacFarlane, J., & Gschwend, P. M. (1997). Quantification of the dilute sedimentary soot phase: implications for PAH speciation and bioavailability. Environmental Science & Technology, 31, 203-209. https://doi.org/10.1021/es960317s.

Hockaday, W. C., Grannas, A. M., Kim, S., Hatcher, P. G. (2007). The transformation and mobility of charcoal in a fire-impacted watershed. *Geochimica et Cosmochimica Acta*, 71, 3432-3445. https://doi.org/10.1016/j.gca.2007.02.023.

Hofman, J., Samson, R., Joosen, S., Blust, R., & Lenaerts, S. (2018). Cyclist exposure to black carbon, ultrafine particles and heavy metals: An experimental study along two commuting routes near Antwerp, Belgium. *Environmental Research*, 164, 530-538. https://doi.org/10.1016/j.envres.2018.03.004.

ISO, 1995. Soil quality, determination of carbonate content - Volumetric method, ISO 10693.

IUSS Working Group WRB (2022). World Reference Base for Soil Resources: International soil classification system for naming soils and creating legends for soil maps (4th ed.). International Union of Soil Sciences (IUSS).

Jobbágy, E. G., & Jackson, R. B. (2000). The vertical distribution of soil organic carbon and its relation to climate and vegetation. *Ecological Applications*, 10(2), 423-436. https://doi.org/10.1890/1051-0761(2000)010[0423:TVDOSO]2.0.CO;2.

Kögel-Knabner, I., Guggenberger, G., Kleber, M., Kandeler, E., Kalbitz, K., Scheu, S., Eusterhues, K., & Leinweber, P. (2008). Organo-mineral associations in temperate soils: Integrating biology, mineralogy, and organic matter chemistry. *Journal of Plant Nutrition and Soil Science*, 171(1), 61-82. https://doi.org/10.1002/jpln.200700048.

Lehmann, J., & Kleber, M. (2015). The contentious nature of soil organic matter. *Nature*, 528, 60-68. https://doi.org/10.1038/nature16069.

Lehndorff, E., Roth, P. J., Cao, Z. H., & Amelung, W. (2014). Black carbon accrual during 2000 years of paddy-rice and non-paddy cropping in the Yangtze River Delta, China. *Global Change Biology*, 20(6), 1968-1978. https://doi.org/10.1111/gcb.12468.

Llorente, M., Glaser, B., & Turrión, M. B. (2010). Storage of organic carbon and Black carbon in density fractions of calcareous soils under different land uses. *Geoderma*, 159(1-2), 31-38. https://doi.org/10.1016/j.geoderma.2010.06.011.

Lorenz, K., & Lal, R. (2018). Carbon sequestration in urban ecosystem. *Springer*. https://doi.org/10.1007/978-94-007-2366-5.

Lutfalla, S., Abiven, S., Barré, P., Wiedemeier, D. B., Christensen, B. T., Hout, S., Kätterer, T., Macdonald, A. J., van Oort, F., & Chenu, C. (2017). Pyrogenic carbon lacks long-term persistence in temperate arable soils. *Frontiers in Earth Science*, 5, 96. https://doi.org/10.3389/feart.2017.00096.

Major, J., Lehmann, J., Rondon, M., Goodale, C. (2010). Fate of soil-applied black carbon: Downward migration, leaching and soil respiration. Global Change Biology, 16(4), 1366-1379. https://doi.org/10.1111/j.1365-2486.2009.02044.x.

Masiello, C. A. (2004). New directions in black carbon organic geochemistry. *Marine Chemistry*, 92(1-4), 201-213. https://doi.org/10.1016/j.marchem.2004.06.043.

Nam, J. J., Gustafsson, Ö., Kurt-Karakus, P., Breivik, K., Steinnes, E., & Jones, K. C. (2008). Relationships between organic matter, black carbon and persistent organic pollutants in European background soils: Implications for sources and environmental fate. *Environmental Pollution*, 156, 809-817. https://doi.org/10.1016/j.envpol.2008.05.027.

Olsen, S. R., & Dean, L. A. (1965). Phosphorus, Methods of Soil Analysis Part 2, Chemical and Microbiological Properties. Madison, Wisconsin: American Society of Agronomy, Inc.

Poeplau, C., Dechow, R., Begill, N., & Don, A. (2024). Towards an ecosystem capacity to stabilise organic carbon in soils. Global Change Biology, 30(8), e17453. https://doi.org/10.1111/gcb.17453.

Ponette-González, A. G., Chen, D., Elderbrock, E., Rindy, J. E., Barrett, T. E., Luce, B. W., Lee, J. H., Ko, Y., & Weathers, K. C. (2022). Urban edge trees: Urban form and meteorology drive elemental carbon deposition to canopies and soils. *Environmental Pollution*, 314, 120197. https://doi.org/10.1016/j.envpol.2022.120197.

R Core Team (2025) R: A Language and Environment for Statistical Computing. *R Foundation for Statistical Computing*. https://www.r-project.org/.

Reisser, M., Purves, R. S., Schmidt, M. W. I., Abiven, S. (2016). Pyrogenic carbon in soils: A literature-based inventory and a global estimation of its content in soils. *Frontiers in Earth Science*, 4, 80. https://doi.org/10.3389/feart.2016.00080.

Santín, C., Doerr, S. H., Preston, C. M., & González-Rodríguez, G. (2015). Pyrogenic organic matter production from wildfires: a missing sink in the global carbon cycle. *Global Change Biology*, 21, 1621-1633. https://doi.org/10.1111/gcb.12800.

Schifman, L. A., Prues, A., Gilkey, K., & Shuster, W. D. (2018) Realizing the opportunities of black carbon in urban soils: Implications for water quality management with green infrastructure. Science of Total Environment; 644, 1027-1035. https://doi.org/10.1016/j.scitotenv.2018.06.396.

Schmidt, M. W. I., Skjemstad, J. O., Czimczik, C. I., Glaser, B., Prentice, K. M., Gelinas, Y., & Kuhlbusch, T. A. J. (2001). Comparative analysis of black carbon in soils. *Global Biogeochemical Cycles*, 15(1), 163-167. https://doi.org/10.1029%2F2000GB001284.

Wang, J., Xiong, Z., Kuzyakov, Y. (2016). Biochar stability in soil: Meta-analysis of decomposition and priming effects. *GCB Bioenergy*, 8(3), 512-523. https://doi.org/10.1111/gcbb.12266.

Wang, X. S. (2010). Black carbon in urban topsoils of Xuzhou (China): environmental implication and magnetic proxy. *Environmental Monitoring and Assessment*, 163, 41-47 (2010). https://doi.org/10.1007/s10661-009-0814-z.

Zanella, A., Jabiol, B., Ponge, J. F., Sartori, G., De Waal, R., Van Delft, B., Graefe, U., Cools, N., Katzensteiner, K., Hager, H., & Englisch, M. (2011). A European morpho-functional classification of humus forms. *Geoderma*, 164(3-4), 138-145. https://doi.org/10.1016/j.geoderma.2011.05.016.

Appendix

Tables A1-A8.

Table A1. Characteristics of the 83 sampled forested sites (PPf, SUF and W). For each plot, site name, geographic coordinates (latitude and longitude), green area typology (reported both in full and as acronyms) and site age are provided.

Plot ID	site	Latitude N	Longitude E	green area	age
Bosco della Besozza	BB-01	45.4694	9.3195	forested Periurban Park - PPf	25
	BB-02	45.4712	9.3208		
Bosco di Cusago	BC-01	45.4501	9.0062	Woodland - W	>150
	BC-02	45.4479	9.0069		
	BC-03	45.4481	9.0099		
	BC-04	45.4497	9.0088		
Bosco del Fontanone	BF-01	45.5339	9.3173	forested Periurban Park - PPf	55
	BF-02	45.5315	9.3181		45
	BF-03	45.5328	9.3197		50
	BF-04	45.5337	9.3191		35
Bosco di Montorfano	BM-01	45.3661	9.3259	forested Periurban Park - PPf	18
	BM-02	45.3658	9.3280		18
	BM-03	45.3638	9.3293		28
	BM-04	45.3637	9.3288		27
	BM-05	45.3633	9.3279		27
Bosco delle Noci	BN-01	45.3538	9.3157	forested Periurban Park - PPf	31
	BN-02	45.3532	9.3156		31
	BN-03	45.3530	9.3168		22
	BN-04	45.3518	9.3184		22
	BN-05	45.3517	9.3185		22
	BN-06	45.3523	9.3174		22
Bosco di Riazzolo	BR-01	45.4397	8.95554	Woodland - W	>150
	BR-02	45.4391	8.9587		
	BR-03	45.4387	8.9573		
	BR-04	45.4391	8.9609		
	BR-05	45.4407	8.9632		
	BR-06	45.4406	8.9620		
Bosco del Carengione	CA-01	45.4459	9.3081	forested Periurban Park - PPf	18
	CA-02	45.4449	9.3093		45
	CA-03	45.4466	9.3098		25
	CA-04	45.4468	9.3087		25
Bosco della Chiesa	CH-01	45.4446	8.9536	Woodland - W	>150
	CH-02	45.4462	8.9532		
Boscoincittà	CT-01	45.4881	9.0849	forested Periurban Park - PPf	51
	CT-02	45.4889	9.0846		
	CT-03	45.4877	9.0878		
	CT-04	45.4857	9.0941		
	CM-37	45.4885	9.0852		

Table A1. (continue).

Plot ID	site	Latitude N	Longitude E	green area	age
Boscoincittà	CM-38	45.4860	9.0906	forested Periurban Park - PPf	51
	CM-39	45.4838	9.0935		
	CM-54	45.4843	9.0962		
	CM-55	45.4856	9.0942		
Bosco ex maneggio	EM-01	45.4062	9.2820	forested Periurban Park - PPf	27
	EM-02	45.4055	9.2827		
	EM-03	45.4059	9.2823		
	EM-04	45.4051	9.2827		
La Goccia	LG-01	45.5042	9.1493	Spontaneous Urban Forest - SUF	50
	LG-02	45.5079	9.1523		37
	LG-04	45.5093	9.1517		21
Oasi del Municipio SGM	MS-01	45.4017	9.2842	forested Periurban Park - PPf	22
	MS-02	45.4022	9.2842		22
	MS-03	45.4018	9.2837		22
	MS-04	45.4020	9.2836		22
	MS-05	45.4017	9.2850		28
	MS-06	45.4011	9.2857		10
Parco Natura	NA-01	45.4437	9.0814	forested Periurban Park - PPf	17
	NA-02	45.4459	9.0832		
Parco delle Cave	PC-01	45.4691	9.1041	forested Periurban Park - PPf	15
	PC-02	45.4660	9.1066		28
	PC-03	45.4736	9.1016		27
	PC-04	45.4697	9.0942		89
Parco Nord Milano	PN-01	45.5271	9.1996	forested Periurban Park - PPf	25
	PN-02	45.5290	9.2060		33
	PN-03	45.5296	9.2117		38
	PN-04	45.5294	9.1988		27
	PN-05	45.5405	9.2098		34
	PN-06	45.5417	9.2122		41
	PN-07	45.5430	9.2123		42
	PN-08	45.5456	9.2080		30
	PN-09	45.5448	9.2108		42
	PN-10	45.5273	9.1986		18
	PN-11	45.5260	9.2012		18
	PN-12	45.5244	9.1997		18
	CM-13	45.5451	9.2106		42
	CM-14	45.5417	9.2121		41
	CM-15	45.5291	9.2059		33
	CM-19	45.5406	9.2093		34
Parco della Vita	PV-01	45.4360	9.0769	forested Periurban Park - PPf	37
Testa del Fontanile	TF-01	45.4054	9.2810	forested Periurban Park - PPf	35
	TF-02	45.4056	9.2811		
Oasi di Vanzago	VA-01	45.5225	8.9772	Woodland - W	89
	VA-02	45.5255	8.9765		18
Viale Berbera	VB-01	45.5212	9.2047	forested Periurban Park - PPf	16

Table A2. Characteristics of the 51 sampled non-forested sites (PP, UGI, UP and UPC). For each plot, site name, geographic coordinates (latitude and longitude) and green area typology (reported both in full and as acronyms) are provided.

Plot ID	site	Latitude N	Longitude E	green area
Boscoincittà	CM-34	45.4873	9.0865	Periurban Park - PP
	CM-35	45.4845	9.0930	
	CM-36	45.4839	9.0946	
Collina dei Ciliegi	CM-01	45.5128	9.2091	Urban Park - UP
Giardini della Guastalla	CM-08	45.4602	9.1973	Central Urban Park - UPC
Giardini Montanelli	CM-02	45.4736	9.2007	Central Urban Park - UPC
	CM-03	45.4748	9.2017	
	CM-04	45.4738	9.1993	
Monte Stella	CM-31	45.4887	9.1365	Urban Park - UP
	CM-32	45.4895	9.1341	
	CM-33	45.4908	9.1315	
P.le Cimitero Monumentale	CM-45	45.4845	9.1786	Urban Green Infrastructures - UGI
P.le Damiano Chiesa	CM-44	45.4842	9.1564	Urban Green Infrastructures - UGI
P.le Istria	CM-60	45.5017	9.1985	Urban Green Infrastructures - UGI
P.le Siena	CM-59	45.4654	9.1367	Urban Green Infrastructures - UGI
P.le Susa	CM-52	45.4678	9.2244	Urban Green Infrastructures - UGI
P.zza Ascoli	CM-47	45.4733	9.2177	Urban Green Infrastructures - UGI
P.zza Leonardo da Vinci	CM-46	45.4784	9.2261	Urban Green Infrastructures - UGI
Parco delle Basiliche	CM-09	45.4568	9.1824	Central Urban Park - UPC
Parco delle Cave	CM-25	45.4659	9.1021	Periurban Park - PP
	CM-26	45.4617	9.0997	
	CM-27	45.4671	9.0959	
	CM-28	45.4730	9.1002	
Parco Forlanini	CM-23	45.4658	9.2672	Periurban Park - PP
	CM-24	45.4636	9.2627	
	CM-51	45.4660	9.2615	

Table A2. (continue).

Plot ID	site	Latitude N	Longitude E	green area
Parco Formentano	CM-29	45.4600	9.2147	Urban Park - UP
	CM-30	45.4618	9.2163	
Parco Lambro	CM-20	45.4926	9.2481	Periurban Park - PP
	CM-21	45.4951	9.2434	
	CM-22	45.4934	9.2429	
Parco Martesana	CM-42	45.5029	9.2313	Urban Park - UP
	CM-43	45.5012	9.2322	
Parco Nord Milano	CM-10	45.5467	9.2070	Periurban Park - PP
	CM-11	45.5452	9.2086	
	CM-12	45.5396	9.2087	
	CM-16	45.5242	9.1885	
	CM-18	45.5225	9.1825	
Parco Ravizza	CM-40	45.4469	9.1920	Urban Park - UP
	CM-41	45.4478	9.1939	
Parco Sempione	CM-05	45.4720	9.1772	Central Urban Park - UPC
	CM-06	45.4753	9.1762	
	CM-07	45.4739	9.1747	
Piazzale Lodi	CM-50	45.4475	9.2103	Urban Green Infrastructures - UGI
Porto di Mare	CM-56	45.4322	9.2342	Periurban Park - PP
	CM-57	45.4275	9.2370	
	CM-58	45.4241	9.2360	
Rotonda della Besana	CM-48	45.4599	9.2049	Central Urban Park - UPC
Via Emanueli	CM-53	45.5141	9.2089	Urban Green Infrastructures - UGI
Via Polvani	CM-17	45.5127	9.2112	Urban Green Infrastructures - UGI
Villa Belgiojoso	CM-49	45.4720	9.1987	Central Urban Park - UPC

Table A3. Descriptive statistics of soil properties at different depths (0-10 cm, 10-20 cm, and 20-40 cm). Reported values include sample size (n), mean, standard deviation (SD), coefficient of variation (CV %), minimum (min), and maximum (max) for each variable. Variables comprise pH, soil organic carbon (SOC), total nitrogen (N), SOC:N ratio, calcium carbonate ($CaCO_3$), available phosphorus (avP), and texture fractions (sand, silt, clay).

variable	depth	n	mean	SD	CV %	min	max
pH	0-10	134	5.74	0.88	15.27	3.8	7.7
	10-20	134	5.76	1.01	17.60	3.8	7.9
	20-40	131	5.92	1.10	18.56	3.9	8.0
SOC g kg^{-1}	0-10	134	34.91	15.84	45.37	14.9	91.9
	10-20	134	19.00	6.57	34.60	6.3	35.7
	20-40	131	12.84	4.56	35.52	3.0	28.2
N g kg^{-1}	0-10	134	3.11	1.28	41.31	1.1	7.0
	10-20	134	1.80	0.56	30.89	0.4	3.4
	20-40	131	1.28	0.45	35.26	0.4	2.8
SOC:N ratio	0-10	134	11.18	1.27	11.36	9.2	18.4
	10-20	134	10.53	1.44	13.70	6.8	16.6
	20-40	131	10.09	1.73	17.20	5.3	18.2
$CaCO_3$ g kg^{-1}	0-10	134	2.1	10.3	481.32	0	89
	10-20	134	3.3	13.7	418.74	0	106
	20-40	131	5.9	17.0	288.15	0	103
avP mg kg^{-1}	0-10	134	27.0	18.9	69.82	8.7	127.4
	10-20	74	18.2	8.6	47.19	7.1	54.2
	20-40	73	15.0	8.8	58.82	2.9	55.7
Sand g kg^{-1}	0-10	134	510.1	101.4	19.88	198	817
	10-20	134	499.7	107.6	21.54	154	786
	20-40	131	519.4	112.1	21.58	153	852
Silt g kg^{-1}	0-10	134	394.4	104.3	26.44	53	633
	10-20	134	391.0	99.4	25.42	76	628
	20-40	131	372.1	102.5	27.54	109	623
Clay g kg^{-1}	0-10	134	95.5	49.2	51.50	17	380
	10-20	134	109.3	49.8	45.59	24	345
	20-40	131	108.5	45.5	41.90	16	355

Table A4. Soil organic carbon (SOC), pyrogenic carbon (PyC), and PyC:SOC ratio across soil depth layers. Values are reported as mean ± standard deviation. Minimum and maximum values are shown in parentheses. Data refer to mineral soil layers at 0-10, 10-20, and 20-40 cm depth.

Depth (cm)	SOC (g kg^{-1})	PyC (g kg^{-1})	PyC:SOC (%)
0-10	34.9 ± 15.8 (14.9-91.9)	4.34 ± 5.18 (0.74-24.39)	10.36 ± 6.42 (2.96-30.94)
10-20	19.0 ± 6.6 (6.3-35.7)	2.14 ± 1.50 (0.51-7.32)	11.19 ± 5.89 (2.47-31.56)
20-40	12.8 ± 4.6 (3.0-28.2)	1.29 ± 0.76 (0.28-4.34)	10.68 ± 5.73 (2.50-29.37)

Table A5. Effects of soil depth on absolute and relative SOC and PyC fractions based on linear mixed-effects models. Estimated marginal means (EMM) ± standard error (SE) are reported.

Variable	Depth (cm)	EMM	SE	Group
SOC_POM (g kg^{-1})	0-10	2.35	0.09	a
	10-20	1.30	0.09	b
SOC_MAOM (g kg^{-1})	0-10	1.14	0.03	a
	10-20	0.60	0.03	b
PyC_POM (g kg^{-1})	0-10	0.22	0.01	a
	10-20	0.11	0.01	b
PyC_MAOM (g kg^{-1})	0-10	0.21	0.02	a
	10-20	0.10	0.02	b
SOC_POM (%)	0-10	65.52	0.97	b
	10-20	67.32	0.97	a
SOC_MAOM (%)	0-10	34.48	0.97	a
	10-20	32.68	0.97	b
PyC_POM (%)	0-10	57.03	1.08	a
	10-20	55.76	1.08	a
PyC_MAOM (%)	0-10	42.97	1.08	a
	10-20	44.24	1.08	a
PyC:SOC (POM)	0-10	8.78	0.44	a
	10-20	9.20	0.44	a
PyC:SOC (MAOM)	0-10	17.45	1.70	a
	10-20	18.16	1.70	a

Note: different letters indicate statistically significant differences between depths ($p < 0.05$). Depth effects were significant for absolute SOC and PyC fractions and for SOC relative distribution ($p < 0.05$), but not for PyC relative distribution or PyC:SOC ratios ($p > 0.05$).

Table A6. Effects of urban concentric zones on indices describing PyC stabilization pathways in surface (0-10 cm) and subsurface (10-20 cm) soils. Estimated marginal means (EMMs) ± standard error (SE) are reported.

Variable	Depth (cm)	Urban zone	EMM ±SE	Group	*p* (urban zone)
PyC POM:MAOM ratio	0-10	Inner	2.60 ± 0.52	a	0.358
		Intermediate	1.84 ± 0.22	a	
		Outer	1.57 ± 0.36	a	
	10-20	Inner	1.37 ± 0.32	a	0.513
		Intermediate	1.35 ± 0.14	a	
		Outer	1.64 ± 0.22	a	
MAOM-associated PyC (%)	0-10	Inner	35.70 ± 5.65	a	0.605
		Intermediate	40.84 ± 2.40	a	
		Outer	43.45 ± 3.82	a	
	10-20	Inner	44.42 ± 4.23	a	0.612
		Intermediate	44.82 ± 1.76	a	
		Outer	41.71 ± 2.78	a	

Notes: different letters indicate statistically significant differences among urban zones ($p < 0.05$, Tukey-adjusted pairwise comparisons). For all variables, the effect of urban zone was not statistically significant ($p > 0.3$), indicating comparable PyC partitioning between particulate and mineral-associated pools across concentric urban zones.

Table A7. Significance groups for soil parameters across green area categories (age-stratified) obtained from non-parametric analyses. Groups are based on Kruskal-Wallis tests followed by pairwise Wilcoxon comparisons with Benjamini-Hochberg adjustment. Estimated marginal means and standard errors are not applicable and therefore not reported.

Parameter	PP	PPfy	PPfm	PPfo	UGI	UP	UPC	SUF	W
PyC1	c	b	ab	a	c	c	c	cd	d
PyC3	ce	ab	a	bc	d	de	de	de	de
SOC_POM1	abc	abcd	ab	ac	bd	abcd	c	d	e
PyC_POM1	cd	a	a	b	c	cd	d	ce	e
PyC_MAOM1	e	ab	a	abc	abcd	de	cde	bcde	f
PyC_MAOM2	bc	a	a	b	bc	c	c	cd	d
PyC:SOC1 ratio	ce	ab	a	bc	d	de	de	de	de
PyC:SOC3 ratio	cde	a	a	b	cd	cd	c	d	be
PyC_POM:MAOM1 ratio	ab	ab	a	ab	c	ab	ab	bc	d

Table A8. Total pyrogenic carbon content (PyC_total) and proportion of mineral-associated pyrogenic carbon (PyC_MAOM share) in surface and subsurface soils (0-10 and 10-20 cm) across green area categories. Values are reported as mean ± standard deviation, with minimum and maximum values shown in parentheses. PyC_MAOM share (%) represents the fraction of total PyC associated with the mineral-associated organic matter pool.

Green area	Depth (cm)	n	PyC_total (g kg^{-1})	PyC_MAOM share (%)
PP	0-10	21	3.65 ± 1.95 (1.53-8.94)	44.68 ± 15.66 (11.87-69.46)
	10-20	21	2.38 ± 1.22 (1.04-4.43)	42.95 ± 13.13 (17.38-71.09)
PPfy	0-10	11	1.57 ± 1.29 (0.74-4.80)	40.24 ± 9.67 (16.89-49.04)
	10-20	11	1.08 ± 0.37 (0.56-1.62)	37.38 ± 7.40 (27.12-49.65)
PPfm	0-10	36	1.62 ± 0.72 (0.83-3.43)	43.70 ± 8.93 (25.27-65.72)
	10-20	36	1.00 ± 0.46 (0.51-3.10)	42.14 ± 9.52 (21.57-63.95)
PPfo	0-10	19	2.04 ± 0.92 (1.14-4.15)	44.48 ± 15.55 (21.35-76.45)
	10-20	19	1.55 ± 0.62 (0.81-2.85)	44.65 ± 7.51 (29.89-60.65)
UGI	0-10	10	3.80 ± 0.96 (2.45-5.30)	25.73 ± 12.64 (14.64-55.80)
	10-20	10	2.50 ± 1.01 (0.86-4.13)	37.41 ± 8.72 (21.69-51.16)
UP	0-10	10	4.20 ± 1.28 (2.48-6.78)	39.43 ± 10.58 (19.30-55.21)
	10-20	10	2.64 ± 1.22 (1.53-4.88)	45.42 ± 5.66 (37.58-56.11)
UPC	0-10	10	3.61 ± 0.67 (2.76-4.98)	38.28 ± 9.64 (27.72-54.93)
	10-20	10	2.54 ± 0.45 (2.04-3.26)	43.09 ± 6.11 (32.84-52.22)
SUF	0-10	3	9.55 ± 6.88 (3.41-16.98)	25.68 ± 3.18 (22.03-27.88)
	10-20	3	5.07 ± 1.88 (3.29-7.03)	37.93 ± 6.87 (31.61-45.23)
W	0-10	14	17.56 ± 5.00 (8.78-24.39)	60.50 ± 4.77 (53.22-68.64)
	10-20	14	4.78 ± 1.42 (2.65-7.32)	62.72 ± 6.39 (52.33-74.18)

Chapter 3.
Methodological insights from Parco Nord Milano: PyC Chemo-Thermal-Oxidation (CTO-360) vs Chemical Oxidation (CO)

This chapter addresses methodological uncertainty in pyrogenic carbon quantification by comparing chemo-thermal oxidation (CTO-360) and chemical oxidation approaches applied to the same soil samples. It evaluates the consistency and divergence between methods across soil depths and explores how analytical choices influence the interpretation of PyC pools. The chapter also examines relationships between PyC, soil properties, and trace metals, contributing to a more robust understanding of carbon dynamics in urban soils.

1. Introduction

Pyrogenic carbon (PyC) comprises a wide continuum of carbonaceous materials formed during the incomplete combustion of biomass and fossil fuels. This continuum spans from lightly charred organic matter to highly graphitized soot, differing in aromaticity, molecular structure, and resistance to decomposition (Masiello, 2004). As extensively demonstrated by Kuhlbusch & Crutzen (1995) and later confirmed by Kuhlbusch (1999), PyC represents one of the most persistent components of the global carbon cycle, with degradation timescales extending from centuries to geological times. Its persistence in soils and sediments is supported by multiple lines of evidence, including the long-term preservation of charcoal particles in sediment cores (Herring, 1985) and the high resistance of condensed aromatic structures to microbial and abiotic oxidation (Glaser *et al.*, 2000). Recent global syntheses have emphasized the importance of PyC in Earth system functioning, highlighting its role in long-term carbon sequestration, biogeochemical cycling, and interactions with hydrological processes (Bird *et al.*, 2015; Masiello & Berhe, 2020). Moreover, archaeological and paleoecological records suggest that anthropogenic fire regimes have influenced PyC production for millennia (Bird *et al.*, 2024).

Accurate quantification of PyC is essential to assess its role in soil carbon stocks, carbon-cycle feedbacks, and environmental pollutant dynamics. However, measuring PyC remains challenging because it is not a single compound, but a thermochemically diverse continuum (Masiello, 2004). Consequently, reported PyC concentrations vary widely among analytical methods, with discrepancies that may reach one or two orders of magnitude (Schmidt *et al.*, 2001; Hammes *et al.*, 2007). The methodological uncertainty is especially problematic in heterogeneous matrices such as urban and peri-urban soils, where PyC derives from mixed biomass-burning and fossil-fuel sources, including diesel soot, industrial emissions, and particulate deposition (Hofman *et al.*, 2018; Liu *et al.*, 2019). These complex inputs are particularly relevant in rapidly urbanizing regions and heavily industrialized areas, where PyC accumulation may be accompanied by co-occurrence of trace metals, polycyclic aromatic hydrocarbons (PAHs), and technogenic particles (Liu *et al.*, 2019). Increasing global awareness of the climatic and health impacts of black carbon emissions further underscores the need for reliable PyC quantification (Ren *et al.*, 2025).

A wide range of analytical methods has been developed to quantify PyC in soils and sediments, each targeting a distinct operational portion of the combustion continuum (Hammes *et al.*, 2007; Xie *et al.*, 2024). Among these, thermo-oxidative and chemical oxidation approaches remain the most widely applied in environmental studies. The chemo-thermal oxidation protocol at 375 °C (CTO-375), originally introduced by Gustafsson *et al.* (1997) and refined in Gustafsson *et al.* (2001), selectively isolates highly condensed soot-like fractions through controlled thermal oxidation following acid pretreatment. Elmquist *et al.* (2004) further demonstrated the sensitivity of CTO recoveries to temperature, showing that lowering oxidation temperature to ~360 °C can reduce co-oxidation of non-pyrogenic organic matter and improve soot selectivity in some matrices, particularly those affected by catalytic mineral phases. In contrast, the chemical oxidation (CO) method, based on dichromate-sulfuric oxidation after HF treatment, targets a broader though less specific portion of the PyC continuum (Hammes *et al.*, 2007). CO often yields higher PyC recoveries but may include chemically resistant

organic matter unrelated to combustion, thus inflating PyC estimates in certain soils (Masiello, 2004; Xie *et al.*, 2024). Because of their conceptual complementarity, CTO and CO target different PyC fractions and therefore rarely isolate the same material; their relative performance depends strongly on environmental context and matrix composition.

Comparative evaluations of CTO and CO have been mostly restricted to sediments or agricultural soils (Hammes *et al.*, 2007; Elmquist *et al.*, 2004), with limited applications to urban and industrial contexts. Yet, urban soils exhibit distinctive combinations of natural PyC, fossil-fuel soot, atmospheric deposition, and technogenic particles, alongside elevated concentrations of metals and pollutants (Hofman *et al.*, 2018; Liu *et al.*, 2019). These factors may alter the thermal stability or chemical resistance of PyC, potentially biasing standard CTO-375 and CO protocols. Moreover, the vertical distribution of PyC in young urban forest soils remains understudied, despite evidence that both natural and anthropogenic PyC can undergo downward transport, accumulate in surface horizons, or become stabilized within mineral-associated fractions (Santín *et al.*, 2015b; Bird *et al.*, 2015). Few studies have assessed how PyC quantification responds to soil depth or how method-derived PyC concentrations relate to key soil properties such as soil organic carbon (SOC), total nitrogen (N), pH, texture, or pedogenic development.

Within this framework, the present study addresses these gaps by performing a systematic comparison of CTO and CO methods on peri-urban forest soils within the Metropolitan City of Milan. We employ a modified version of the CTO protocol, lowering the oxidation temperature from 375 °C to 360 °C to enhance method selectivity, consistent with evidence from Elmquist *et al.* (2004) regarding thermal thresholds for soot preservation. PyC was quantified across three depths (0-10, 10-20, and 20-40 cm) to capture vertical trends and evaluate depth-dependent sensitivity of each method. Beyond a purely methodological comparison, we integrate PyC estimates with soil physicochemical properties, including SOC, N, pH, and texture, and with ecological indicators such as forest stand age and land-use history. This combined pedological-ecological perspective allows us to assess whether CTO and CO respond differently to soil traits, vegetation development, and urban environmental conditions.

Overall, this work provides new insight into how methodological choices influence PyC quantification in complex urban soils and clarifies the extent to which CTO and CO capture distinct components of the PyC continuum along depth and environmental gradients. By sitting in the methodological comparison within a broader ecological and pedological framework, this study contributes to improving PyC assessment in heterogeneous and human-impacted landscapes.

2. Materials and Methods

2.1. Study sites and sampling design

The study, conducted in 8 forested sites located within Parco Nord Milano (northern Milan, Italy: 45.5378 N; 9.2094 E) (Fig. 2.1), a peri-urban park characterized by mixed broadleaved stands established on former agricultural land, is part of a broader research project on PyC dynamics and its physical fractionation (POM-MAOM) across the entire Metropolitan City of Milan (see *Chapter 2. "PyC distribution across the Metropolitan City of Milan"*).

Fig. 2.1. Study area and location of the 8 sampling sites in the Parco Nord (PN).

The Metropolitan City of Milan is characterized by a continental climate, with annual precipitation of approximately 920-940 mm and average minimum and maximum daily temperatures of 8 °C and 17 °C, respectively. In the Milan region, natural soils are mainly *Luvisols* and *Cambisols* formed on alluvial deposits, with local *Fluvisols*, *Umbrisols* and *Gleysols*, according to the World Reference Base for Soil Resources (IUSS Working Group WRB, 2022). In urbanized sectors, natural patterns are largely replaced by *Technosols* due to prolonged human disturbance and the incorporation of anthropogenic materials.

The study area encompasses both recently afforested stands and older forest patches (aged from 25 to 42 years) established on former agricultural land, with vegetation dominated by *Acer spp.* (*A. campestre* and *A.*

platanoides), *Celtis australis*, *Fraxinus spp.* (*F. ornus* and *F. oxicarpa*), *Quercus spp.* (*Q. cerris*, *Q. robur* and *Q. rubra*), and mixed shrub-herbaceous communities.

Eight forest plots were selected along a north-south transect crossing the park, covering a distance of ~2 km. The northern plots (from PN-05 to PN-08) lie within 1 km of the A4 motorway, while the southern plots (from PN-01 to PN-04) are more distant (>1 km), allowing assessment of the potential imprint of historical vehicular emissions. The A4 urban stretch is one of the busiest motorway segments in the Milan area, with frequent congestion and a high proportion of heavy-duty vehicles. Distance from this road was therefore used as a simple proxy for long-term exposure to traffic-related deposition of PyC and associated trace metals, allowing us to test whether plots closer to the motorway show enhanced PyC and metal contents compared with the more distal southern plots.

Soil sampling was conducted in June 2024 using a gouge auger (Eijkelkamp, 2.5 cm diameter). For each site, three sampling points were selected in a triangular layout, each 2 m from the georeferenced center. From each point, soil samples were taken from three mineral soil layers (0-10 cm, 10-20 cm, and 20-40 cm) and combined to form one composite sample per layer.

Table 2.1 shows the characteristics of each of the 8 sampling sites, with information regarding the geographical coordinates (Latitude N, Longitude E), the forest plantation age and the type of environment.

Tab 2.1. Description of the 8 sampling sites in Parco Nord Milano.

site	Latitude N	Longitude E	age	type of environment
PN-01	45,527144	9,199553	25	closed mixed broadleaf forest (*A. platanoides* and *Q. robur* dominance)
PN-02	45,528962	9,205984	33	closed mixed broadleaf forest (*A. campestre* dominance)
PN-03	45,529613	9,211658	38	open mixed broadleaf forest (*A. campestre* dominance)
PN-04	45,529401	9,198809	27	open mixed broadleaf forest (*A. campestre* and *F. oxicarpa* dominance)
PN-05	45,540462	9,209771	34	semi-open mixed broadleaf forest (*A. campestre* dominance)
PN-06	45,541687	9,212193	41	semi-open mixed broadleaf forest (*C. australis* and *F. ornus* dominance)
PN-07	45,543021	9,212319	42	open mixed broadleaf forest (*Q. cerris* and *Q. rubra* dominance)
PN-08	45,545620	9,208049	30	semi-open mixed broadleaf forest (*A. campestre* and *Q. robur* dominance)

2.2. Laboratory analyses

2.2.1. Soil chemo-physical characterization

Mineral soil samples were air-dried for one week. Aggregates were manually broken with rubber tools, and coarse fragments (e.g., stones, bricks, roots) were removed. The fine earth fraction (< 2 mm) was used for analyses. Sub-samples milled < 0.2 mm were prepared for soil organic carbon (SOC), total nitrogen (N), and PyC analyses (Chemo-Thermal Oxidation CTO-360 and Chemical Oxidation CO methods).

Analytical procedures included: pH in H_2O (1:2.5 soil-to-solution ratio; potentiometric method); total carbonates (Dietrich-Frühling calcimeter; ISO 10693); SOC and N (dry combustion; Flash EA 1112 NCSoil elemental analyzer, Thermo Fisher Scientific, Pittsburgh, PA, USA); available phosphorus (avP) (ascorbic acid method; Olsen & Dean, 1965); texture (pipette method; Day, 1965); pseudototal heavy metals concentrations (chromium, copper, nickel, lead, and zinc: acid digestion, ISO 11466.3; quantification by Flame Atomic Absorption Spectrometry, PinAAcle 500 Flame AAS, PerkinElmer).

2.2.2. PyC quantification methods

For PyC quantification, two complementary analytical methods were applied to the same fine-earth aliquots after acid pre-treatment with 1 M HCl to remove carbonates:

1. Chemo-Thermal Oxidation (CTO-360): subsamples were oven-dried, weighed, and oxidized in a muffle furnace at 360 °C for 18 hours under a 20 % O_2/air mixture. The remaining residue was analyzed for C content by elemental analyzer.
2. Chemical Oxidation (CO): subsamples were treated with 10 % HF and 0.1 M $K_2Cr_2O_7$ / 2 M H_2SO_4 under controlled conditions. The oxidized residues were oven-dried, and analyzed for C content by elemental analyzer.

Both methods were applied to the same set of 24 soil samples, allowing direct comparison of the CTO-360 and CO estimates of PyC. The analytical procedures followed the protocols described in Gustafsson *et al.* (2001), Elmquist *et al.* (2004), Hammes *et al.* (2007), and Santín *et al.* (2017), with minor adaptations for urban soils.

2.3. Data preparation and statistical analyses

All statistical analyses were performed in R (v. 4.5.1) using the *tidyverse*, *ggplot2*, *ggpmisc*, *rstatix*, *FSA*, *emmeans*, *broom*, *readxl*, and *effsize* packages (R Core Team, 2025).

For each sample, non-pyrogenic SOC (SOC_nPyC) was calculated as the difference between SOC and PyC measured with each method:

SOC_nPyC (CTO-360) = SOC − PyC (CTO-360)
SOC_nPyC (CO) SOC − PyC (CO)

where

SOC_nPyC (CTO-360) represents the non-pyrogenic carbon fraction obtained after subtracting the CTO-360-derived PyC, and

SOC_nPyC (CO) corresponds to the same fraction computed using PyC concentrations measured by the CO method.

Depth classes (0-10, 10-20, 20-40 cm) were treated as ordered factors, and a pooled dataset (0-40 cm) was generated by stacking all depth layers (n = 24).

2.3.1 Comparison between PyC determination methods

Paired comparisons between PyC (CTO-360) and PyC (CO) were performed separately for each depth layer using paired *t*-tests when normality (Shapiro-Wilk) was met, and Wilcoxon signed-rank tests otherwise. Normality of residuals was assessed using the Shapiro-Wilk test. Homoscedasticity was evaluated through visual inspection of residual vs fitted plots and Levene's tests when appropriate.

Differences in PyC:SOC (%) were also evaluated analogously.

The paired design accounts for the fact that CTO-360 and CO were applied to the same soil samples by explicitly comparing method-derived PyC estimates within each individual sample. This approach controls for between-sample variability in soil properties (e.g. SOC content, texture, depth, and site-specific characteristics), allowing observed differences to be attributed to the analytical method rather than to intrinsic soil heterogeneity.

The magnitude of statistical relationships was interpreted according to conventional effect size thresholds for correlation coefficients (Cohen, 1988).

2.3.2 Relationships between PyC and SOC

Linear regression models were fitted separately for each PyC determination method (CTO-360 and CO) and for each soil depth interval (0-10, 10-20, and 20-40 cm), using SOC as predictor and PyC concentration as response variable.

Differences in slopes and intercepts between methods were evaluated using Tukey-adjusted pairwise contrasts from the *emmeans* package, after fitting ANCOVA models with SOC as covariate and method as fixed effect.

Depth-related differences in regression parameters were tested by including interaction terms (method × depth) in the ANCOVA framework.

2.3.3 Correlations with soil properties and heavy metals

Pearson's correlations were computed to assess relationships among soil carbon variables (PyC (CTO-360), PyC (CO), PyC:SOC ratios, and SOC_nPyC), general soil properties (SOC, pH, N, avP, texture, SOC:N ratio), and heavy metals (Cr, Cu, Ni, Pb, Zn).

Both CTO-360-based and CO-based SOC_nPyC estimates (as defined in Section 2.3) were included.

Correlation analyses were performed separately for each depth layer (0-10, 10-20, 20-40 cm) and for the pooled 0-40 cm dataset to increase statistical power and evaluate cross-depth patterns.

Correlation coefficients *r* and associated *p*-values were obtained using *Hmisc::rcorr* and retained for reporting in the results.

Correlation matrices were visualized using half-heatmaps to enhance readability.

2.3.4 Assessment of spatial structure along the north-south transect

To explore potential spatial structuring along the north-south transect, latitude was used as a continuous proxy for spatial position relative to the A4 motorway. Exploratory scatterplots were first used to visually inspect

possible trends or discontinuities in SOC, PyC variables, SOC_nPyC, and heavy metal concentrations along the transect.

Where patterns suggested potential spatial differentiation, additional statistical comparisons were conducted to support the descriptive interpretation. These analyses were considered exploratory and are intended to provide contextual information rather than formal hypothesis testing.

3. Results

3.1. PyC concentrations and comparison between analytical methods

Across all samples, both analytical approaches detected measurable amounts of pyrogenic carbon (PyC), although with systematic differences in magnitude between methods (Figure 3.1; Appendix Table A1).

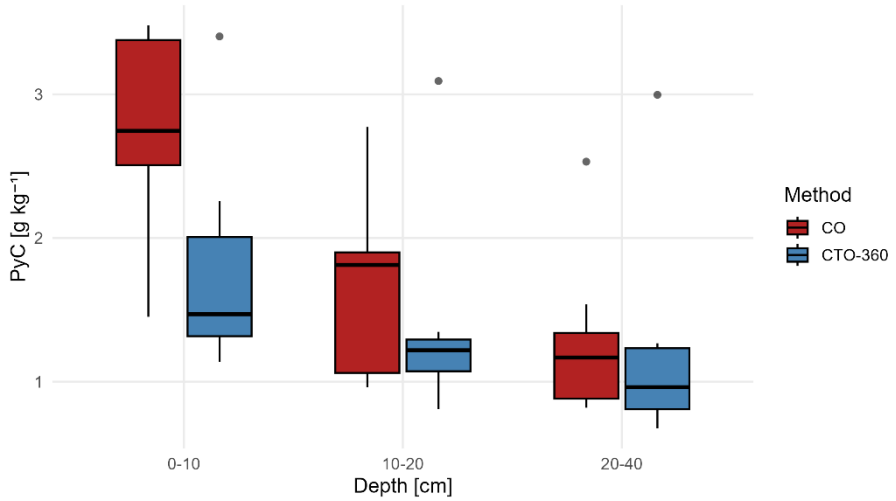

Figure 3.1. Boxplots of pyrogenic carbon (PyC) concentrations (g kg^{-1}) obtained using the chemical oxidation (CO) and chemo-thermal oxidation (CTO-360) methods at three soil depths (0-10, 10-20, and 20-40 cm). Boxes indicate the interquartile range (IQR) with median values, whiskers represent 1.5 × IQR, and dots indicate outliers.

At the surface layer (0-10 cm), mean PyC concentrations obtained by the CO method (2.8 ± 0.7 g kg^{-1}) were markedly higher than those measured using CTO-360 (1.8 ± 0.7 g kg^{-1}), corresponding to an average increase of approximately 55-60%. This difference was statistically significant (paired *t*-test, p = 0.005; Wilcoxon signed-rank test, $p = 0.021$).

In the 10-20 cm layer, PyC concentrations decreased for both methods, with mean values of 1.7 ± 0.6 g kg^{-1} for CO and 1.4 ± 0.7 g kg^{-1} for CTO-360. Although CO still yielded higher PyC concentrations, the inter-method difference was smaller and did not reach statistical significance ($p > 0.05$).

Similarly, in the deepest layer (20-40 cm), mean PyC concentrations converged further (1.3 ± 0.6 g kg^{-1} for CO and 1.2 ± 0.8 g kg^{-1} for CTO-360), with no significant difference between methods ($p > 0.50$).

Considering the entire 0-40 cm depth interval, average PyC concentrations were higher for CO (1.9 ± 0.9 g kg^{-1}) than for CTO-360 (1.5 ± 0.7 g kg^{-1}), and statistically different ($p < 0.001$), confirming a consistent but depth-dependent tendency of the chemical oxidation method to yield higher PyC estimates.

Overall, both methods depicted coherent vertical patterns, with PyC concentrations declining with depth. The stronger divergence observed in surface soils indicates that CO isolates a broader and less refractory fraction of the combustion continuum, whereas CTO-360 selectively targets the most thermally stable PyC pool. Despite differences in absolute concentrations, the parallel depth trends suggest methodological complementarity rather than analytical inconsistency.

3.2. General soil properties

Across the investigated soil layers, clear depth-dependent patterns were observed for the main pedological parameters (Appendix Table A2).

In the 0-10 cm layer, soils were characterized by higher organic matter content, with mean SOC values of 31.5 ± 7.2 g kg^{-1} and total nitrogen of 2.6 ± 0.6 g kg^{-1}. This surface layer also showed the lowest variability for SOC:N ratios (Coefficient of Variation, CV < 7%), indicating relatively homogeneous organic matter composition across sampling points.

In the intermediate layer (10-20 cm), SOC and N contents both decreased markedly (14.5 ± 4.9 and 1.4 ± 0.3 g kg^{-1}, respectively), while SOC:N ratios remained within a comparable range (≈ 10). Variability increased for most chemical parameters, particularly SOC and available phosphorus (CV ≈ 34% and 61% respectively).

In the deepest layer (20-40 cm), SOC and N concentrations further declined to 10.8 ± 4.6 and 1.1 ± 0.3 g kg^{-1}, respectively, whereas SOC:N ratios remained relatively stable (≈ 9-10). This layer displayed the highest coefficients of variation for SOC and available phosphorus (avP) (CV ≈ 42% and 77% respectively), indicating increased variability with depth.

Mean soil pH values were similar across the three investigated depths, with average values ranging between 5.2 and 5.3 (Appendix Table A2), indicating predominantly acidic conditions. Higher pH values were recorded at specific sites, particularly PN-03 (pH ≈ 6.0-6.1) and PN-05, where pH increased with depth and reached near-neutral conditions in the 20-40 cm layer (pH up to 7.3). Despite these site-specific deviations, overall pH variability across depths remained limited, as indicated by relatively low coefficients of variation (≈ 14-18%).

Textural fractions showed limited variability across depths, with low coefficients of variation (< 16%), indicating relatively homogeneous physical conditions among sampling points.

3.3. Relationships between PyC, SOC and soil properties

3.3.1. Pearson correlations across the 0-40 cm depth interval

Across the entire 0-40 cm depth interval, Pearson correlation analysis revealed consistent relationships between PyC, SOC, and selected soil properties (Figure 3.2).

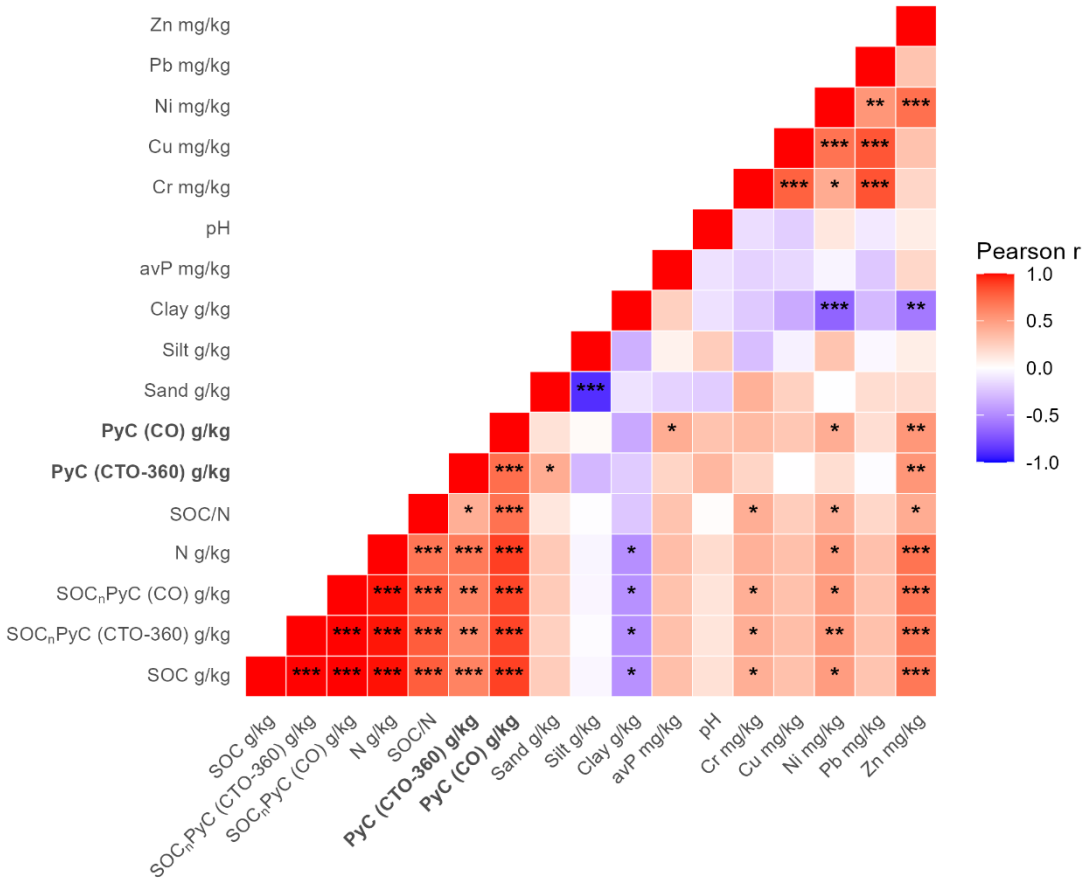

Figure 3.2. Pearson correlation matrix among soil physicochemical parameters (0-40 cm). The color gradient indicates the strength and direction of linear relationships (blue = negative, red = positive). All correlations were computed using pairwise complete observations. Significant correlations are highlighted as follows: *** p < 0.001 | ** p < 0.01 | * p < 0.05.

PyC quantified using the chemical oxidation (CO) method exhibited a strong positive correlation with total SOC ($r = 0.89$, $p < 0.001$), whereas the correlation was weaker for PyC (CTO-360) ($r = 0.63$, $p < 0.001$). This difference highlights the broader operational definition of PyC captured by CO compared to the more selective chemo-thermal oxidation method.

When considering the non-pyrogenic fraction of SOC (SOC_nPyC), significant positive correlations with several trace metals emerged in the pooled dataset. SOC_nPyC derived from both CTO-360 and CO showed positive correlations with Zn ($r \approx 0.67$-0.68, $p < 0.001$), Ni ($r \approx 0.51$-0.52, $p < 0.05$), and Cr (both $r \approx 0.42$, $p < 0.05$), while correlations with Cu and Pb were weak or not significant.

In contrast, PyC itself displayed weaker and less systematic relationships with trace metals, particularly for PyC (CTO-360), whereas moderate associations were observed for PyC (CO) when all depths were considered together.

Strong positive inter-metal correlations were also observed, particularly between Cr and both Cu and Pb ($r = 0.77$-0.83, $p < 0.001$), Cu and Ni-Pb ($r = 0.70$-0.82, $p < 0.001$), Ni and both Zn ($r = 0.71$, $p < 0.001$) and Pb ($r = 0.54$, $p < 0.01$), indicating coherent metal distribution patterns across the investigated sites. Relationships with pH and soil texture were generally weaker or variable.

Depth-specific Pearson correlation matrices (0-10, 10-20 and 20-40 cm) are reported in the Supplementary Materials (Appendix Figures A1-A3) and show overall weaker and less consistent relationships, likely reflecting the reduced sample size within individual soil layers.

This suggests that metal-metal and metal-carbon associations primarily emerge at the whole-depth (0-40 cm) scale, whereas depth-specific analyses are more strongly influenced by local heterogeneity.

Within this framework, the pooled analysis further indicates that metal retention is more closely associated with the non-pyrogenic SOC fraction (SOC_nPyC) than with PyC itself, irrespective of the analytical method used.

3.3.2. Depth-dependent SOC-PyC relationships

Linear regression analyses highlighted depth-dependent relationships between SOC and PyC concentrations, with differences in strength between analytical methods and soil layers (Figure 3.3).

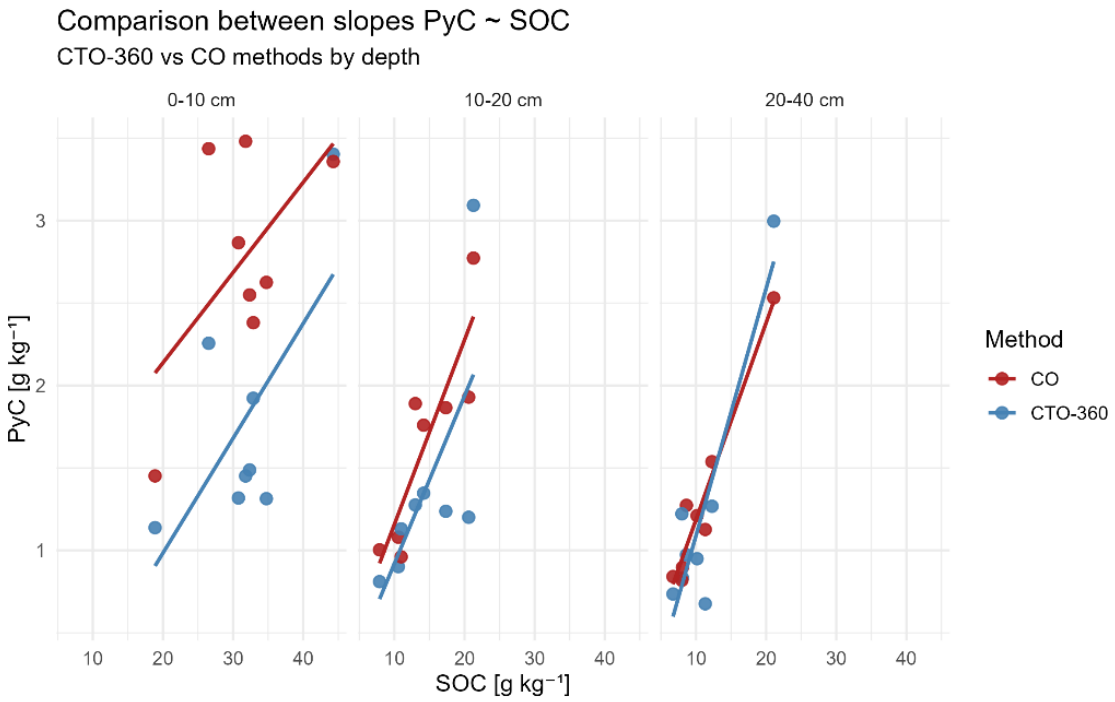

Figure 3.3. Linear regressions between PyC and SOC concentrations (g kg^{-1}) for the CO and CTO-360 methods across the three depth intervals (0-10, 10-20, and 20-40 cm). Regression strength increases with depth for both methods, while the CO approach generally shows higher coefficients of determination (R^2), indicating stronger coupling with SOC variability.

In the surface layer (0-10 cm), positive relationships between SOC and PyC were observed for both analytical methods, although regression slopes were not statistically significant ($p > 0.05$), with moderate coefficients of determination (R^2 = 0.33-0.45).

In the intermediate layer (10-20 cm), the SOC-PyC relationship strengthened, particularly for the CO method, which showed a significant positive regression slope (p = 0.004; R^2 = 0.77). In contrast, the relationship for PyC (CTO-360) was weaker and marginally non-significant (p = 0.059; R^2 = 0.47).

In the deepest layer (20-40 cm), both methods exhibited strong and significant linear relationships between SOC and PyC. The CO method showed the highest explanatory power ($R^2 = 0.94$, $p < 0.001$), while CTO-360 also displayed a strong association ($R^2 = 0.82$, $p = 0.002$).

Overall, regression analyses confirm that SOC-PyC relationships become stronger with depth, while the magnitude of explained variance differs between analytical methods, with CO generally yielding higher coefficients of determination than CTO-360.

3.4. Depth patterns of PyC:SOC ratios

Across the investigated soil depth intervals, PyC:SOC ratios showed a clear depth-dependent pattern for both analytical methods (Figure 3.4). Median PyC:SOC values increased progressively from surface soils (0-10 cm) to subsoil layers (20-40 cm), indicating a relative enrichment of PyC with respect to total SOC at greater depths.

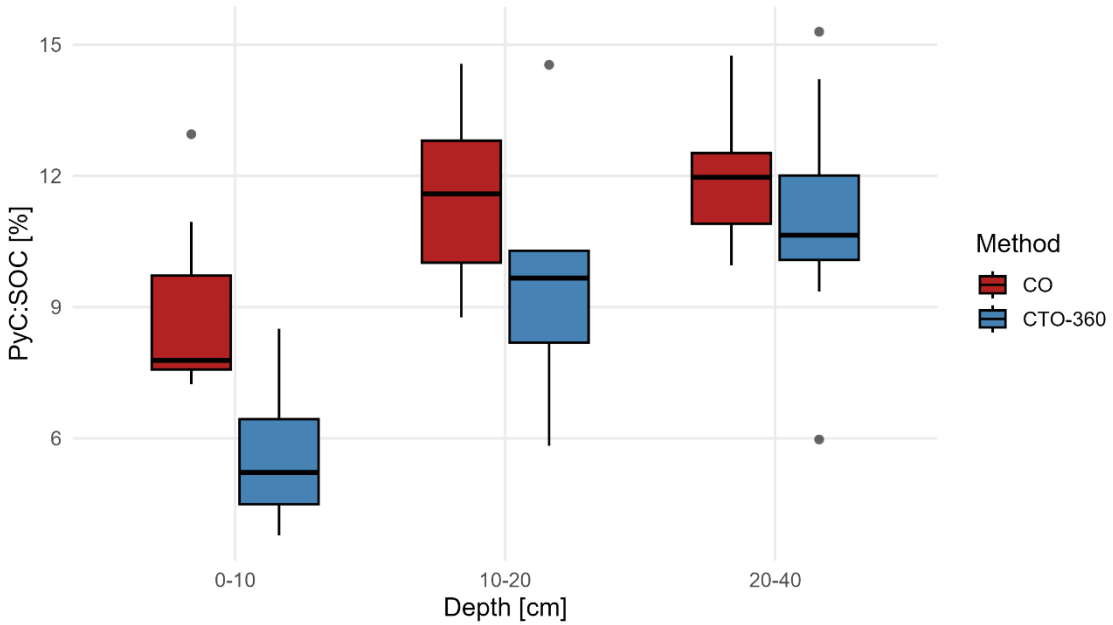

Figure 3.4. Boxplots of the PyC:SOC ratio across soil depths (0-10, 10-20, and 20-40 cm) for the CO and CTO-360 methods. Boxes represent the interquartile range (IQR) with the median as the central line; whiskers extend to 1.5 × IQR, and dots indicate outliers.

For the CO method, mean PyC:SOC ratios increased from 8.9 ± 2.1 % at 0-10 cm to 11.5 ± 2.0 % at 10-20 cm and 11.9 ± 1.5 % at 20-40 cm, while CTO-360 showed consistently lower but comparable depth trends (5.9 ± 1.7 %, 9.5 ± 2.6 %, and 11.0 ± 2.9 %, respectively).

Inter-method differences were depth-dependent. A statistically significant difference between PyC:SOC ratios obtained by CO and CTO-360 was detected only in the 0-10 cm layer (paired *t*-test $p = 0.005$; Wilcoxon signed-rank test, $p = 0.021$), whereas differences were not significant in the 10-20 cm and 20-40 cm layers ($p > 0.05$ for both tests). Despite this, CO consistently yielded higher PyC:SOC ratios across all depths, indicating a coherent but not uniformly significant tendency toward higher estimates compared to CTO-360.

The relative enrichment of PyC with depth reflects a proportional increase of the more refractory carbon pool as total organic carbon declines.

This progressive reduction in the difference between methods with depth is consistent with the boxplot distributions, which show a narrowing of PyC:SOC variability in deeper layers (Figure 3.4). Together, these results indicate that methodological contrasts in PyC quantification are most pronounced in surface soils, whereas relative PyC contributions to SOC become increasingly similar between methods in subsoils.

To further explore method- and depth-specific trends, linear regressions between PyC and SOC concentrations were performed separately for each depth interval. The resulting regression slopes, summarizing the sensitivity of PyC to SOC across depths and methods, are reported in the Supplementary Materials (Appendix Figure A4).

4. Discussion

4.1 Methodological complementarity between CTO-360 and CO

The two analytical methods applied in this study isolate partially overlapping but chemically distinct fractions of PyC continuum. Across all depths, CO consistently yielded higher PyC concentrations than CTO-360, in line with its ability to oxidize a broader suite of aromatic domains, including intermediate-order structures and partially oxygenated charred materials (Hammes *et al.*, 2007; Masiello & Berhe, 2020). Conversely, CTO-360 isolates only the most condensed and thermally stable polyaromatic clusters (Gustafsson *et al.*, 1997, 2001), resulting in systematically lower PyC estimates.

Despite these operational differences, both methods displayed strong internal coherence. Linear regressions between PyC and SOC revealed high and depth-consistent associations for both CTO-360 (r = 0.67-0.91) and CO (r = 0.58-0.97), indicating that each method captures consistent vertical and spatial gradients in PyC abundance. Regression slopes were systematically steeper for CO than CTO-360, reflecting higher sensitivity to variations in total organic matter concentration. Pairwise ANCOVA contrasts confirmed that slopes and intercepts did not differ significantly among depths ($p > 0.05$), suggesting a stable methodological offset across the sampled depth intervals rather than depth-specific divergences.

Taken together, these results demonstrate that CTO-360 and CO provide complementary windows into the PyC continuum: CTO-360 isolates the most refractory fraction, while CO captures both refractory and intermediate components. Their combined interpretation strengthens the characterization of PyC pools in urban forest soils by distinguishing among fractions associated with long-term stabilization versus more reactive aromatic domains.

4.2 Controls on PyC-SOC-texture relationships and implications for soil carbon dynamics

PyC showed strong, positive correlations with SOC across the entire 0-40 cm dataset for both CTO-360 and CO (r = 0.58-0.97, $p < 0.01$), supporting the close coupling between pyrogenic and non-pyrogenic organic matter stocks. These relationships reflect both co-deposition of combustion-derived particulates and co-accumulation within mineral horizons over decadal timescales (Bird *et al.*, 2015; Santín *et al.*, 2015a). The increasing PyC:SOC ratios for both methods with depth further suggests selective preservation of condensed aromatic structures relative to more labile SOC fractions.

Soil texture exerted a secondary but detectable influence. PyC (CTO-360) correlated with sand at 0-10 and 10-20 cm (r = 0.24-0.72, $p < 0.05$), and both PyCs correlated with clay at 10-20 cm (r = 0.33 and 0.52 respectively for CTO-360 and CO, with no significance). These patterns reflect the dual role of coarse and fine minerals in stabilizing aromatic materials through surface interactions and aggregate protection (Liu *et al.*, 2019; Zhan *et al.*, 2024). In contrast, both PyCs showed no significant relationships with avP or pH across depths, whereas correlations with N were consistently strong for both methods (CTO-360: r = 0.73-0.95, $p < 0.05$; CO: r = 0.66-0.94, $p < 0.01$, except for the 0-10 cm). The tight PyC-N coupling reflects the co-accumulation of pyrogenic and non-pyrogenic organic matter, while the absence of associations with avP and pH highlights the limited involvement of PyC in short-term nutrient dynamics.

Collectively, these observations support a model in which PyC in urban forest soils is governed primarily by long-term stabilization, via mineral associations, physical occlusion, and resistance to microbial degradation, rather than by active biogeochemical cycling. This reinforces the view of PyC as a persistent and structurally stable carbon reservoir within anthropogenic forest ecosystems.

4.3 SOC_nPyC as a primary driver of metal retention

Across the pooled 0-40 cm dataset (n = 24), SOC_nPyC displayed clear and significant associations with several heavy metals, whereas PyC showed weak or absent relationships.

SOC_nPyC correlated strongly with Zn (SOC_nPyC (CTO-360): $r = 0.67$, $p < 0.01$; SOC_nPyC (CO): $r = 0.68$, $p < 0.01$), Ni (SOC_nPyC (CTO-360): $r = 0.52$, $p < 0.01$; SOC_nPyC (CO): $r = 0.51$, $p < 0.01$), Cr (both SOC_nPyC: $r \approx 0.42$, $p < 0.05$), while correlations with Pb (both SOC_nPyC $r = 0.32$, $p > 0.10$) and Cu (SOC_nPyC (CTO-360): $r = 0.34$, $p > 0.10$; SOC_nPyC (CO): 0.33, $p > 0.10$) were weaker and non-significant. These patterns align with the well-established affinity of Zn, Ni, and Cr for reactive SOM functional groups - carboxyl, phenolic, and carbonyl domains - through complexation, ligand exchange, and organo-mineral interactions (Bartkowiak *et al.*, 2017; Chandramohan *et al.*, 2025). By contrast, Pb sorption in soils is less dependent on organic ligands and more strongly governed by atmospheric deposition history, mineral associations, and low-mobility speciation.

Single-depth analysis (n = 8 per layer) yielded weaker and non-significant relationships ($p > 0.10$), reflecting limited statistical power at individual depth-interval scale. However, correlations emerging from the pooled depth-integrated dataset demonstrate that SOC_nPyC represents the dominant C fraction regulating the retention of transition metals (Zn, Ni, Cr) in these soils. The negligible correlations between PyC and metals across depths reinforce the limited sorption capacity of condensed aromatic structures, which contain few polar functional groups and exhibit minimal cation-exchange reactivity (Masiello, 2004; Hammes *et al.*, 2007).

Overall, SOC_nPyC - not PyC - is the primary biogeochemical driver of metal retention in these peri-urban forest soils.

However, these associations should be interpreted with caution. Trace metal concentrations were measured on the bulk fine soil fraction, rather than on isolated PyC or black carbon particles. Consequently, the observed correlations do not allow direct inference on specific metal-PyC binding mechanisms. Moreover, the strong covariance among soil properties (e.g. SOC, texture and pH) indicates a high degree of multicollinearity, which limits causal attribution to individual carbon fractions. The reported relationships therefore reflect general co-variations within the soil system rather than direct sorption processes, which would require targeted analyses on isolated carbon pools.

4.4 Site-specific variability and legacy Pb patterns

Although not a primary objective of this study, a site-specific variability in Pb concentrations emerged within the investigated area, reflecting spatial heterogeneity likely related to historical inputs rather than to current soil carbon composition.

Sectoral comparisons revealed a consistent north-south gradient for Pb, with significantly higher concentrations in northern sites across all depths ($p < 0.05$). No differences were detected for SOC, PyC (CTO-360 or CO), or SOC_nPyC, confirming that the spatial pattern is not driven by soil properties but by external deposition dynamics.

The northern sector is situated closer to historically congested transportation corridors - including the A4 motorway and dense urban traffic within the Cinisello-Bresso-Sesto San Giovanni axis - which have been identified as hotspots of Pb and other heavy metals in urban soils (Torretta *et al.*, 2005). Similar persistence of Pb hotspots has been documented in European cities decades after the ban of leaded gasoline (Hofman *et al.*, 2018). The presence of elevated Pb even at 20-40 cm suggests long-term incorporation of deposited particles and extremely slow downward migration, consistent with Pb's geochemical immobility in moderately acidic, carbon-rich soils.

In contrast, Zn, Ni, and Cr - metals that correlate with SOC_nPyC - did not differ between sectors, indicating control by internal soil processes rather than by spatial patterns of atmospheric inputs. Pb therefore behaves as a robust tracer of legacy traffic emissions rather than of soil carbon composition or reactivity.

4.5 Depth-dependent stabilization of PyC and vertical patterns

Although absolute PyC concentrations measured by both methods decreased with depth, both PyC:SOC ratios increased toward 20-40 cm, indicating selective preservation of condensed aromatic carbon relative to more labile SOC. This depth-dependent enrichment aligns with conceptual models of PyC stability based on resistance to microbial oxidation, sorption to mineral surfaces, and physical protection within aggregates (Bird *et al.*, 2015; Naisse *et al.*, 2015).

Differences between CTO-360 and CO provide insight into PyC structural "maturity". The larger CO-CTO gap in surface layers reflects a greater abundance of intermediate, partially oxidized aromatic materials likely derived from historical combustion sources and atmospheric deposition. Conversely, the narrower gap at depth suggests progressive dominance of the most condensed aromatic clusters (Hammes *et al.*, 2007; Masiello & Berhe, 2020), consistent with long-term stabilization within mineral soil layers.

These vertical patterns show that PyC behaves largely as an inert and persistent carbon pool within these urban forest soils, one that retains a clear legacy signal of past deposition and site history while contributing to long-term carbon storage capacity.

4.6 Ecosystem services-level relevance of PyC-rich soils

Urban and peri-urban forest soils provide multiple ecosystem services that are influenced by the composition and stability of their carbon pools. PyC contributes to:

1. Long-term carbon sequestration, due to its multi-decadal persistence and low degradability. Even modest PyC concentrations can buffer carbon losses in soils exposed to disturbance and anthropogenic pressures.

2. Indirect pollution buffering, through its co-occurrence with SOC. While PyC itself does not bind metals effectively, PyC-rich soils often contain higher SOC_nPyC concentrations, enhancing retention of Zn, Ni, and Cr.
3. Soil structural development, promoting aggregation and improved porosity, with implications for water regulation and plant establishment.
4. Belowground habitat provision, as PyC particles create microsites with distinct redox and sorption environments that can influence microbial assemblages.
5. Nature-based solutions, by combining carbon storage, pollution mitigation, and support for vegetation in highly anthropogenic environments (Sanesi *et al.*, 2007; Chandramohan *et al.*, 2025).

Understanding the interactions among PyC, SOC_nPyC, heavy metals, and soil texture is therefore critical for managing urban forest soils as multifunctional ecological infrastructures.

5. Conclusions

This study demonstrates that PyC in urban forest soils constitutes a highly persistent and chemically stable carbon pool, whereas SOC_nPyC primarily governs metal retention and biogeochemical reactivity. The two analytical approaches applied, CTO-360 and CO, provide complementary insights into PyC composition by targeting distinct portions of the combustion continuum. However, their divergence is primarily expressed in surface soils, where CO yields systematically higher PyC concentrations by capturing a broader range of less refractory aromatic structures. With increasing soil depth, PyC estimates obtained by the two methods progressively converge, indicating that deeper horizons are dominated by highly condensed and thermally stable PyC forms that are similarly isolated by both approaches.

Across soil depth intervals, relationships between carbon pools and trace metals were predominantly mediated by SOC_nPyC, while PyC itself exhibited limited direct associations with metal concentrations. This highlights the importance of distinguishing between pyrogenic and non-pyrogenic carbon fractions when interpreting carbon-metal interactions in urban soils.

Overall, these findings underscore that both methodological choice and depth of investigation critically influence the assessment of PyC dynamics and its environmental implications. Incorporating method-aware PyC quantification into urban soil studies is therefore essential for improving the comparability of datasets and for advancing our understanding of carbon storage and contaminant dynamics in anthropogenic landscapes.

References

Bartkowiak, A., Lemanowicz, J., & Breza-Boruta, B. (2017). Evaluation of the content of Zn, Cu, Ni and Pb as well as the enzymatic activity of forest soils exposed to the effect of road traffic pollution. *Environmental Science and Pollution Research*, 24, 23893-23902. https://doi.org/10.1007/s11356-017-0013-3.

Bird, M. I., Brand, M., Comley, R., Fu, X., Hadeen, X., Jacobs, Z., Rowe, C., Wurster, C. M., Zwart, C., & Bradshaw, C. J. A. (2024). Late Pleistocene emergence of an anthropogenic fire regime in Australia's tropical savannahs. *Nature*, 17, 233-240. https://doi.org/10.1038/s41561-024-01388-3.

Bird, M. I., Wynn, J. G., Saiz, G., Wurster, C. M., & McBeath, A. (2015). The pyrogenic carbon cycle. *Annual Review of Earth and Planetary Sciences*, 43, 273-298. https://doi.org/10.1146/annurev-earth-060614-105038.

Chandramohan, M.S., Martinho da Silva, I., Ribeiro, R. P., Jorge, A., & Esteves da Silva, J. (2025). Screening urban soil contamination in Rome: insights from XRF and multivariate analysis. *Environments*, 12(4), 126. https://doi.org/10.3390/environments12040126.

Cohen, J. (1988). Statistical Power Analysis for the Behavioral Sciences (2nd ed.). Routledge. https://doi.org/10.4324/9780203771587.

Day, R. P. (1965) Pipette Method of Particle Size Analysis. In: Methods of Soil Analysis, Agronomy No. 9, ASA, Madison, 553-562.

Elmquist, M., Gustafsson, Ö., & Andersson, P. (2004). Quantification of sedimentary black carbon using the chemothermal oxidation method: an evaluation of ex situ pretreatments and standard additions approaches. *Limnology and Oceanography: Methods*, 2, 417-427. https://doi.org/10.4319/lom.2004.2.417.

Glaser, B., Balashov, E., Haumaier, L., Guggenberger, G., & Zech, W. (2000). Black carbon in density fractions of anthropogenic soils of the Brazilian Amazon region. *Organic Geochemistry*, 31(7-8), 669-678. https://doi.org/10.1016/S0146-6380(00)00044-9.

Gustafsson, Ö., Bucheli, T. D., Kukulska, Z., Andersson, M., Largeau, C., Rouzaud, J-N., Reddy, C. M. and Eglinton, T. I. (2001). Evaluation of a protocol for the quantification of black carbon in sediments. *Global Biogeochemical Cycles*, 15(4), 881-890. https://doi.org/10.1029/2000GB001380.

Gustafsson, Ö., Haghseta, F., Chan, C., MacFarlane, J., & Gschwend, P. M. (1997). Quantification of the dilute sedimentary soot phase: implications for PAH speciation and bioavailability. *Environmental Science & Technology*, 31, 203-209. https://doi.org/10.1021/es960317s.

Hammes, K., Schmidt, M. W. I., Smernik, R. J., Currie, L. A., Ball, W. P., Nguyen, T. H., … Ding, L. (2007). Comparison of quantification methods to measure fire-derived (black/elemental) carbon in soils and sediments using reference materials from soil, water, sediment and the atmosphere. *Global Biogeochemical Cycles*, 21, GB3016. https://doi.org/10.1029/2006GB002914.

Herring, J. R., (1985). Charcoal fluxes into sediments of the North Pacific Ocean: the Cenozoic record of burning. In: Sundquist, E. T., Broecker, W. S. (eds). The carbon cycle and atmospheric CO_2: natural variations Archean to present. Washington DC: AGU. pp 419-442. https://doi.org/10.1029/GM032p0419.

Hofman, J., Samson, R., Joosen, S., Blust, R., & Lenaerts, S. (2018). Cyclist exposure to black carbon, ultrafine particles and heavy metals: an experimental study along two commuting routes near Antwerp, Belgium. *Environmental Research*, 164, 530-538. https://doi.org/10.1016/j.envres.2018.03.004.

ISO, 1995. Soil quality, determination of carbonate content - Volumetric method, ISO 10693.

ISO, 1995. Soil quality, extraction of trace elements soluble in aqua regia, ISO 11466.3.

IUSS Working Group WRB (2022). World Reference Base for Soil Resources: International soil classification system for naming soils and creating legends for soil maps (4th ed.). International Union of Soil Sciences (IUSS).

Kuhlbusch, T. A. J. (1999). Black carbon and the global carbon and oxygen cycle. Contribution No. 971, p. 163. *Ninth Annual Goldschmidt Conference*, Lunar and Planetary Institute, Houston, USA.

Kuhlbusch, T. A. J., & Crutzen, P. J. (1995). Toward a global estimate of black carbon in residues of vegetation fires representing a sink of atmospheric CO_2 and a source of O_2. *Global Biogeochemical Cycles*, 9(4), 491-501. https://doi.org/10.1029/95GB02742.

Liu, Y. H., Wang, X. S., Guo, Y. H., Mao, Y. M., & Li, H. (2019). Association of black carbon with heavy metals and magnetic properties in soils adjacent to a cement plant, Xuzhou (China). *Journal of Applied Geophysics*, 170, 103802. https://doi.org/10.1016/j.jappgeo.2019.06.018.

Masiello, C. A. (2004). New directions in black carbon organic geochemistry. *Marine Chemistry*, 92(1-4), 201-213. https://doi.org/10.1016/j.marchem.2004.06.043.

Masiello, C. A., & Berhe, A. A. (2020). First interactions with the hydrologic cycle determine pyrogenic carbon's fate in the Earth system. *Earth Surface Processes and Landforms*, 45, 2394-2398. https://doi.org/10.1002/esp.4925.

Naisse, C., Girardin, C., Davasse, B., Chabbi, A., & Rumpel, C. (2015). Effect of biochar addition on C mineralisation and soil organic matter priming in two subsoil horizons. *Journal of Soils and sediments*, 15, 825-832. https://doi.org/10.1007/s11368-014-1002-5.

Olsen, S. R., & Dean, L. A. (1965). Phosphorus, Methods of Soil Analysis Part 2, Chemical and Microbiological Properties. Madison, Wisconsin: American Society of Agronomy, Inc.

R Core Team (2025) R: A Language and Environment for Statistical Computing. *R Foundation for Statistical Computing*. https://www.r-project.org/.

Ren, Y., Oxford, C. R., Zhang, D., Liu, X., Zhu, H., Dillner, A. M., ... Martin, R. V. (2025). Black carbon emissions generally underestimated in the global south as revealed by globally distributed measurements. *Nature Communications*, 16, 7010. https://doi.org/10.1038/s41467-025-62468-5.

Sanesi, G., Lafortezza, R., Marziliano, P. A., Ragazzi, A., & Mariani, L. (2007). Assessing the current status of urban forest resources in the context of Parco Nord, Milan, Italy. *Landscape and Ecological Engineering*, 3, 187-198. https://doi.org/10.1007/s11355-007-0031-2.

Santín, C., Doerr, S. H., Kane, E. S., Masiello, C. A., Ohlson, M., de la Rosa, J. M., Preston, C. M., & Dittmar, T. (2015b). Towards a global assessment of pyrogenic carbon from vegetation fires. *Global Change Biology*, 22, 76-91. http://doi.org/10.1111/gcb.12985.

Santín, C., Doerr, S. H., Merino, A., Bucheli, T. D., Bryant, R., Ascough, P., Gao, X. & Masiello, C., A. (2017). Carbon sequestration potential and physicochemical properties differ between wildfire charcoals and slow-pyrolysis biochars. *Scientific Reports*, 7, 11233. https://doi.org/10.1038/s41598-017-10455-2.

Santín, C., Doerr, S. H., Preston, C. M., & González-Rodríguez, G. (2015a). Pyrogenic organic matter production from wildfires: a missing sink in the global carbon cycle. *Global Change Biology*, 21, 1621-1633. https://doi.org/10.1111/gcb.12800.

Schmidt, M. W. I., Skjemstad, J. O., Czimczik, C. I., Glaser, B., Prentice, K. M., Gelinas, Y., & Kuhlbusch, T. A. J. (2001). Comparative analysis of black carbon in soils. *Global Biogeochemical Cycles*, 15(1), 163-167. https://doi.org/10.1029%2F2000GB001284.

Torretta, M., Confalonieri, M., & Zangari, R. (2005). Influenza delle attività antropiche sulla concentrazione di metalli pesanti nei suoli di un'area urbana. *Siti Contaminati*, 2(2), 132-145.

Xie, Y., Li, C., Chen, H., Gao, Y., Vancov, T., Keen, B., Van Zwieten, L., Fang, Y., Sun, X., He, Y., Li, X., Bolan, N., Yang, X., & Wang, H. (2024). Methods for quantification of biochar in soils: a critical review. Catena, 241, 108082. https://doi.org/10.1016/j.catena.2024.108082.

Zhan, C., Wan, D., Han, Y., Zhang, J., Liu, S., Liu, H., Hu, T., Xiao, W., Cao, J., & Li, D. (2024). Decadal trends of black carbon and heavy metal accumulation in a lake sediment core from central China: A historical perspective. *Catena*, 247, 108513. https://doi.org/10.1016/j.catena.2024.108513.

Appendix

Figures A1-A4

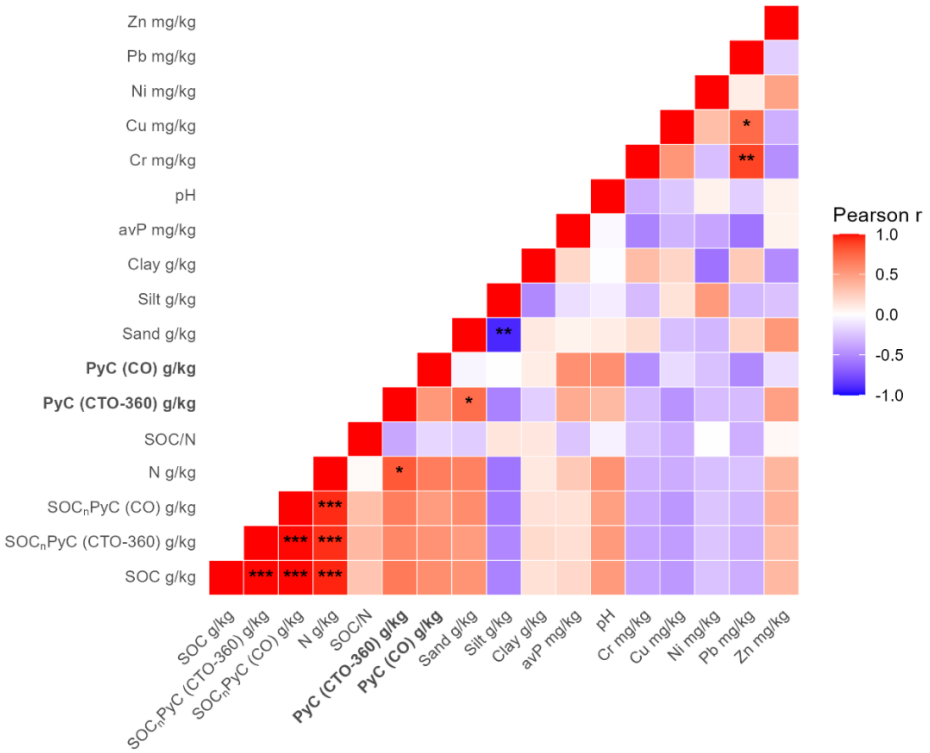

Figure A1.

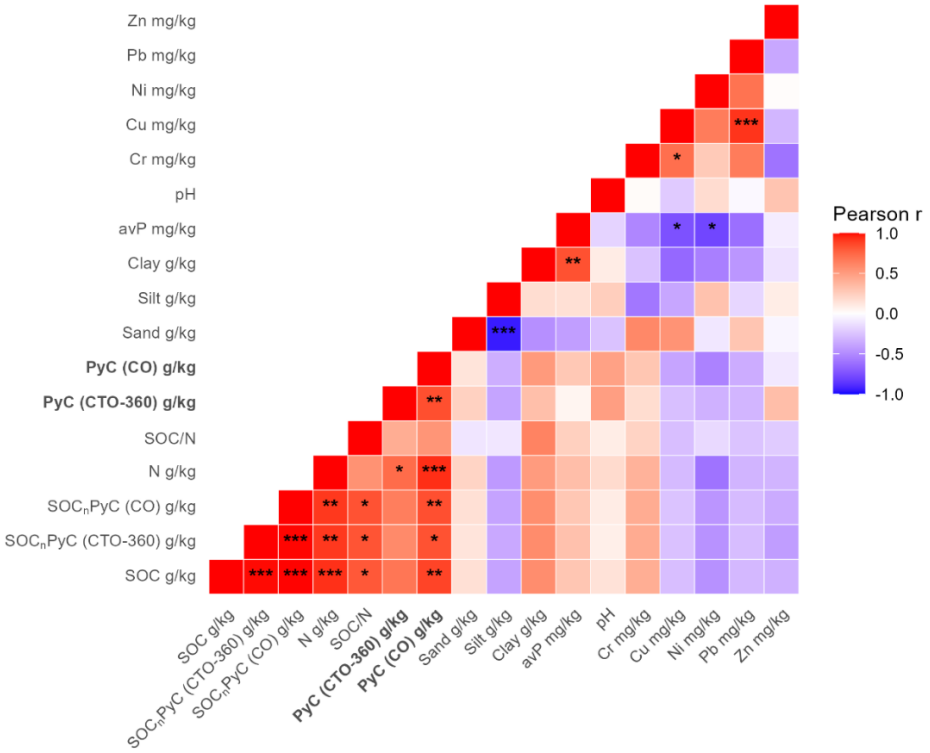

Figure A2.

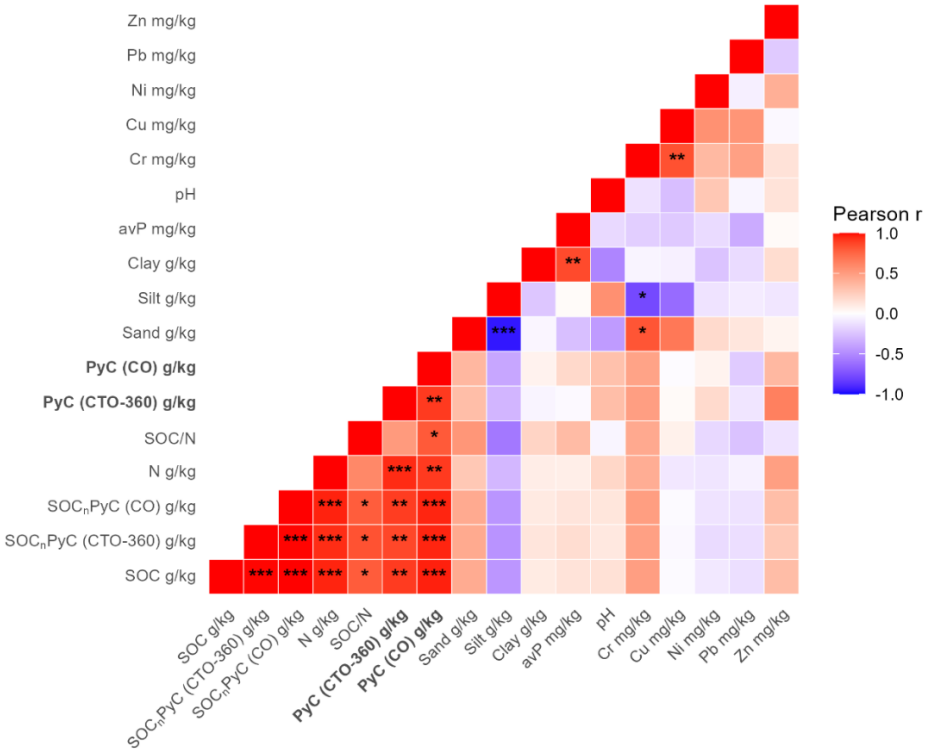

Figure A3.

Figures A1-A3. Pearson correlation matrix among soil physicochemical parameters at different depths:

Figure A1: 0-10 cm; Figure A2: 10-20 cm; Figure A3: 20-40 cm. The color gradient indicates the strength and direction of linear relationships (blue = negative, red = positive). All correlations were computed using pairwise complete observations.

Significant correlations are highlighted as follows: *** $p < 0.001$ | ** $p < 0.01$ | * $p < 0.05$.

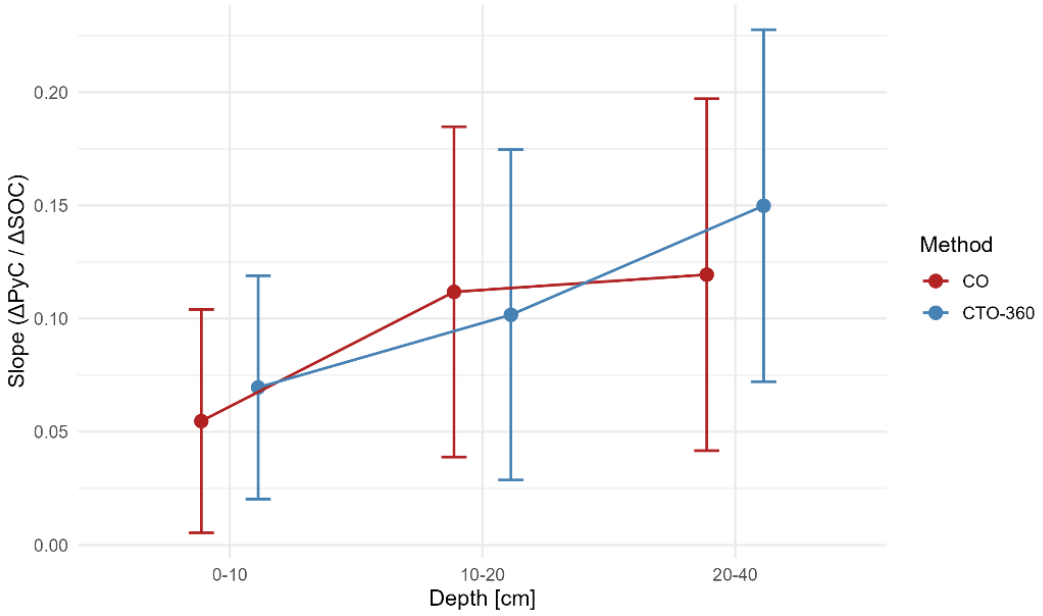

Figure A4. Slopes (±95% confidence intervals) of linear regressions between PyC and SOC concentrations for the CO and CTO-360 methods across the three depth intervals. Slopes represent the sensitivity of PyC to changes in SOC within each soil layer. Differences between methods within individual depths should be interpreted cautiously due to overlapping confidence intervals. Depth is used here as a stratification factor, with regressions fitted independently for each layer.

Tables A1-A2

Table A1. Descriptive statistics of pyrogenic carbon (PyC) concentrations (g kg^{-1}) determined by chemical oxidation (CO) and chemo-thermal oxidation (CTO-360) across soil depth intervals. Reported values include sample size (n), mean, standard deviation (SD), coefficient of variation (CV %), minimum (min), and maximum (max).

Method PyC	depth	n	mean (g kg^{-1})	SD	CV (%)	min	max
CTO-360	0-10 cm	8	1.79	0.75	41.8	1.14	3.40
CO	0-10 cm	8	2.77	0.68	24.7	1.45	3.48
CTO-360	10-20 cm	8	1.38	0.72	52.2	0.81	3.09
CO	10-20 cm	8	1.66	0.62	37.3	0.96	2.77
CTO-360	20-40 cm	8	1.21	0.75	62.4	0.68	3.00
CO	20-40 cm	8	1.28	0.56	43.9	0.82	2.53
CTO-360	0-40 cm	24	1.46	0.75	51.5	0.68	3.40
CO	0-40 cm	24	1.90	0.88	46.2	0.82	3.48

Table A2. Descriptive statistics of soil properties at different depths (0-10 cm, 10-20 cm, and 20-40 cm). Reported values include mean, standard deviation (SD), coefficient of variation (CV %), minimum (min), and maximum (max) for each variable. Variables comprise pH, soil organic carbon (SOC), total nitrogen (N), SOC:N ratio, calcium carbonate ($CaCO_3$), available phosphorus (avP), and texture fractions (sand, silt, clay).

Variable	depth	mean	SD	CV %	min	max
pH	0-10 cm	5.33	0.72	13,57	4.5	6.6
	10-20 cm	5.21	0.82	15,77	4.4	6.8
	20-40 cm	5.34	0.94	17,54	4.4	7.3
SOC g kg^{-1}	0-10 cm	31.53	7.19	22,79	18.9	44.3
	10-20 cm	14.47	4.86	33,58	7.9	21.3
	20-40 cm	10.78	4.56	42,30	6.7	21.1
N g kg^{-1}	0-10 cm	2.64	0.59	22,33	1.6	3.8
	10-20 cm	1.40	0.31	22,12	1.0	1.9
	20-40 cm	1.12	0.32	29,05	0.8	1.8
SOC:N ratio	0-10 cm	11.95	0.79	6,59	10.8	13.1
	10-20 cm	10.14	1.64	16,14	7.1	11.8
	20-40 cm	9.44	1.33	14,12	7.1	11.4
$CaCO_3$ g kg^{-1}	0-10 cm	0.0	0.0	-	0	0
	10-20 cm	0.0	0.0	-	0	0
	20-40 cm	0.5	1.4	-	0	4
avP mg kg^{-1}	0-10 cm	29.852	13.474	45,14	13.00	57.06
	10-20 cm	23.689	14.535	61,36	8.67	54.20
	20-40 cm	20.511	15.819	77,12	7.23	55.74
Sand g kg^{-1}	0-10 cm	469.0	47.1	10,04	407	561
	10-20 cm	456.0	45.4	9,95	405	531
	20-40 cm	464.4	52.1	11,22	401	541
Silt g kg^{-1}	0-10 cm	466.4	54.3	11,64	379	540
	10-20 cm	450.4	40.4	8,97	401	501
	20-40 cm	439.0	53.7	12,23	368	519
Clay g kg^{-1}	0-10 cm	64.6	22.1	34,25	40	105
	10-20 cm	93.6	14.7	15,74	68	115
	20-40 cm	96.6	15.2	15,73	80	125

Chapter 4.

Although this chapter is presented as a standalone published article, it is conceptually embedded within the broader framework of this thesis. The previous chapters have demonstrated how soil organic matter composition, including both biogenic SOC and Pyrogenic Carbon, and their depth-dependent distribution govern carbon persistence and ecosystem functioning in urban soils. These same properties also play a key role in regulating sorption processes and contaminant mobility.

In this context, the present chapter extends the multifunctional soil perspective by focusing on contaminant transport processes in unsaturated urban soils. It highlights how soil heterogeneity, hydraulic properties, and parameter uncertainty interact with soil carbon-related properties to control the mobility of heavy metals, thereby linking carbon dynamics to environmental risk processes.

Heavy metals in unsaturated urban soils: Experimental insights and stochastic forecasting

Aronne Dell'Oca[(a)], Davide Abu El Khair[(b)], Chiara Ferré[(b)], Roberto Comolli[(b)], Monica Riva*[(a)]

(a) Department of Civil and Environmental Engineering, Politecnico di Milano, Piazza L. Da Vinci, 32, 20133 Milano, Italy

(b) Department of Earth and Environmental Sciences, Piazza della Scienza 1, 20126 Milan, Italy

*Corresponding author. E-mail address: monica.riva@polimi.it

Received 2 December 2025, Revised 8 January 2026, Accepted 13 January 2026, Available online 19 January 2026, Version of Record 31 January 2026. https://doi.org/10.1016/j.jconhyd.2026.104855

Abstract

The toxicity and long-term persistence of heavy metals pose a major threat across environmental compartments. Heavy metal contamination of soils poses long-term risks to groundwater resources, particularly in urban environments where rainfall-driven infiltration under unsaturated conditions can promote contaminant migration toward underlying aquifers. The aim of this study is to assess how uncertainty in soil hydraulic and sorption properties affects predictions of heavy metals migration from urban soils to groundwater. To this aim, we cast our work in a stochastic framework that integrates column scale drainage experiments and batch sorption tests to estimate key parameters governing water flow and heavy metal sorption dynamic, along with their associated uncertainty. Monte Carlo simulations are then performed to mimic the rainfall-induced drainage of heavy metals from metal-enriched soils through sewage sludge application. We consider two representative urban soil types and five heavy metals commonly detected in urban environments, i.e. lead (Pb), copper (Cu), chromium (Cr), nickel (Ni) and zinc (Zn). Our results indicate that Cr is highly mobile, while Ni, Zn, Cu exhibit consistently low mobility across both soils. Lead displays a strong soil-dependent behavior, transitioning from high to low mobility depending on the substrate. Outputs of a rigorous global sensitivity analysis reveal that, for highly mobile metals, flow and transport parameters have significant influence on metals migrations, reflecting the strong interplay of unsaturated flow and reactive transport processes. On the other hand, for low mobile heavy metals, parameters defining the initial contamination conditions and soil water content dominate the temporal evolution of metals retention in the soil. These findings indicate that parameter uncertainty and flow-transport processes in the vadose zone should be explicitly considered in groundwater contamination risk assessment protocols for urban environments.

1. Introduction

Heavy metals are among the most hazardous soil contaminants due to their toxicity and non-degradable nature that could potentially result in long-term ecological damages. Once released and accumulated in soils, they can disrupt ecosystem functioning by affecting soil microbial communities, invertebrates (e.g., earthworms, nematodes, arthropods), and plant species that are highly sensitive to metal toxicity. Heavy metals interfere with the microbial activities, enzyme dynamics, and nutrient cycling leading to a decline in soil fertility and resilience (e.g., Giller *et al.*, 1998; Khan *et al.*, 2010), loss of biomass, species richness, and trophic complexity (e.g., Kandeler *et al.*, 1999; Stefanowicz *et al.*, 2008).

The impact of heavy metals extends beyond the soil compartment. Under specific hydrological conditions, particularly during rainfall infiltration events, these contaminants can migrate through the unsaturated zone and reach underlying aquifers. Such processes are of particular concern in urban and peri-urban areas, where both anthropogenic inputs and population exposure risks are elevated (Kumar *et al.*, 2024; Ariman and Balkaya, 2025; Pan *et al.*, 2025). Urban soils are widely recognized as hotspots of heavy metal contamination due to the superposition of multiple anthropogenic sources, including historical industrial activities, traffic emissions, combustion processes, atmospheric deposition, and poorly managed waste (Li *et al.*, 2001; Lu *et al.*, 2010; Adamiec *et al.*, 2016; Wang *et al.*, 2024). Urban green spaces, such as parks, gardens and urban woodlands, are increasingly recognized for their provision of key ecosystem services, by supporting biodiversity, regulating microclimates, and facilitating rainwater infiltration. However, their ecological performance can be severely compromised by heavy metal pollution. The mobility of these contaminants depends on multiple factors, such as soil pH, redox potential, organic matter content, and texture, which complicates the prediction of their behavior in the subsurface environment (e.g., Ma *et al.*, 2026). Once reaching groundwater, they may persist and accumulate (Alloway, 2013; Tóth *et al.*, 2016) posing significant concerns for water quality. The presence of heavy metals in shallow aquifers has been linked to adverse effects on human health and ecosystem services, reinforcing the need for integrated studies that consider both soil and water compartments (Tian *et al.*, 2023; Khan *et al.*, 2025; Rostami *et al.*, 2025; Manan *et al.*, 2026; Liu *et al.*, 2026).

Awareness of the environmental and health threats posed by heavy metal pollution has led the European Union (EU) to develop regulatory frameworks aimed at soil and water protection. Several existing policies, such as the Water Framework Directive (2000/60/EC), the Industrial Emissions Directive (2010/75/EU), and the Thematic Strategy for Soil Protection (COM(2006) 231, COM(2021) 699), include measures to control and limit metal emissions. The recent EU Soil Strategy for 2030 explicitly identifies the remediation of contaminated soils as a key priority, especially in urban areas. It emphasizes the importance of protecting soils as a non-renewable resource, recognizing their role in supporting biodiversity, food security, and climate mitigation.

The fate of heavy metals in the subsurface can be predicted using the laws of mass and momentum conservation. Solving these equations requires to specify a set of hydraulic and transport parameters, imbuing the characteristic of the soil and its interactions with water and heavy metals (e.g., Selim *et al.*, 2023; Xu *et*

al., 2024) and to hydraulic conductivity (e.g. Pan *et al.*, 2009; He *et al.*, 2023). These parameters are typically inferred by means of laboratory or field experiments. However, their estimation is ubiquitously affected by uncertainty (e.g., Kahl *et al.*, 2015; Younes *et al.*, 2017; Ma *et al.*, 2026; Kahl *et al.*, 2015). Quantifying the impact of parameters uncertainty on quantities of interest is a critical issue in risk assessment frameworks (e.g., Dye *et al.*, 2009; Deng *et al.*, 2009; Jiang *et al.*, 2023; Shao *et al.*, 2023). For example, Ye et al. (2007) showed that in a reactive transport scenario involving radionuclide adsorption in an unsaturated aquifer, inclusion of uncertainty in adsorption parameters substantially increases the uncertainty in radionuclide fate prediction. The authors also reported a strong correlation between percolating water fluxes and radionuclide concentrations, suggesting that knowledge of the former could help reduce uncertainty in the latter. Van der Grift and Griffioen (2008) identified the soil sediment composition (i.e., organic matter, clay minerals and iron oxides) as the dominant factors controlling heavy metal fate in a regional-scale aquifer. Bonten et al. (2012) highlighted the importance of including transient effects associated with water infiltration and heavy metal transport to accurately predict metal fate at the catchment scale.

Beyond uncertainty quantification, identifying the dominant processes and parameters controlling heavy metal transport is critical for improving model interpretability and guiding data acquisition efforts. Global Sensitivity Analysis (GSA) provides a rigorous framework for this purpose. Among the available GSA strategies, the moment-based AMA indices introduced by Dell'Oca et al. (2017) quantify the contribution of the uncertainty in model parameters to the statistical moments of target model outputs and have been successfully applied in a range of hydrological and environmental studies (e.g., Bianchi Janetti *et al.*, 2019; Dell'Oca, 2023; Ceresa *et al.*, 2023; Dell'Oca *et al.*, 2023; Sandoval *et al.*, 2024).

In this work, we present, to the best of our knowledge, the first comprehensive framework that integrates laboratory-scale experiments with stochastic modeling, uncertainty propagation, and global sensitivity analysis to investigate heavy metal transport processes in unsaturated urban soils. The overall workflow and interconnections among its components are summarized in Figure 1. Our goal is to assess the impact of multiple sources of uncertainty in the percolation of heavy metals from contaminated urban soils to the underlying aquifers. The specific objectives of this study are to: (i) estimate key hydraulic and sorption parameters within a stochastic calibration framework; (ii) quantify how residual (i.e. after calibration) parameter uncertainty propagates to predictions of water flow and heavy metal retention or percolation; and (iii) identify the dominant factors controlling heavy metal mobility under unsaturated conditions. By explicitly linking experimental observations with probabilistic modeling and GSA, this study provides process-based insights into heavy metal migration in the vadose zone and its implications for groundwater contamination risk.

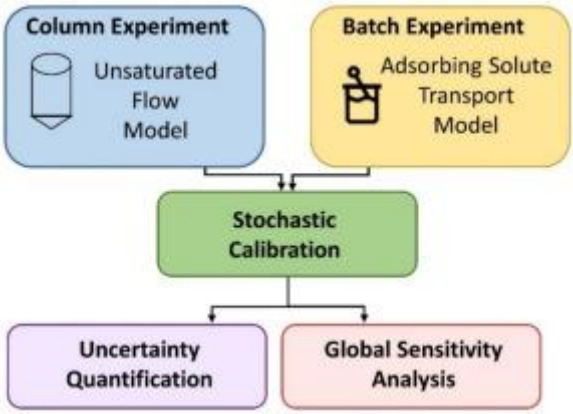

Figure 1. Workflow and interconnections among its components.

The manuscript is organized as follows. In Section 2, we describe the experiments setup. Section 3 presents the theoretical modeling framework and the stochastic calibration approach. Section 4 discusses the main results, and concluding remarks are provided in Section 5.

2. Experimental set-up

The experiments were conducted on two soil horizons collected from a peri-urban park located in northern Milano (Parco della Balossa, Italy). The study area is part of Parco Nord Milano (in the Po Plain), an urban park of high environmental and naturalistic value located within one of the most densely urbanized regions in Europe. The park has developed in a setting historically characterized by intense industrial activity (now largely dismissed), along with agricultural use and subsequent residential development. Thanks to its strategic location, Parco Nord Milano has been the subject of large-scale reforestation and green infrastructure development since the late 1980s, explicitly aimed at enhancing soil permeability, increasing infiltration capacity, and mitigating urban flooding. While these measures provide important hydrological and ecological benefits, they also enhance groundwater recharge pathways, potentially increasing the vulnerability of the underlying aquifer to contaminant leaching. As discussed in the introduction, we focus on five heavy metals (Ni, Cu, Pb, Zn, Cr) commonly detected in urban soils, particularly in areas that have undergone a transition from agricultural and industrial to urban setting, such as the site considered in this study. These metals are regulated under EU Directive 86/278/EEC on sewage sludge application, and their selection enables comparison across a range of mobility behaviors. Their occurrence in soils is linked to both historical agricultural activities, such as the use of fertilizers, pesticides and organic amendments (e.g., Adriano, 2001; Nicholson *et al.*, 2003), and current urban sources, including traffic emissions, construction materials and atmospheric deposition (Manta *et al.*, 2002; Ferreira *et al.*, 2016). Although trivalent chromium, Cr(III), is the dominant form in most soils, including urban and sludge-amended systems, its strong affinity for mineral surfaces and its tendency to precipitate as hydroxides make it essentially immobile under typical environmental conditions (pH 5-8). Hexavalent chromium, Cr(VI), though generally found at lower concentrations, is the most mobile and bioavailable species because its anionic forms (CrO_4^{2-}, $HCrO_4^-$) exhibit little sorption to negatively charged soil particles (Bartlett and James, 1979; Fendorf, 1995). Because risk assessment requires evaluation of worst-case scenarios, and since localized oxidizing conditions (e.g. periodic drying-wetting cycles, presence of Mn oxides) can promote the oxidation of Cr(III) to Cr(VI) in soils (Bartlett and James, 1979), we focused on chromium transport in its hexavalent form. This provides a conservative estimate of Cr mobility, representing upper-bound transport scenarios relevant to risk assessment in contaminated urban soils. Undisturbed soil samples were collected from a soil profile (Appendix Table A1) employing PVC and iron cylindrical pipes. According to the World reference base for soil Resources (IUSS Working Group WRB, 2022), the soil is classified as *Mollic Cambic Umbrisols (Loamic, Aric, Eutric, Humic)*. The presence of a mollic horizon, rich in organic matter, and a cambic horizon with incipient clay illuviation indicate a transition from fertile cultivated soils to more mature profiles, typical of plains surrounding metropolitan areas. The first two horizons selected for laboratory tests (topsoil and subsoil) differ primarily in organic carbon and clay content. We performed two types of laboratory experiments, as detailed in the following subsections: (i) percolation tests on undisturbed soil columns under unsaturated conditions, to determine soil hydraulic properties; and (ii) batch adsorption experiments to assess soil-water partitioning of heavy metals.

2.1. Hydraulic tests

The experimental setup consists of a cylindrical soil column with a diameter, D, of 0.14 m. The core height, L, is 0.25 m for the topsoil sample and 0.2 m for the subsoil sample. A layer of clay pebbles 5 cm thick is placed at the bottom of each column, sustained by a fiberglass grid with 1 mm openings, to support the soil column while minimizing interference with infiltration dynamics. Prior to testing, each soil column was saturated and then allowed to drain under gravity for about two days to reach field capacity. Then, a constant water head of 10 mm was applied at the column inlet using a 2-l bottle held with a clamp by a steel burette holder. The inflow Darcy flux, $\hat{q}_{in}(t)$, was determined by recording the volume of water spilled from the bottle over time, t, with evaporation prevented by sealing the column top with a plastic film. The resulting average inflow flux is approximately 4 mm h^{-1}, comparable to the mean rainfall intensity in the study area. The temporal evolution of the cumulative percolated water volume, $\widehat{W}(t)$, was monitored at the column outlet using a funnel positioned below the soil core.

2.2. Batch adsorption experiments

We conducted batch experiments to characterize the soil-water partitioning behavior of five selected heavy metals (Cr, Cu, Ni, Pb, Zn). For each combination of heavy metal and soil horizon, the sorption test was performed according to the following procedure. A water solution with a prescribed initial heavy metal concentration, C_0, was mixed with a soil sample at a soil to solution volume ratio of 1:2. Heavy metals were introduced in the following forms: Cr as potassium dichromate ($K_2Cr_2O_7$) providing Cr(VI), Cu as copper chloride ($CuCl_2$), Ni as nickel chloride hexahydrate ($NiCl_2 \cdot 6H_2O$), Pb as lead acetate trihydrate ($Pb(CH_3COO)_2 \cdot 3H_2O$), and Zn as zinc acetate dihydrate ($Zn(CH_3COO)_2 \cdot 2H_2O$). Note that, the use of readily soluble metal salts enhances their adsorption onto the soil matrix with respect to their counterpart forms present in sewage sludge, where metals present in sewage sludge are commonly complexed with organic matter, sulfides, or other ligands that limit their bioavailability. The resulting suspension was shaken for 24 h at 50 rpm to promote metal partitioning and then centrifuged for 15 min at 8000 rpm to segregate the liquid and solid phases. Finally, the equilibrium concentration of dissolved heavy metal in the water phase, $\hat{C}$, was measured using an atomic absorption spectrometer, AAS (PinAAcle 500 Flame AAS, PerkinElmer) and the equilibrium concentration of heavy metal adsorbed onto the soil matrix, $\hat{S}$, was evaluated via mass balance. This procedure yields equilibrium pairs of $\hat{C}$ and $\hat{S}$ for each heavy metal corresponding to initial concentration C_0. The procedure was repeated for nine initial concentrations, i.e.: C_0 = [0.5; 1.0; 2.0; 4.0; 8.0; 16.0; 32.0; 64.0; 128.0] ppm, enabling the estimation of adsorption isotherm parameters as described in Section 3.

3. Theoretical framework and methodological approach

3.1. Modeling approach for flow and reactive transport

We model each soil column as a one-dimensional homogeneous domain, where water flow occurs along the vertical, z, axis defined positive downward. Under unsaturated conditions, water movement is described at the continuum scale by the Richards' and Darcy' equations

$$\begin{cases}\left(c(h)+S_s\frac{\theta(h)}{\theta_s}\right)\frac{\partial h}{\partial t}=\frac{\partial q}{\partial z}\\ q=K(h)\left(\frac{\partial h}{\partial z}-1\right)\end{cases} \quad (1)$$

where h [L] is pressure head, defined as $h = p/(\rho g)$, p [$ML^{-1}T^{-2}$] being water pressure; g [LT^{-2}] gravitational acceleration and ρ [ML^{-3}] water density; q [LT^{-1}] is the Darcy velocity along z; t [T] is time; $\theta(h)$ [-] is the water content; $c(h) = d\theta(h)/dh$ [L^{-1}] is the specific moisture capacity; $K(h)$ [LT^{-1}] is the unsaturated hydraulic conductivity; and S_s [L^{-1}] is the specific storage, i.e., $S_s = \rho g \beta \theta_s$, being θ_s [-] saturated water content (i.e., porosity), and β [$M^{-1}LT^2$] water compressibility.

The nonlinear system (1) requires constitutive relationships defining the dependence of $\theta(h)$ and $K(h)$ on the pressure head. Here, we employ the widely used Mualem-Van Genuchten model, i.e.

$$\begin{cases}S_e(h)=\frac{\theta(h)-\theta_r}{\theta_s-\theta_r}=\begin{cases}(1+|\alpha h|^n)^{-m}h<0\\ 1h\geq 0\end{cases}\\ K(S_e)=K_s{S_e}^{1/2}\left[1-\left(1-S_e^{1/m}\right)^m\right]^2\end{cases} \quad (2)$$

where $S_e(h)$ [-] denotes the effective saturation; θ_r [-] is the residual water content; and K_s [LT^{-1}] is the saturated hydraulic conductivity. Parameters $\alpha > 0$ [L^{-1}] and $n > 1$[-] are scale and shape parameters, respectively, embedding water-soil interactions at pore scale and $m = 1 - 1/n$. Specifically, α is inversely proportional to the air-entry pressure head and controls the scale of the soil water retention curve, e.g., high values of α (typical of coarse-textured soils) indicate that water drains at relatively lower pressure heads. Parameter n, associated to the soil pore-size distribution, controls the steepness of the water retention curve, e.g., higher n values (typical of uniform pore-size distribution) result in steeper drop in water content as pressure head decreases.

Solute transport is governed by the advection-dispersion-sorption equation, i.e.

$$\frac{\partial}{\partial t}(\theta C+\rho_b S)+\frac{\partial qC}{\partial z}-\frac{\partial}{\partial z}\left(\theta D\frac{\partial C}{\partial z}\right)=0 \quad (3)$$

where C [ML^{-3}] is the dissolved solute concentration, S [MM_{ss}^{-1}] is the adsorbed solute concentration (i.e., mass of solute adsorbed per unit mass of solid phase, M_{ss}); ρ_b [$M_{ss}\,L^{-3}$] is the soil bulk density. The dispersion coefficient, $D = \alpha_l V + D_m$ [L^2T^{-1}], accounts for both molecular diffusion, D_m [L^2T^{-1}], and mechanical dispersion, α_l [L] being the longitudinal dispersivity and $V = q/\theta$ the seepage velocity.

In our work, solute concentrations in the liquid and solid phases are linked by an instantaneous adsorption/desorption equilibrium, implying that the characteristic time scale for adsorption/desorption is

negligible compared to that of advection-dispersion processes. Based on experimental evidence (see Section 4.2), we employ the Freundlich isotherm, i.e.,

$$S = K^F C^{n^F} \quad (4)$$

where K^F [M^{1-nF} L^{3nF} M_{ss}^{-1}] is a measure of sorption capacity, and n^F [-] reflects sorption intensity, i.e., $n^F = 1$ corresponds to linear sorption, while $n^F < 1$ (>1) indicated that sorption is favored at low (high) values of C.

Equations (1)-(4) are solved subject to the following initial conditions:

$$\theta(z, t = 0) = \theta_i = \theta_r + i_\theta(\theta_s - \theta_r) \text{ with } 0 < i_\theta < 1 \quad (5)$$

$$S(z, t = 0) = S_0 = K^F C_0^{n^F} \quad (6)$$

i.e., the initial water content is expressed as a fraction of the total possible range of water content. The effect of inherent uncertainty in i_θ and S_0 on model predictions are assessed in Section 4.

Boundary conditions are set to reflect the experimental setup: (*i*) at the inlet, a prescribed Darcy flow is imposed, $q(z = 0, t) = \hat{q}_{in}(t)$, and the dissolved solute concentration is set to $C(z = 0, t) = 0$; (*ii*) at the outlet, a free drainage condition is applied, i.e., $q(z = L, t) = K(h)$, and $\partial C(z = L, t)/\partial z = 0$.

We solve the flow problem (1)-(2) using the open source numerical code *openRE* (Ireson *et al.*, 2023), which implements Eq. (1) according to the method of lines coupled with an ordinary differential equation solver. Solute transport is simulated with an in-house solver employing a finite difference spatial discretization and a backward Euler time method to model advection and dispersion. At each time step, dissolved and adsorbed solute concentrations are equilibrated according to (4).

3.2. Stochastic calibration strategy

Due to our incomplete knowledge of the hydraulic and transport properties of the soil samples, we treat parameters and initial conditions of Eq.s (1)-(2), i.e. $x_f = [\theta_r, \theta_s, i_\theta, \alpha, n, K_s]$, Eq. (3), i.e. $x_t = [S_0, \alpha_l]$, and Eq. (4), i.e. $x_a = [n^F, K^F]$, as uniformly distributed and uncorrelated random variables.

Intervals of variation for $\boldsymbol{x_f}$ are depicted as grey shaded areas in Figure 2b (topsoil) and 3b (subsoil). These ranges are defined based on literature values to capture the broad variability observed across sandy soil types (e.g., Younes *et al.*, 2017; Babaeian and Tuller, 2023). Parameters embedded in x_a are allowed to vary over several orders of magnitudes, reflecting their wide variability reported in experimental studies (e.g., Bianchi Janetti *et al.*, 2012). Specifically, we allow n^F to vary between 10^{-2} and 10, and K^F between 10^{-2} and 10^5. Considering x_t, we account for the scale-dependent nature of α_l by modeling it as a fraction of the column height, i.e., $\alpha_l \in [1/10 - 1/20]L$ (Neuman *et al.*, 2008). The parameter ranges adopted for S_0 are reported in the Table 1. For each heavy metal the minimum value of S_0, S_0^{min}, reflects the natural background contamination while the maximum value of S_0, S_0^{max}, corresponds to the cumulative load resulting from five years of sewage sludge application for agricultural use. This estimate is based on (*i*) the Regional Council guidelines (Lombardy Region, 2019), which set a maximum annual application rate of 5 *t*/*ha* for soils with Cation Exchange Capacity, CEC > 15 $cmol_{(+)}$ kg^{-1} and pH between 6.0 and 7.5 (conditions that are met for the

soils considered in this study), and (*ii*) the European legislation (Council of the European Communities, 1986, 2006; Italian Parliament, 1992) that prescribes the maximum heavy metal concentrations in sewage sludge as: Cr 200 ppm; Cu 1000 ppm; Ni 300 ppm; Pb 750 ppm; and Zn 2500 ppm. We note that, although the scenario considered here spans conditions from natural background levels to cumulative loads resulting from five years of sewage sludge application, the actual history of metal input to soils may be more variable, for example due to the superposition of multiple metal sources. Finally, since sewage sludge spreading is restricted to the surface, uncertainty in S_0 is considered only for the topsoil, while a deterministic value corresponding to the natural background (i.e., S_0^{min}) is assigned to the subsoil.

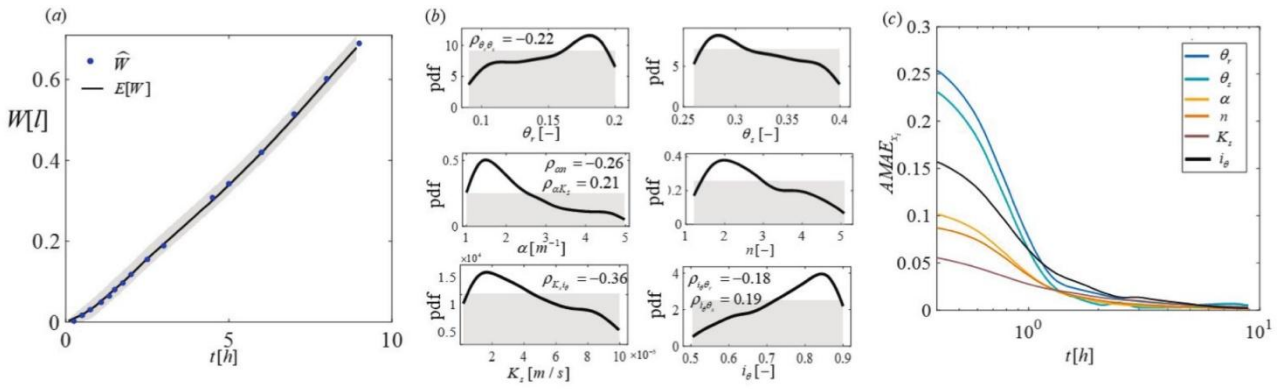

Figure 2. Topsoil: (*a*) temporal evolution of experimental cumulated water outflow, $\widehat{W}(t)$ (blue dots), mean model prediction, *E[W]* (black curve), and associated uncertainty (grey shaded area bounded); (*b*) prior (grey shaded area) and posterior (solid curves) pdf of soil hydraulic parameters, together with the corresponding correlation coefficients (when no negligible); (*c*) temporal evolution of the moment-based global sensitivity index $AMAE_{x_i}$ for each hydraulic parameters.

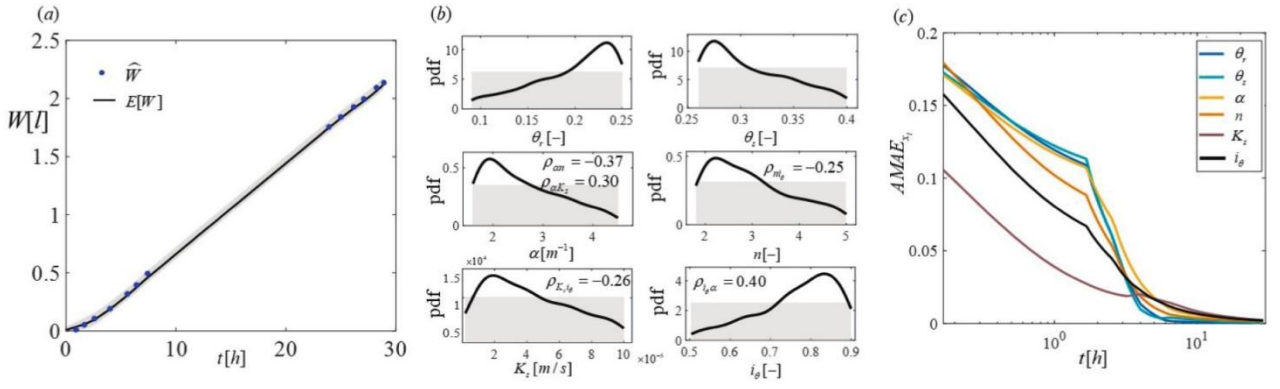

Figure 3. Subsoil: (*a*) temporal evolution of experimental cumulated water outflow, $\widehat{W}(t)$ (blue dots), mean model prediction, *E[W]* (black curve), and associated uncertainty (grey shaded area bounded); (*b*) prior (grey shaded area) and posterior (solid curves) pdf of soil hydraulic parameters, together with the corresponding correlation coefficients (when no negligible); (*c*) temporal evolution of the moment-based global sensitivity index $AMAE_{x_i}$ for each hydraulic parameters.

Table 1. Values of S_0^{min} and S_0^{max} for each heavy metal.

	S_0^{min} [mg kg^{-1}]	S_0^{max} [mg kg^{-1}]
Cr	82.7	84.2
Ni	51.6	53.9
Zn	33.6	52.6
Cu	11.0	18.6
Pb	19.9	25.6

Stochastic calibration of x_f is carried out based on the column flow experiments as follows. For each soil type, we generate NMC Monte Carlo realizations of x_f. Then, for each realization we solve (1)-(2) and evaluate the cumulated water outflow at the *j*-th observation time, $W_j(x_f)$. The flow objective function is then evaluated as

$$J^f = \frac{1}{N_t}\sum_{j=1}^{N_t}\left|\frac{\widehat{W}_j - W_j(x_f)}{\widehat{W}_j}\right| \quad (7)$$

where $\widehat{W}_j$ denotes the experimental cumulated water outflow at time t_j and N_t is the total number of available observations. We then retain only those parameters vectors x_f for which $J^f < 5\%$ and use the accepted realizations to derive the posterior joint probability density function (pdf) of x_f. It is worth noting that the accepted realizations also capture any correlations among the model parameters, as further discussed in Section 4.

A similar procedure is employed for the stochastic calibration of x_a, basis on the batch sorption experiments. First, for each soil-metal combination, we generate NMC Monte Carlo samples of x_a. Then we solve (4) to compute the adsorbed concentration, $S_i(x_a)$, corresponding to the *i*-th experimental dissolved solute concentration, $\hat{C}_i$. The sorption objective function is defined as

$$J^a = \frac{1}{N_C}\sum_{i=1}^{N_C}\left|\frac{\hat{S}_i - S_i(x_a)}{\hat{S}_i}\right| \quad (8)$$

where $\hat{S}_i$ is the experimental adsorbed concentration corresponding to the dissolved concentration $\hat{C}_i$, and N_C is the total number of experimental batch data points. We retain only those parameters vectors x_a resulting in $J^a < 15\%$ for Cr, Cu and Pb and for $J^a < 30\%$ for Ni and Zn. For the latter heavy metals, the acceptance threshold reflects the fact that the Frendulich isotherm (as well as other classical formulations, details not shown) provides a less accurate representation of the experimental data as detailed in Section 4. The accepted x_a samples are then used to construct the posterior joint pdf for x_a for each soil-metal combination. Stable posterior pdfs of x_f and x_a are obtained by retaining approximately 10^4 samples, out of a total of NMC = 10^7 Monte Carlo realizations. Regarding x_t, we restrict our analysis to quantify the impact of its uncertainty on the model output, as no experimental data are available to enable a stochastic calibration of x_t.

3.3. Uncertainty quantification and global sensitivity analysis

After calibration, the residual parameter uncertainty (i.e., the uncertainty remaining after calibration and captured by the posterior joint pdf of model parameters) is projected to quantify the uncertainty in the prediction of a target model output, *y.* Two target outputs are considered: (*i*) the time evolution of the cumulated water outflow, $W(t)$ and (*ii*) the time evolution of the total mass of heavy metal that remain adsorbed onto the soil matrix, $M_s(t)$. The latter choice is consistent with the selected transport scenario (i.e. initially contaminated soil column flushed by rain water) and reflects a focus on the progressive removal of heavy metals from the soil matrix. Nonetheless, the proposed framework is flexible and can be extended to other environmental targets. The uncertainty in the prediction of $W(t)$ and $M_s(t)$ is assessed in a Monte Carlo framework by sampling the posterior pdfs of x_f and x_a and the prior pdf of x_t and by solving Equations (1)-(6) for each sampled parameter set.

Finally, we perform a global sensitivity analysis, GSA, by relying on the *AMA* indices (Dell'Oca *et al.*, 2017). In particular, we focus on the *AMA* index associated with the expected value of *y*,

$$AMAE_{x_i} = \frac{E_{x_i}[|E[y] - E_{\sim x_i}[y|x_i]|]}{E[y]} \tag{7}$$

where $E_{x_i}[]$ denotes the expected value with respect to parameter x_i while $E_{\sim x_i}[]$ represents the expected value with respect to all model parameters but x_i. $AMAE_{x_i}$ quantifies the impact of the uncertainty in x_i on the variability of the expected value of *y*, thus capturing the parameter's influence on the expected model response.

4. Results and discussion

4.1. Soils hydraulic response

Figure 2(*a*) shows the time evolution of observed cumulative water outflow, $\widehat{W}(t)$, for the topsoil. These data are used to perform the stochastic calibration of the flow model parameters $x_f = [\theta_r, \theta_s, i_\theta, \alpha, n, K_s]$. The corresponding posterior pdfs of these parameters are displayed in Figure 2(*b*), together which the Pearson correlation coefficients, ρ, where non-negligible (i.e. $|\rho| > 0.1$). Analogous results for the subsoil are presented in Figures 3(*a*) and 3(*b*). Table 2 also lists the posterior medians and coefficient of variations, *CV*, for each flow parameter.

Table 2. Posterior median values and coefficient of variation (*CV*) of flow model parameters.

	Topsoil		Subsoil	
	Median	*CV*	*Median*	*CV*
θ_r [-]	0.20	0.22	0.14	0.21
θ_s [-]	0.30	0.13	0.31	0.13
i_θ [-]	0.78	0.13	0.77	0.14
α [m^{-1}]	2.45	0.29	1.98	0.46
n [-]	2.80	0.29	2.57	0.38
K_s [m s^{-1}]	3.8×10^{-5}	0.64	3.6×10^{-5}	0.67

The topsoil consists predominantly of sand (Appendix Table A1), the median values of α, n and K_s suggests a well-sorted sandy soil that releases water sharply once the drainage threshold is reached. The relatively high values of α and n suggest a relatively uniform pore structure, with a prevalence of fine sand, reflected also in the relatively low K_s value. The subsoil exhibits a lower α value, indicating a higher water retention capacity and a slightly lower n, suggesting a broader pore-size distribution and more gradual water release compared to the topsoil. These characteristics are consistent with a sandy loam soil, as also confirmed by the properties reported in Appendix Table A1.

Inspection of Figure 2(*b*) and 3(*b*) reveals that, although the prior pdfs of each parameter are uniform, each marginal posterior pdf exhibits a clear peak. At the same time, we note long tails in the parameters pdf and non-negligible *CV* values reflecting the uncertainty in the estimated parameters, in particular for K_s in both soils and (to a lesser extent) α and n in the subsoil. This uncertainty is then propagated to estimate the pdf of W. Figures 2(*a*) and 3(a) include the temporal evolution of the posterior mean of W, $E[W]$ (continuous black curve), along with its uncertainty interval (grey shaded area) bounded by 2nd and 98th percentiles, for the topsoil and subsoil, respectively. In both cases, $E[W]$ closely matches the experimental data, with relatively narrow uncertainty intervals, indicating a satisfactory model performance and reliable predictions of W.

The analysis of the Pearson correlation coefficients reveals consistent patterns across both soils (*i*) i_θ is negatively correlated with K_s and (*ii*) α is positively correlated with K_s and negatively correlated with n. These patterns stem from the model formulation and the nature of the data available for calibration. The negative

correlation between K_s and i_θ arises because both parameters control W, as i_θ increases, K_s (governing the velocity of the wetting front) tends to decrease (and vice versa) to ensure that the simulated W remains consistent with the experimental observations. The positive correlation between α and K_s reflects their combined influence in Eq (2). As α increases the effective saturation, S_e, decreases (for a given pressure head), which during the calibration tends to be compensated by higher values of K_s to reproduce the water outflow. The negative correlation between α and n is also linked to Eq (2). As α increases n tends to decrease to produce steeper water retention curves, enhancing drainage as detected during the experiments.

In the topsoil, θ_r and θ_s are negatively correlated, consistent with their joint control on S_e in Eq (2). Moreover, θ_r and θ_s are negatively and positively correlated with i_θ, respectively. This behavior reflects the interplay of these parameters in determining the initial water content in the column, as described by Eq (5). On the other hand, in the subsoil no strong correlations are observed between θ_r and θ_s, not between either of these parameters and i_θ. Instead: (*i*) i_θ is positively correlated with α, as α increases the average retention capacity of soil increases, thus requiring higher i_θ values to achieve the observed W quantities (and vice-versa); (*ii*) i_θ is negatively correlated with n, larger n values result in sharper water release (i.e., flatter water retention curves), thus requiring smaller i_θ values to achieve a good fit with the experimental W data. The shift between non-negligible correlation between i_θ and θ_r, θ_s for the topsoil to non-negligible correlations between i_θ, α and n for the subsoil suggests a change in the dominant factors controlling the cumulative water outflow. In the subsoil, W is strongly governed by the infiltration dynamics, while in the topsoil, it is mainly controlled by the initial saturation.

In other to further analyzed this aspect, Figures 2(*c*) and 3(c) depict the sensitivity index $AMAE_{x_f}$ in the topsoil and subsoil, respectively. In both soils, we observe a fast decline in $AMAE_{x_f}$ with respect to all parameters as saturation condition approaches, i.e. (approximately) $t_s \approx 1\ h$ for the topsoil and $t_s \approx 1.5$ h for the subsoil. In the topsoil, for times smaller than t_s, $E[W]$ is sensitive to all flow parameters, with the greatest influence from θ_r and θ_s followed by i_θ. These results highlight the dominant role of the parameters controlling the initial water content on $E[W]$. On the other hand, in the subsoil we note a comparable degree of sensitivity of $E[W]$ with respect to θ_r, θ_s, α and n, indicating that infiltration dynamics exert a dominant role in controlling the mean cumulative water outflow. For both soils, a slower decline in $AMAE_{x_i}$ is observed as the column approaches fully saturated conditions (and $E[W]$ becomes insensitive to all parameters, i.e. $AMAE_{x_i} \approx 0$). The time required to reach this condition is longer in the subsoil, due to its lower α and n values, resulting in a slower and more gradual water release compared to the topsoil.

4.2. Heavy metals transport

Figures 4 and 6 show the concentration of heavy metals adsorbed during the batch experiments, $\hat{S}$, in the topsoil and subsoil, respectively. These data are used to perform the stochastic calibration of the adsorption model parameters $x_a = [n^F, K^F]$. The resulting posterior pdfs of these parameters are included in the pictures. The Pearson correlation coefficients is negligible in all analyzed cases. Table 3 also lists the posterior medians and *CV* values for each parameter. The posterior pdfs of K^F and n^F generally exhibit a clear peak, with only a few exceptions (i.e., K^F of Cu and Cr for the topsoil and of Pb in the subsoil), with generally no or only moderate heavy tails. This, together with the relatively low *CV* values listed in Table 3, indicates that the uncertainty associated with these parameters after calibration is generally limited. This uncertainty is then propagated to evaluate the posterior mean of *S*, $E[S]$, (see black solid curves in Figures 4 and 6) and its associated uncertainty interval (shaded grey area) bounded by 2nd and 98th percentiles. Inspection of Figures 4 and 6 reveals an overall satisfactory agreement between $\hat{S}$ and $E[S]$ for Cr, Pb, Cu. Larger discrepancies are noted for Ni and Zn, whose sorption behavior is not fully captured by the Freundlich isotherm as well as by other classical models (details not shown). Uncertainty bounds are also wider for Ni and Zn than for to the other metals, a result that is linked to the higher acceptance threshold adopted during the calibration of the Freundlich isotherm for these two metals (see Section 3.2).

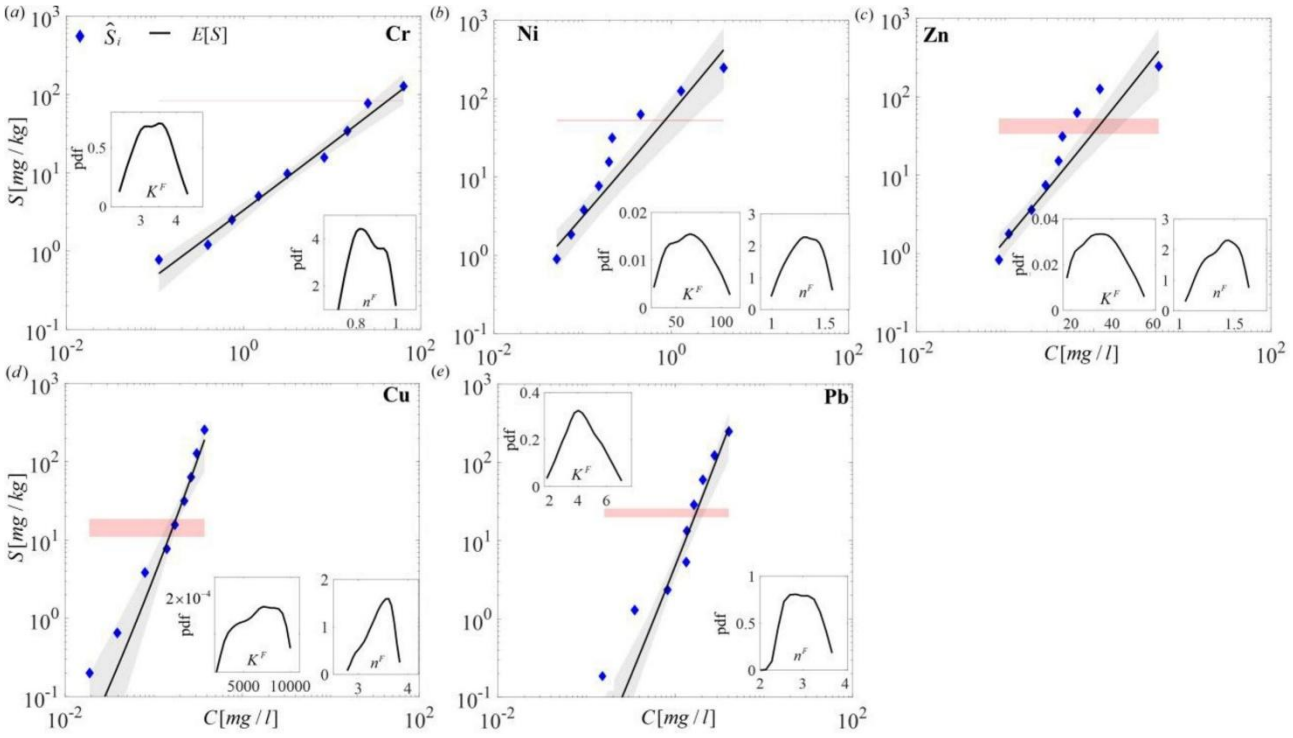

Figure 4. Topsoil: experimental adsorbed solute concentrations, $\hat{S}$ (blue dots), versus the corresponding dissolved concentrations for (*a*) Cr, (*b*) Ni, (*c*) Zn, (*d*) Cu and (*e*) Pb. The predicted expected value of S, $E[S]$ (black curve), and its associated uncertainty interval (shaded grey area) are also shown. Each panel also displays the adopted range of initial sorbed concentrations (shaded pink area, see Table 1) and the calibrated pdf of the adsorption isotherm parameters K^F [$mg^{1-nF} l^{nF} kg^{-1}$] and n^F [−].

Table 3. Posterior median and coefficient of variation (*CV*) values of the adsorption model parameters.

	Topsoil				Subsoil			
	K^F [$mg^{1-nF} l^{nF} kg^{-1}$]		n^F [-]		K^F [$mg^{1-nF} l^{nF} kg^{-1}$]		n^F [-]	
	Median	*CV*	*Median*	*CV*	*Median*	*CV*	*Median*	*CV*
Cr	3.3	0.13	0.86	0.08	3.3	0.12	0.82	0.10
Ni	63.8	0.33	1.31	0.11	17.6	0.08	1.29	0.04
Zn	34.3	0.27	1.37	0.10	53.2	0.32	1.36	0.11
Cu	6.5×10^3	0.32	3.44	0.07	3.4×10^3	0.53	2.34	0.13
Pb	4.5	0.18	2.97	0.06	4.3×10^4	0.40	3.39	0.06

Overall, our results indicate that in both soils: (*i*) Cr displays the highest mobility, consistent with its anionic, soluble, and strongly oxidizing nature, particularly under the unsaturated conditions of the experiment; (*ii*) Ni and Zn show intermediate and comparable behavior consistent with their weak complexation with organic matter, while (*iii*) Cu appears as the least mobile metal, reflecting its strong affinity for organic matter and mineral surfaces, which limits transport in both soils. Otherwise, Pb shows low mobility in the subsoil and intermediate mobility in the topsoil. The contrasting Pb sorption behavior between soil horizons, where Pb shows lower sorption capacity in the more organic-rich topsoil than in the subsoil, deviates from theoretical expectations but aligns with patterns observed in urban soils. This apparent anomaly may stem from: (*i*) partial occupation of high-affinity binding sites by background metals typical of urban environments, which reduces the available sorption capacity (Violante *et al.*, 2010); (*ii*) competition for organic binding sites (McBride *et al.*, 1997); and (*iii*) formation of soluble Pb-organic complexes that enhance mobility rather than retention at higher organic matter concentrations (Sauvé *et al.*, 1998). While these mechanisms are plausible and supported by previous studies, they were not directly tested in our sorption experiments.

We conclude our analysis by computing how the residual (i.e., post calibration) uncertainty in flow and transport parameters propagate to the estimated mass of heavy metals that remain adsorbed onto the soil matrix, i.e., M_s, a quantity of particular interest for risk assessment procedures. Figure 5 and 7 show the predicted mean of M_s, $E[M_s]$ (black solid curve) along with its uncertainty intervals (dashed grey area) for the topsoil and subsoil, respectively. As expected, for the less mobile metals (Ni, Zn, Cu, Pb) there is not a strong decrease in either the mean and the uncertainty prediction intervals of M_s over the investigated period. In contrast, for the most mobile metal (Cr), a clear decrease of $E[M_s]$ over time is observed. However, this is also associated with larger, and time-evolving, uncertainty bounds.

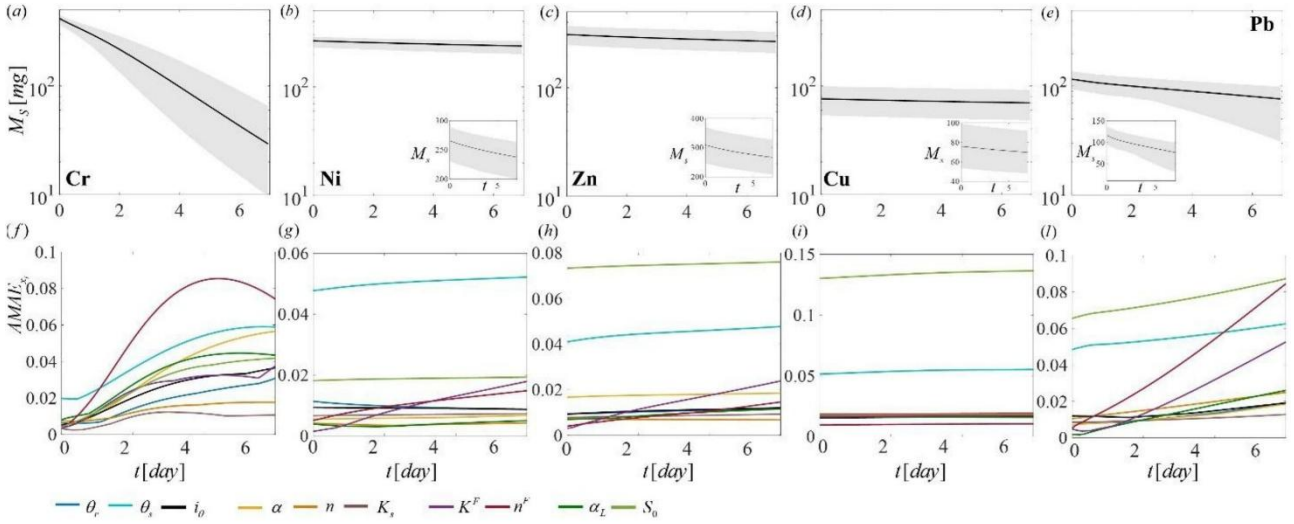

Figure 5. Topsoil: temporal evolution of the mean model prediction (black curve) and associated uncertainty interval (grey shaded area) of the mass of heavy metal adsorbed in the soil column, M_S, together with the corresponding global sensitivity index $AMAE_{x_i}$ for each model parameter. Results are shown for (*a*, *f*) Cr, (*b*, *g*) Ni, (*c*, *h*) Zn, (*d*, *i*) Cu and (*e*, *l*) Pb.

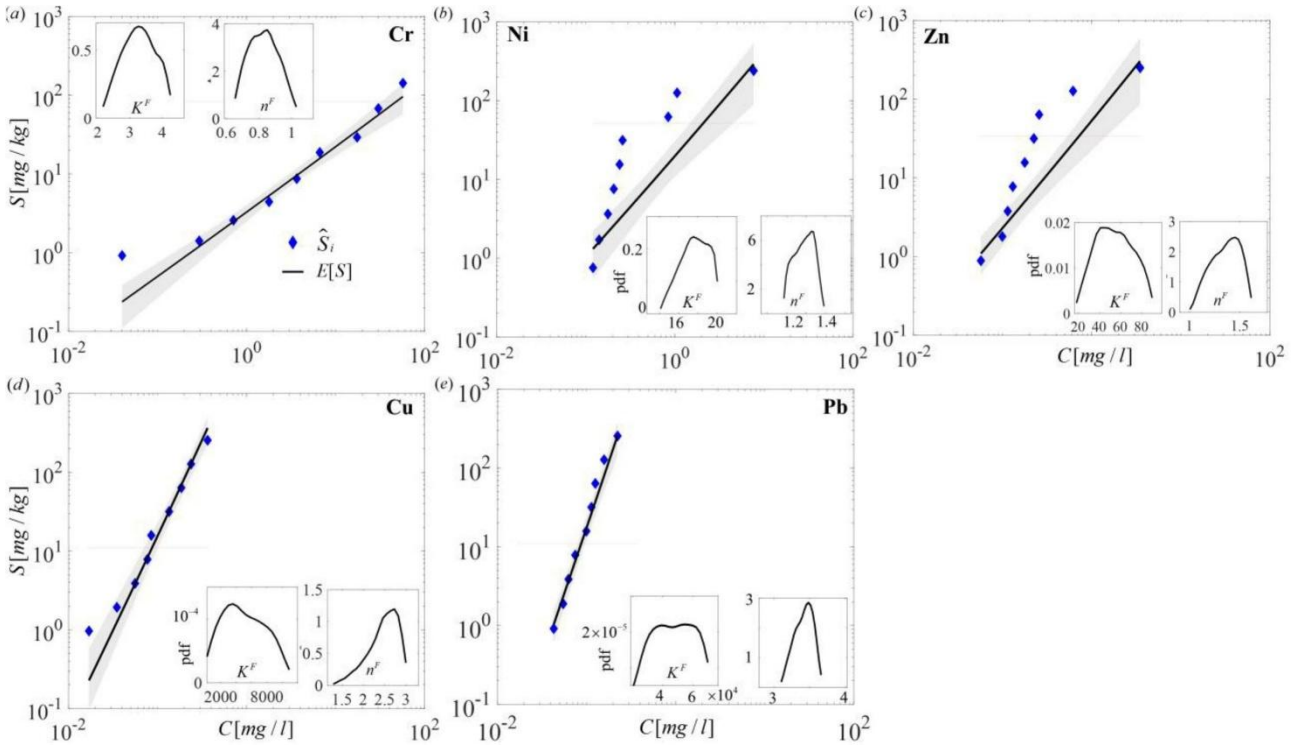

Figure 6. Subsoil: experimental adsorbed solute concentrations, $\hat{S}$ (blue dots), versus the corresponding dissolved concentrations for (*a*) Cr, (*b*) Ni, (*c*) Zn, (*d*) Cu and (*e*) Pb. The predicted expected value of S, $E[S]$ (black curve), and its associated uncertainty interval (shaded grey area) are also shown. Each panel also displays the adopted range of initial sorbed concentrations (shaded pink area, see Table 1) and the calibrated pdf of the adsorption isotherm parameters K^F [$mg^{1-nF} l^{nF} kg^{-1}$] and n^F [−].

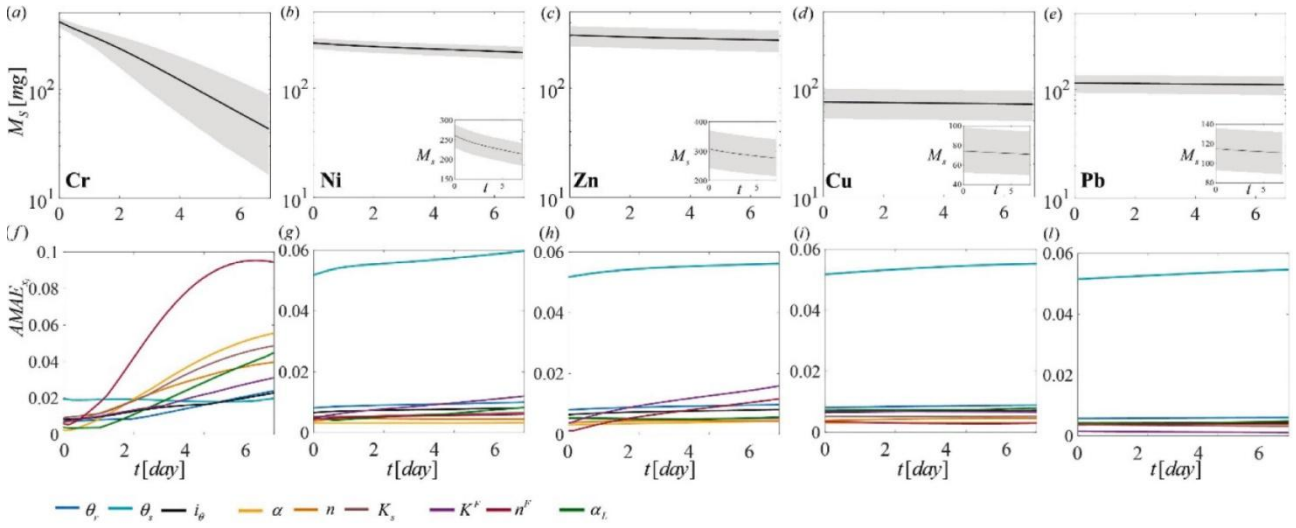

Figure 7. Subsoil: temporal evolution of the mean model prediction (black curve) and associated uncertainty interval (grey shaded area) of the mass of heavy metal adsorbed in the soil column, M_S, together with the corresponding global sensitivity index $AMAE_{x_i}$ for each model parameter. Results are shown for (*a*, *f*) Cr, (*b*, *g*) Ni, (*c*, *h*) Zn, (*d*, *i*) Cu and (*e*, *l*) Pb.

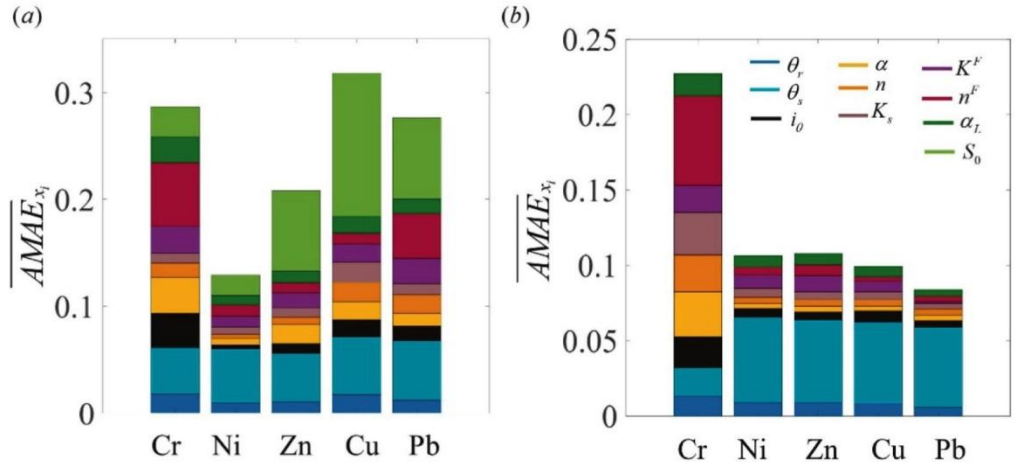

Figure 8. Time averaged global sensitivity index, $\overline{AMAE}_{x_i}$, for the mass of heavy metal adsorbed in the soil column, M_S, considering (*a*) the topsoil and (*b*) the subsoil.

Figure 5 and 7 also include the sensitivity indices $AMAE_{x_i}$ for all parameters. The overall inspection of Figure 5 and 7 reveals two distinct sensitivity patterns, depending on the mobility of the heavy metal. In case of low (Cu) and intermediate mobile (Ni, Zn) metals the highest sensitivity are associated with θ_s and, in the topsoil also with S_0. This indicates that, for these metals, the key controlling factors of $E[M_S]$ are the maximum water content available for dilution (linked to θ_s) and, in the topsoil, the initial amount of metal adsorbed on the soil matrix. For Ni and Zn, an increase in sensitivity to the parameters associated with the adsorption process, K^F and n^F is observed over time, reflecting the onset of desorption processes as these intermediate mobile metals become mobilized. This behavior is not displayed by Cu (the least mobile metal) within the seven-days time scale here considered. For the highly mobile metal Cr, all $AMAE_{x_i}$ values are non-negligible and tend to

increase over time, indicating that Cr release is strongly impacted by the strength and characteristic of the flow, transport and sorption processes. At early times, sensitivity to θ_s is dominant followed, for the topsoil, by sensitivity to S_0. This observation, suggests that, during the initial phase, $E[M_s]$is primarily controlled by the maximum water content available for dilution (linked to θ_s) and, in the topsoil, also by the initial amount of Cr sorbed onto the soil matrix. Over time, the influence of all other parameters increases, with the adsorption parameter K^F becoming dominant. This indicates desorption dynamics play and increasing important role over time. Concurrently, as Cr is progressively mobilized from the soil, flow and transport parameters exert a growing influence on the temporal evolution of $E[M_s]$. We further note that in case of Pb in the topsoil, the sensitivity of $E[M_s]$ to the diverse parameters exhibits a mixed behavior: it shares similarities with the mobile metal Cr (e.g., comparable $AMAE_{x_i}$ magnitude across parameters associated with diverse processes), while also retaining features typical of low mobile metals (e.g., large and persistent sensitivity to θ_s and S_0). These findings are further supported by Figure 8, which displays the time averaged sensitivity index $\overline{AMAE}_{x_i}$ for all parameters and heavy metals considered in (*a*) the topsoil and (*b*) subsoil.

5. Conclusions

We investigate the transport of five selected heavy metals (Cr, Ni, Zn, Cu, Pb) in unsaturated urban soils by integrating laboratory experiments, stochastic calibration, global sensitivity analysis and stochastic forecasting techniques.

Our work leads to the following major conclusions:

- Cumulative water flow data provide valuable information for calibrating flow parameters. However these parameters, particularly the saturated hydraulic conductivity, remain affected by non-negligible residual (i.e., after calibration) uncertainty. This underscores the need of adopting a stochastic approach during both the calibration and prediction phases.
- For highly mobile heavy metals, their mobility is impacted by characteristic of the flow, transport and adsorption processes. On the other hand, in case of low mobile heavy metals, their fate is chiefly controlled by the maximum water content available and the initial amount of metal adsorbed onto the soil. This finding has broad implications for prioritizing data collection in contaminated site investigations.

The methodological framework developed in this study is transferable to urban and peri-urban contexts worldwide and can support the formulation of science-based regulatory guidelines that explicitly include and quantify prediction uncertainty, moving beyond the deterministic safety factors that still dominate current practice (Carlon *et al.*, 2004). Potential extensions of this work include investigating the effects of spatial heterogeneity in soil properties on vadose-zone flow and transport processes.

Financial support

National Recovery and Resilience Plan (NRRP), mission 4 component 2 investment 1.4 - call for tender no. 3138 of 16 December 2021, rectified by decree no. 3175 of 18 December 2021 of Italian Ministry of University and Research funded by the European Union - NextGenerationEU, project code CN_00000033, concession decree no. 1034 of 17 June 2022 adopted by the Italian Ministry of University and Research, CUP D43C22001250001, project title “National Biodiversity Future Center - NBFC”.

CRediT authorship contribution statement

Aronne Dell'Oca: Writing - review & editing, Writing - original draft, Visualization, Validation, Software, Methodology, Formal analysis, Data curation, Conceptualization. Davide Abu El Khair: Writing - review & editing, Writing - original draft, Methodology, Investigation, Data curation. Chiara Ferré: Writing - review & editing, Supervision, Project administration, Investigation, Funding acquisition. Roberto Comolli: Writing - review & editing, Supervision, Investigation, Funding acquisition. Monica Riva: Writing - review & editing, Writing - original draft, Supervision, Resources, Project administration, Methodology, Funding acquisition, Formal analysis, Conceptualization.

Declaration of interests

The authors declare that they have no known competing financial interests or personal relationships that could have appeared to influence the work reported in this paper.

References

Adamiec, E., Jarosz-Krzemińska, E., & Wieszała, R. (2016). Heavy metals from non-exhaust vehicle emissions in urban and motorway road dusts. *Environmental Monitoring and Assessment*, 188(6), 369. https://doi.org/10.1007/s10661-016-5377-1.

Adriano, D. C. (2001) Trace Elements in Terrestrial Environments: Biogeochemistry, Bioavailability and Risks of Metals. 2nd Edition, *Springer*. http://dx.doi.org/10.1007/978-0-387-21510-5.

Alloway, B. J. (2013). Heavy metals in soils: Trace metals and metalloids in soils and their bioavailability (Vol. 22). *Springer*. https://doi.org/10.1007/978-94-007-4470-7.

Arıman, S., & Balkaya, N. (2025). Spatial and seasonal assessment of heavy metal contamination in Golden Horn sediments, İstanbul, Türkiye: Ecological impacts, human health risks, and environmental monitoring. *Journal of Contaminant Hydrology*, 275, 104696. https://doi.org/10.1016/j.jconhyd.2025.104696.

Babaeian, E., & Tuller, M. (2023). The feasibility of remotely sensed near-infrared reflectance for soil moisture estimation for agricultural water management. *Remote Sensing*, 15(11), 2736. https://doi.org/10.3390/rs15112736.

Bartlett, R., & James, B. (1979). Behavior of chromium in soils: III. Oxidation. *Journal of Environmental Quality*, 8, 31-35.

Bianchi Janetti E, I Dror, M Riva, A Guadagnini, B Berkowitz (2012) Estimation of single-metal and competitive sorption isotherm through Maximum likelihood and model quality criteria, *Soil Science Society of America Journal*, 76:1229-1245. https://doi.org/10.2136/sssaj2012.0010.

Bianchi Janetti, E., Guadagnini, L., Riva, M., & Guadagnini, A. (2019). Global sensitivity analyses of multiple conceptual models with uncertain parameters driving groundwater flow in a regional-scale sedimentary aquifer. *Journal of Hydrology*, 574, 544-556. https://doi.org/10.1016/j.jhydrol.2019.04.035.

Bonten, L. T. C., Kroes, J. G., Groenendijk, P., & van der Grift, B. (2012). Modeling diffusive Cd and Zn contaminant emissions from soils to surface waters. *Journal of Contaminant Hydrology*, 138-139, 113-122. https://doi.org/10.1016/j.jconhyd.2012.06.008.

Carlon, C., Critto, A., Marcomini, A., & Nathanail, P. (2004). Risk based characterisation of contaminated industrial site using multivariate and geostatistical tools. *Environmental Pollution*, 132(3), 471-484. https://doi.org/10.1016/j.envpol.2004.05.009.

Ceresa, L., Guadagnini, A., Rodríguez-Escales, P., Riva, M., Sanchez-Vila, X., & Porta, G. M. (2023). On multi-model assessment of complex degradation paths: The fate of diclofenac and its transformation products. *Water Resources Research*, 59, e2022WR033183. https://doi.org/10.1029/2022WR033183.

Commission of the European Communities. (2006). Thematic Strategy for Soil Protection. https://eur-lex.europa.eu/legal-content/EN/TXT/?uri=CELEX:52006DC0231.

Council of the European Communities (1986). Council Directive of June 12th, 1986 on the protection of the environment, and in particular of the soil, when sewage sludge is used in agriculture (86/278/EEC).

Dell'Oca, A. (2023). Sensitivity analysis: An operational picture. *Water Resources Research*, 59, e2022WR033780. https://doi.org/10.1029/2022WR033780.

Dell'Oca, A., Riva, M., & Guadagnini, A. (2017). Moment-based metrics for global sensitivity analysis of hydrological systems. *Hydrology and Earth System Sciences*, 21(12), 6219-6234. https://doi.org/10.5194/hess-21-6219-2017.

Dell'Oca A, Guadagnini, A, Riva M (2023) Probabilistic assessment of failure of infiltration structures under model and parametric uncertainty, *Journal of Environmental Management*, 344, 118466. https://doi.org/10.1016/j.jenvman.2023.118466.

Deng, H., Ye, M., Schaap, M. G., & Khaleel, R. (2009). Quantification of uncertainty in pedotransfer function-based parameter estimation for unsaturated flow modeling. *Water Resources Research*, 45(4). https://doi.org/10.1029/2008WR007477.

Dye, H. B., Houston, S. L., & Welfert, B. D. (2009). Influence of unsaturated soil properties uncertainty on moisture flow modeling. *Geotechnical and Geological Engineering*, 29, 161-169. https://doi.org/10.1007/s10706-009-9281-0.

Fendorf, S.E. (1995). Surface reactions of chromium in soils and waters. *Geoderma*, 67, 55-71.

Ferreira, A. J. D., Soares, D., Serrano, L. M. V., Ferreira, C. S. S., Lopes, F. P., Coelho, C., & Walsh, R. P. D. (2016). Roads as sources of heavy metals in urban areas: The Covões catchment experiment, Coimbra, Portugal. *Journal of Soils and Sediments*, 16, 2622-2639. https://doi.org/10.1007/s11368-016-1492-4.

Giller, K. E., Witter, E., & McGrath, S. P. (1998). Toxicity of heavy metals to microorganisms and microbial processes in agricultural soils: A review. *Soil Biology and Biochemistry*, 30(10-11), 1389-1414. https://doi.org/10.1016/S0038-0717(97)00270-8.

He, T., Li, Y., Huang, Y., He, E., Li, Y., Qu, L., ... & Zhao, L. (2023). Simulation and risk assessment of arsenic by *Hydrus-3D* and *CalTOX* in a typical brownfield site. *Journal of Hazardous Materials*, 452, 130892. https://doi.org/10.1016/j.jhazmat.2023.130892.

Ireson, A. M., Spiteri, R. J., Clark, M. P., & Mathias, S. A. (2023). A simple, efficient, mass-conservative approach to solving Richards' equation (*openRE*, v1.0). *Geoscientific Model Development*, 16, 659-677. https://doi.org/10.5194/gmd-16-659-2023.

Italian Parliament. (1992). Legislative Decree January 27th, 1992, n. 99: Implementation of the European Directive n. 86/278/CEE "on the protection of the environment, and in particular of the soil, when sewage sludge is used in agriculture" (d. lgs. 99/1992).

IUSS Working Group WRB. (2022). World Reference Base for Soil Resources: International soil classification system for naming soils and creating legends for soil maps (4th ed.). International Union of Soil Sciences (IUSS).

Jiang, Z., Guo, Z., Peng, C., Wang, X., Zhou, Z., & Xiao, X. (2023). Model development and probabilistic risks of cadmium transport in slag-soil-groundwater systems with heterogeneous conditions. *Science of The Total Environment*, 895, 165160. https://doi.org/10.1016/j.scitotenv.2023.165160.

Kahl, G. M., Sidorenko, Y., & Gottesbüren, B. (2015). Local and global inverse modelling strategies to estimate parameters for pesticide leaching from lysimeter studies. *Pest Management Science*, 71(4): 616-31, https://doi.org/10.1002/ps.3914.

Kandeler, E., Tscherko, D., & Spiegel, H. (1999). Long-term monitoring of microbial biomass, N mineralization and enzyme activities of a Chernozem under different tillage management. *Biology and Fertility of Soils*, 28, 343-351. https://doi.org/10.1007/s003740050502.

Khan, S., El-Latif Hesham, A., Qiao, M., Rehman, S., & He, J. Z. (2010). Effects of Cd and Pb on soil microbial community structure and activities. *Environmental Science and Pollution Research*, 17, 288-296. https://doi.org/10.1007/s11356-009-0134-4.

Khan, K., Khan, M. S., Younas, M., Yaseen, M., Al-Sehemi, A. G., Kavil, Y. N., Su, C., Ali, N., Maryam, A., & Liang, R. (2025). Pathways and risk analysis of arsenic and heavy metal pollution in riverine water: Application of multivariate statistics and USEPA-recommended risk assessment models. *Journal of Contaminant Hydrology*, 269, 104483. https://doi.org/10.1016/j.jconhyd.2024.104483.

Kumar, S., Behera, D., Ajay, K., Karthick, B., Dharia, C., & Anoop, A. (2024). Microplastics and heavy metal contamination along a land-use gradient in a Himalayan foothill river: Prevalence and controlling factors. *Journal of Contaminant Hydrology*, 266, 104411. https://doi.org/10.1016/j.jconhyd.2024.104411.

Li, X., Poon, C. S., & Liu, P. S. (2001). Heavy metal contamination of urban soils and street dusts in Hong Kong. *Applied Geochemistry*, 16(11-12), 1361-1368. https://doi.org/10.1016/S0883-2927(01)00045-2.

Liu, T., Du, W., Yu, S., & Zhang, W. (2026). Distribution, sources, and probabilistic risk assessment of heavy metals in the wetland water-sediment system: Based on *CEWQI*, *PLI*, *PMF*, and two-dimensional Monte Carlo method. *Journal of Contaminant Hydrology*, 276, 104753. https://doi.org/10.1016/j.jconhyd.2025.104753.

Lombardy Region (2019). Decision of the Regional Council May 14th, 2019, n. 6665: Recognition of the concentration limits characterizing sewage sludge suitable for use in agriculture (DGR 6665/2019).

Lu, X., Wang, L., Li, L. Y., Lei, K., Huang, L., & Kang, D. (2010). Multivariate statistical analysis of heavy metals in street dust of Baoji, NW China. *Journal of Hazardous Materials*, 173(1-3), 744-749. https://doi.org/10.1016/j.jhazmat.2009.09.001.

Ma, Z., Bi, Y., & Qi, L. (2026). Investigation of cadmium adsorption-transport coupling in soil-mineral systems: Integrating batch adsorption and column transport experiments. *Journal of Contaminant Hydrology*, 276, 104765. https://doi.org/10.1016/j.jconhyd.2025.104765.

Manan, F., Khan, S. M., Asif, I., Mohammad, N., Ahmad, Z., Abbas, F. M., & Hashem, M. (2026). Assessment of the Korang River's water via ecological risk indices and source apportionment procedures for heavy metals contamination, and evaluation of cancer/non-cancer risks. *Journal of Contaminant Hydrology*, 276, 104780. https://doi.org/10.1016/j.jconhyd.2025.104780.

Manta, D. S., Angelone, M., Bellanca, A., Neri, R., & Sprovieri, M. (2002). Heavy metals in urban soils: a case of study from the city of Palermo (Sicily), Italy. *Science of The Total Environment*, 300(1-3), 229-243. https://doi.org/10.1016/S0048-9697(02)00273-5.

McBride, M., et al. (1997). Copper solubility and speciation in in situ contaminated soils. *Environmental Toxicology and Chemistry*, 16, 2215-2222.

Neuman, S.P., M Riva, A Guadagnini (2008) On the geostatistical characterization of hierarchical media. *Water Resources Research*, 44, W02403, https://doi.org/10.1029/2007WR006228.

Nicholson, F. A., Smith, S. R., Alloway, B. J., Carlton-Smith, C., & Chambers, B. J. (2003). An inventory of heavy metals inputs to agricultural soils in England and Wales. *Science of The Total Environment*, 311(1-3, 205-219. https://doi.org/10.1016/S0048-9697(03)00139-6.

Pan, F., Ye, M., Zhu, J., Wu, Y.-S., Hu, B. X., & Yu, Z. (2009). Incorporating layer- and local-scale heterogeneities in numerical simulation of unsaturated flow and tracer transport. *Journal of Contaminant Hydrology*, 103(3-4), 194-205. https://doi.org/10.1016/j.jconhyd.2008.10.005.

Pan, Y., Li, X., Chen, M., Wang, X., & Leng, Y. (2025). Identification of heavy metal sources in reservoir-adjacent soils and specific source risk assessment based on comprehensive environmental factors: A perspective on prioritizing control sources. *Journal of Contaminant Hydrology*, 274, 104673. https://doi.org/10.1016/j.jconhyd.2025.104673.

Rostami, A. A., Sedghi, Z., Nadiri, A. A., Barzegar, R., Dimova, N. T., Senapathi, V., & Islam, A. R. M. T. (2025). Harnessing deep learning for fusion-based heavy metal contamination index prediction in groundwater. *Journal of Contaminant Hydrology*, 274, 104672. https://doi.org/10.1016/j.jconhyd.2025.104672.

Sandoval, L., Dell'Oca, A., & Riva, M. (2024). Operational sensitivity analysis of flooding volume in urban areas. *Sustainable Cities and Society*, 117, 105928. https://doi.org/10.1016/j.scs.2023.105928.

Sauvé, S., et al. (1998). Lead phosphate solubility in water and soil suspensions. Environmental Science & Technology, 32, 388-393.

Selim, T., Elkefafy, S. M., Berndtsson, R., Elkiki, M., & El-kharbotly, A. A. (2023). Heavy metal transport in different drip-irrigated soil types with potato crop. *Sustainability*, 15(13), 10542. https://doi.org/10.3390/su151310542.

Shao, W., Chen, S., Su, Y., Dong, J., Ni, J., Yang, Z., & Zhang, Y. (2023). Reduce uncertainty in soil hydrological modeling: A comparison of soil hydraulic parameters generated by random sampling and pedotransfer function. *Journal of Hydrology*, 623, 129740. https://doi.org/10.1016/j.jhydrol.2023.129740.

Stefanowicz, A. M., Niklińska, M., & Laskowski, R. (2008). Metals affect soil bacterial and fungal functional diversity differently. *Environmental Toxicology and Chemistry*, 27(3), 591-598. https://doi.org/10.1897/07-288.1.

Tian, Z., Pan, Y., Chen, M, Zhang, S., & Chen, Y. (2023). The relationships between fractal parameters of soil particle size and heavy-metal content on alluvial-proluvial fan. *Journal of Contaminant Hydrology*, 254, 104140. https://doi.org/10.1016/j.jconhyd.2023.104140.

Tóth, G., Hermann, T., Da Silva, M. R., & Montanarella, L. (2016). Heavy metals in agricultural soils of the European Union with implications for food safety. *Environment International*, 88, 299-309. https://doi.org/10.1016/j.envint.2015.12.017.

van der Grift, B., & Griffioen, J. (2008). Modelling assessment of regional groundwater contamination due to historic smelter emissions of heavy metals. *Journal of Contaminant Hydrology*, 96(1-4), 48-68. https://doi.org/10.1016/j.jconhyd.2007.10.001.

Violante, A., et al. (2010). Mobility and bioavailability of heavy metals and metalloids in soil environments. *Journal of Soil Science and Plant Nutrition*, 10, 268-292.

Wang, D., Xu, P. Y., An, B. W., & Guo, Q. P. (2024). Urban green infrastructure: Bridging biodiversity conservation and sustainable urban development through adaptive management approach. *Frontiers in Ecology and Evolution*, 12, 1440477. https://doi.org/10.3389/fevo.2024.1440477.

Xu, Z., Yin, M., Yang, X., Yang, Y., Xu, X., Li, H., Hong, M., Qiu, G., Feng, X., Tan, W., & Yin, H. (2024). Simulation of vertical migration behaviors of heavy metals in polluted soils from arid regions in northern China under extreme weather. *Science of The Total Environment*, 919, 170494. https://doi.org/10.1016/j.scitotenv.2024.170494.

Ye, M., Pan, F., Wu, Y.-S., Hu, B. X., Shirley, C., & Yu, Z. (2007). Assessment of radionuclide transport uncertainty in the unsaturated zone of Yucca Mountain. *Advances in Water Resources*, 30(1), 118-134. https://doi.org/10.1016/j.advwatres.2006.03.005.

Younes, A., Mara, T., Fahs, M., Grunberger, O., & Ackerer, P. (2017). Hydraulic and transport parameter assessment using column infiltration experiments. *Hydrology and Earth System Sciences*, 21(5), 2263-2275. https://doi.org/10.5194/hess-21-2263-2017.

Appendix

Table A1

Table A1. Main characteristic of the soil profile.

Soil horizon	Depth [cm]	pH	Org C [%]	Tot N [%]	bulk density [g cm^{-3}]	CEC [$cmol_{(+)}$ kg^{-1}]	BS [%]	Sand [g kg^{-1}]	Silt [g kg^{-1}]	Clay [g kg^{-1}]	textural class USDA
Ap (topsoil)	0-32	6.4	3.00	0.18	0.99	17.90	76.3	552	384	64	SL
Bw1 (subsoil)	32-60	6.6	0.72	0.07	1.26	14.08	65.4	472	341	187	L
Bw2	60-94	6.6	0.52	0.06		12.11	62.3	540	286	174	SL
BC	94-122	6.7	0.21	0.03		6.24	52.1	793	152	55	LS
C	122-150	6.9	0.10	< 0.001		2.78	64.4	939	50	11	S

General Conclusions

Urban and peri-urban soils are complex environmental systems shaped by the long-term interplay between anthropogenic pressures, land-use change, and natural pedogenetic processes. This PhD thesis investigated urban and peri-urban soils of the Metropolitan City of Milan by integrating pedological, biogeochemical, ecological, and process-based perspectives, with the overarching aim of understanding how soil carbon dynamics, vegetation development, and contaminant behaviour co-evolve in highly heterogeneous and human-impacted landscapes.

Taken together, the four thematic chapters provide a coherent and multi-scale framework for interpreting urban soil functioning, highlighting soil depth, carbon quality, and soil heterogeneity as central organizing principles.

Soil-vegetation interactions and SOC dynamics following urban afforestation

The first thematic chapter demonstrated that afforestation of former agricultural soils in urban and peri-urban contexts leads to rapid and measurable changes in soil organic carbon (SOC) contents, humus forms, and understory vegetation functional composition. The combined pedological and ecological approach revealed that SOC accumulation is not uniform with depth and is closely linked to forest development stage, humus form evolution, and soil physical-chemical properties.

These results show that urban soils retain a strong legacy of past land use, which continue to influence soil properties, while remaining highly responsive to vegetation establishment. Importantly, SOC dynamics reflected multiple, coexisting stabilization pathways rather than a single dominant process, emphasizing the need to interpret carbon sequestration in urban forests through an integrated soil-vegetation lens.

Pyrogenic carbon as a persistent component of urban soil organic matter

Building on the limitations of bulk SOC as a sole indicator of carbon dynamics, the second thematic chapter focused on pyrogenic carbon (PyC) as a chemically distinct and persistent fraction of soil organic matter. At the city scale, PyC was shown to be a ubiquitous component of urban and peri-urban soils, with relatively stable PyC:SOC ratios across soil depths and land-use contexts.

The results indicate that PyC distribution reflects long-term atmospheric deposition and stabilization processes rather than short-term ecological dynamics. While SOC contents responded strongly to vegetation development and soil depth, PyC exhibited greater persistence and relative stability, highlighting its role as a long-term carbon reservoir in urban soils. These findings underscore that urban soil carbon pools cannot be fully understood without explicitly accounting for combustion-derived inputs and their distinct stabilization pathways.

Methodological sensitivity and depth-dependent convergence of PyC estimates

The third thematic chapter demonstrated that methodological choices critically influence PyC quantification, particularly in surface soils. The comparison between chemo-thermal oxidation (CTO-360) and chemical oxidation (CO) showed that methodological divergence is most pronounced in topsoil layers, where CO

captures a broader range of less refractory aromatic structures. With increasing soil depth, PyC estimates obtained by the two methods progressively converged, indicating that deeper horizons are dominated by highly condensed and thermally stable PyC forms that are similarly isolated by both approaches.

This depth-dependent convergence provides an important interpretative key for PyC studies and reinforces the relevance of soil depth as a fundamental axis for understanding carbon persistence. Moreover, the methodological comparison clarified that while PyC contributes to long-term carbon storage, the non-pyrogenic SOC fraction (SOC_nPyC) represents the primary reactive pool governing metal retention and biogeochemical interactions in these soils.

From carbon fractionation to contaminant mobility in unsaturated urban soils

The final thematic chapter extended the insights gained from carbon characterization to the process-based assessment of heavy metal mobility in unsaturated urban soils. By combining laboratory experiments with stochastic modelling, this work demonstrated that contaminant transport is strongly controlled by soil heterogeneity, hydraulic properties, and sorption processes, with parameter uncertainty playing a key role in shaping predictions of metal migration toward groundwater.

Importantly, the results highlighted that many of the soil properties influencing contaminant mobility - such as texture, organic carbon content, and depth-dependent structure - are the same properties governing SOC and PyC stabilization. This reinforces the conceptual link between soil carbon dynamics and contaminant behaviour and confirms that urban soils cannot be treated as homogeneous media in environmental risk assessments.

Integrated perspective and implications

Overall, this thesis shows that urban soils function as stratified, multifunctional systems in which carbon persistence, vegetation development, and contaminant dynamics are tightly interconnected. Soil depth emerges as a unifying dimension across all chapters, structuring carbon stabilization pathways, biological activity, and contaminant transport processes. Likewise, distinguishing between carbon quantity and carbon quality proved essential for interpreting both ecosystem functioning and environmental risk in urban contexts.

From an applied perspective, these findings highlight the importance of soil-aware management strategies in urban green infrastructures. Enhancing soil organic matter through afforestation and green space development can promote carbon sequestration and ecosystem services, but the quality and persistence of carbon inputs—as well as their interactions with contaminants—must be explicitly considered. Incorporating depth-resolved soil information and method-aware carbon assessments is therefore critical for designing effective nature-based solutions and for improving the sustainability and resilience of urban environments.

Finally, this work demonstrates that integrating pedology, biogeochemistry, ecology, and process-based modelling provides a robust framework for advancing urban soil science. Future research should build on this integrated approach by further exploring the long-term evolution of carbon fractions, the coupling between

biological and physicochemical stabilization mechanisms, and the implications of soil heterogeneity for contaminant dynamics under changing climatic and urbanization scenarios.

Taken together, the results of this thesis demonstrate that carbon persistence, vegetation dynamics, and contaminant processes are tightly interconnected components of urban soil functioning. While Chapters 1-3 highlight the role of soil organic matter and pyrogenic carbon in supporting ecosystem services such as carbon storage and biodiversity, Chapter 4 shows that the same properties also regulate contaminant mobility and environmental risk. This confirms that urban soils must be interpreted as multifunctional systems, where processes related to ecosystem services and risks co-occur and interact across spatial and vertical gradients.

Tesi di dottorato realizzata nell'ambito del progetto NBFC finanziato dal PNRR Missione 4 Componente 2 Investimento 1.4, finanziato dall'Unione Europea - NextGenerationEU - CUP H43C22000530001